

INFORMATION TO USERS

This manuscript has been reproduced from the microfilm master. UMI films the text directly from the original or copy submitted. Thus, some thesis and dissertation copies are in typewriter face, while others may be from any type of computer printer.

The quality of this reproduction is dependent upon the quality of the copy submitted. Broken or indistinct print, colored or poor quality illustrations and photographs, print bleedthrough, substandard margins, and improper alignment can adversely affect reproduction.

In the unlikely event that the author did not send UMI a complete manuscript and there are missing pages, these will be noted. Also, if unauthorized copyright material had to be removed, a note will indicate the deletion.

Oversize materials (e.g., maps, drawings, charts) are reproduced by sectioning the original, beginning at the upper left-hand corner and continuing from left to right in equal sections with small overlaps. Each original is also photographed in one exposure and is included in reduced form at the back of the book.

Photographs included in the original manuscript have been reproduced xerographically in this copy. Higher quality 6" x 9" black and white photographic prints are available for any photographs or illustrations appearing in this copy for an additional charge. Contact UMI directly to order.

UMI[®]

Bell & Howell Information and Learning
300 North Zeeb Road, Ann Arbor, MI 48106-1346 USA
800-521-0600

HARVARD UNIVERSITY
Graduate School of Arts and Sciences



THESIS ACCEPTANCE CERTIFICATE

The undersigned, appointed by the
Division of Engineering and Applied Sciences
Department
Committee

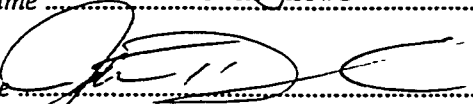
have examined a thesis entitled
"Tactile Imaging"

presented by Parris Saxon Wellman

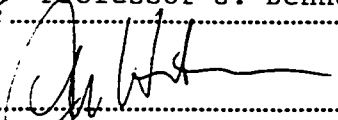
candidate for the degree of Doctor of Philosophy and hereby
certify that it is worthy of acceptance.

Signature 

Typed name Professor R. Howe

Signature 

Typed name Professor J. Dennerlein

Signature 

Typed name Professor J. Hutchinson

Date May 3, 1999

Tactile Imaging

A thesis presented

by

Parris Saxon Wellman

to

The Division of Engineering and Applied Sciences

in partial fulfillment of the requirements

for the degree of

Doctor of Philosophy

in the subject of

Engineering Sciences

Harvard University

Cambridge, Massachusetts

May, 1999

UMI Number: 9935928

Copyright 1999 by
Wellman, Parris Saxon

All rights reserved.

UMI Microform 9935928
Copyright 1999, by UMI Company. All rights reserved.

This microform edition is protected against unauthorized
copying under Title 17, United States Code.

UMI
300 North Zeeb Road
Ann Arbor, MI 48103



© 1999 Parris Saxon Wellman

All rights reserved.

Abstract

Palpation is a ubiquitous skill that we use every day, from finding a button-hole in a shirt to determining if fruit is ripe in the grocery store. Nowhere is it more important than when it is used by physicians in the discovery and assessment of disease. The problem with this technique is that it can be difficult to accurately verbalize and record tactile sensations, which makes the comparison of two manual examinations extremely difficult. This thesis presents a new medical imaging technique, tactile imaging, which promises to alleviate this difficulty through more objective documentation of clinical examinations. We present one implementation of such a system, targeted at the documentation of the properties of palpable breast lumps. It is comprised of a hand held scan head with a distributed pressure sensor mounted on it and a magnetic position tracker contained within it that is stroked across the surface of the breast by a clinician. The pressure distribution on the face of the sensor and its location in space are recorded using a computer and an algorithm assembles a composite tactile map of the structure in real time. This map is the average of all pressures recorded at a particular location in the breast as the physician examines it. In order to extract features from these maps, we have

developed mathematical models that relate material and geometric properties of palpable lumps to surface pressure distributions. These models were used to develop inversion algorithms that can be used to extract the size of the lumps imaged. In clinical tests on 25 surgical patients, size estimate accuracy (compared to ex vivo size measurements) was within 13% mean absolute error (MAE). This compares favorably to 34% and 47%, MAE, respectively, for ultrasound estimates and clinical breast examination estimates. Across multiple maps, size repeatability was within 7.5% (one standard deviation). Tactile imaging therefore promises to improve the objectivity of clinical breast examination.

First you guess. Don't laugh, this is the most important step. Then you compute the consequences. Compare the consequences to experience. If it disagrees with experience, the guess is wrong. In that simple statement is the key to science. It doesn't matter how beautiful your guess is or how smart you are or what your name is. If it disagrees with experience, it's wrong. That's all there is to it.

Richard Feynman

For Michelle

Contents

Dedication	vi
Contents.....	vii
List of Figures	xi
Acknowledgments.....	xiv
Chapter 1 Introduction.....	1
<i>1.1 Palpation as a Clinical Tool</i>	<i>1</i>
<i>1.2 Tactile Imaging</i>	<i>5</i>
<i>1.3 Research Questions and Thesis Outline.....</i>	<i>6</i>
Chapter 2 The Tactile Imaging System.....	9
<i>2.1 Introduction.....</i>	<i>9</i>

<i>2.2 The Tactile Imaging System</i>	<i>11</i>
2.2.1 System Description and Design	11
2.2.2 Clinical Technique	15
2.2.3 Tactile Mapping Algorithm.....	16
2.2.4 Determining the Reference Frame and Best Fit Plane	18
2.2.5 Accounting for Variations in Input Pressure.....	19
2.2.6 Assembling the Tactile Map.....	20
<i>2.3 Testing Methods</i>	<i>21</i>
<i>2.4 Laboratory Testing Results</i>	<i>22</i>
<i>2.5 Discussion</i>	<i>23</i>
Chapter 3 The Mechanical Properties of Breast Tissues in Compression.....	30
3.1 <i>Introduction</i>	30
3.2 <i>Methods</i>	32
3.2.1 Tissue Testing Device Description	32
3.2.4 Experimental Procedure	33
3.2.2 Analysis and Modeling.....	35
3.3 <i>Results</i>	40
3.3.1 Rubber Testing	40
3.3.2 Tissue Testing.....	41
3.4 <i>Discussion</i>	43

Chapter 4 Mechanical Modeling	49
4.1 <i>Introduction</i>	49
4.2 <i>Forward Model</i>	50
4.2.1 Forward Model Derivation.....	51
4.2.2 Finite Element Model.....	53
4.2.3 Empirical Model.....	55
4.2.4 Forward Model Validation	60
4.2.5 Forward Model Trends.....	62
4.3 <i>Inverse Modeling</i>	63
4.3.1 Invertibility.....	63
4.3.2 Inverse Model: Gaussian Fit Algorithm.....	65
4.3.3 Inverse Model: Thresholding Algorithm.....	68
4.4 <i>Laboratory Validation of Inversion Algorithms</i>	69
4.4.1 Laboratory Validation: Gaussian Fit Algorithm	70
4.4.2 Laboratory Validation: Thresholding Algorithm	71
4.5 <i>Discussion</i>	73
Chapter 5 Clinical Testing	90
5.1 <i>Introduction</i>	90
5.2 <i>Clinical Study</i>	91
5.2.1 Pilot Study Results	93
5.2.2 Surgical Study Results	95

5.3 Discussion	97
5.3.1 Examination Mode Comparison.....	97
5.3.2 Repeatability.....	99
5.3.3 Experimental Limitations	100
5.3.4 Future Work	101
Chapter 6 Conclusions	112
6.1 Discussion	112
6.2 Future Development	115
6.3 Future Applications	118
Bibliography	120
Appendix A Distributed Pressure Sensor Characterization	124
<i>A.1 Sensor Description.....</i>	<i>124</i>
<i>A.2 Characterization Methods</i>	<i>125</i>
<i>A.3 Results.....</i>	<i>125</i>
Appendix B Tactile Mapping Coordinate Frame Transformations.....	130
<i>B.1 Selection of the Best Fit Plane and Reference Line.....</i>	<i>130</i>
Appendix C Fit Constants for the Forward Model.....	135

List of Figures

Figure 1.1: “Bathsheba bathing” by Rembrandt	8
Figure 2.1: The tactile imaging system.	26
Figure 2.2: The "ideal" indenter shape.....	26
Figure 2.3: Clinical technique.	27
Figure 2.4: Tactile mapping explained.....	27
Figure 2.5: Linear normalization.....	28
Figure 2.6: Typical tactile maps of rubber models.....	28
Figure 2.7: Evaluation of the mapping algorithm in rubber models.	29
Figure 3.1: The tissue testing instrument.	46
Figure 3.2: The specimen geometry during punch indentation testing.....	46
Figure 3.3: Typical nominal strain–stress curves for five silicone rubber specimens.	47
Figure 3.4: Typical strain-stress curves for 8 different kinds of breast tissue.	47
Figure 3.5: Typical strain-stress curves at multiple indentation rates.....	48
Figure 4.1: Modeling block diagram.....	76
Figure 4.2: Anatomy of the breast.....	76

Figure 4.3: The geometry of the plane-strain finite element model.....	77
Figure 4.4: Typical output pressure distributions from the finite element model.....	77
Figure 4.5: Definition of the pressure distributions P_0, P_1, P_2 and P_F	78
Figure 4.6: The pressure distribution P_1 with no lump.	78
Figure 4.7: Two dimensional tactile mapping explained.	79
Figure 4.8: Representative pressure frames on the face of the indenter for four lumps. .	80
Figure 4.9: Representative maps for four lumps.	81
Figure 4.10: Representative single pressure frames for two lumps.	82
Figure 4.11: Problems with invertibility : identical maps.	83
Figure 4.12: Representative FEA map pressure distribution.	84
Figure 4.13: Variation in map width with lump depth.	85
Figure 4.14: Change in standard deviation of Gaussian fit with stiffness ratio.	85
Figure 4.15: Surfaces for Gaussian fit parameters.	86
Figure 4.16: The Jacobian for the Gaussian fit parameters.....	86
Figure 4.17: Forward model trends.	87
Figure 4.18: Inversion trends.	88
Figure 4.19: Comparison of a tactile map and Gaussian fit to it.	88
Figure 4.20: Inversion algorithms: rubber model validation.....	89
Figure 5.1: Tactile map of a scar and a benign lump.	104
Figure 5.2: Tactile map of a cyst.....	105
Figure 5.3: Tactile map of a benign ridge of tissue not visible on mammograms.....	106
Figure 5.4: Tactile map of and 11mm by 9mm infiltrating ductal cancer.	107
Figure 5.5: Tactile map of a 16mm by 12mm infiltrating ductal cancer.	108

Figure 5.6: Ultrasound, CBE and ex vivo maximum size comparison.....	109
Figure 5.7: Tactile imaging and ex vivo maximum size comparison.	110
Figure 5.8: Tactile imaging and ex vivo minimum size comparison.....	110
Figure 5.9: Pathology and ex vivo maximum size comparison.	111
Figure A.1: The tactile array sensor.	127
Figure A.2: Tactile array sensor transduction mechanism.....	127
Figure A.3: The air pressure chamber used to characterize the sensor.	127
Figure A.4: The tactile sensor behavior under cyclic loading.....	128
Figure A.5: Spatial response of the tactile sensor.	129
Figure B.1: Coordinate transformations required to construct a tactile map.	134

Acknowledgments

No man is an island, and I am no exception; there are a thousand people I need to thank for their help and support during this research.

I would like to thank everyone at Assurance Medical for their assistance with this work; without them it would not have been possible. They are: Denise Gagnon, Mike Kelly, Tim Last, John Luttenbacher, Paul Maguire, Brian Noble, Chris Pearson, Sharon Timberlake, Joel Weinstein and Alan West. My thanks go also to Navin Dewagan, programmer extraordinaire and Troy Roberts, fantastic engineer and all-around good guy who always went to bat for me. I also thank Michael Cundari, who took the time to mentor me and really made the collaboration work out. Thanks are also due to the good doctors, Dr. Edward Dalton and Dr. Kenneth Kern who allowed me to invade their offices and operating rooms in pursuit of this thesis. Their patience and help are greatly appreciated. I thank Dr. David Krag, whose advice and ideas were so important to the clinical protocol. I would also like to thank the women who agreed to participate in the study. Their willingness to help and care for others is remarkable and wonderful at an especially difficult time in their lives.

Thanks also go to Professor Robert Howe, my advisor, for his insight, flexibility and advice throughout my Ph.D. experience. He taught me to be a scientist as well as an engineer. I thank my committee members Professor John Hutchinson and Professor Thomas McMahon for their advice, assistance and concern. I wish Tom were around to see the thesis. I also thank Professor Jack (Jax) Dennerlein, whose wit and good nature kept me going when he was *just* a post-doctoral student in our lab. As a member of my committee he has been extremely helpful and always available to critique and advise.

All of my lab-mates and fellow graduate students deserve my thanks for their advice, good humor, and friendship. In no particular order these thanks go to Dianne Pawluk, Aram Hajian, Jae Son, Gregg Favalora, Fuji Lai, Mei Shibata, Dimitris Hristu and Kristi Morgansen. A special thanks goes to Bill Peine; comrade-in-arms, engineer, thinker and friend. Bill, should we take off our rose colored glasses yet?

I thank my family, for their patience, support and love throughout my life. My Mom and Dad, Diana and Eric, taught me to dream and to work to make my dreams come true. And my brother Kyle has shown me the meaning of persistence and perspiration.

Finally, my dearest Michelle. The dedication says it all - this thesis is as much yours as it is mine.

I am grateful for the financial support of the Division of Engineering and Applied Sciences, the Whitaker Foundation and Assurance Medical Corporation.

Chapter 1

Introduction

1.1 Palpation as a Clinical Tool

Physicians have used palpation for thousands of years in the assessment of their patients. It is a ubiquitous and invaluable clinical tool. Even in this era of highly sophisticated medical imaging technologies it is widely used in the detection and diagnosis of disease. Some examples of its utility are for palpating the thyroid gland, or feeling the liver, pancreas and other internal organs during general surgery to assess their health, or for localizing lung nodules during thoracic surgery (Mack et al. 1993). In the detection and diagnosis of breast cancer, although patients sometimes present with visible retraction or distortion of the breast as shown in Figure 1, a palpable lump is the most common symptom of the disease for which patients are referred to a breast specialist (Dixon and Mansel 1994). Palpation plays a primary role in detecting these lumps and in routine screening through recommended monthly breast self examination (BSE) and annual clinical breast examination (CBE) (American Cancer Society 1997). It is an

important tool for long-term monitoring of problematic breast lumps. Such benign lumps may be naturally occurring breast structures, such as asymmetric glandular tissue, scarring from biopsy or surgery, or benign lumps like fibroadenomas and fibrocystic tissue. These lumps can be a source of confusion with self-examination or clinical examination that may lead to missing cancerous lumps. They need to be followed, with the goal of providing a stable, repeatable breast examination (Dalton 1998).

A typical scenario in a breast clinic is that a patient is referred from her primary care physician to a breast specialist for the evaluation of a suspicious mass (Dixon and Mansel, 1994 put this number at 31% of all referrals). Often, the referring physician will give a description no better than “lump in left breast” to the specialist. Once the patient arrives the specialist locates the mass using palpation during CBE. The clinician will often then examine it using ultrasound or even order additional magnified mammograms in order to examine the lump in more detail. Often these methods do not give a conclusive indication of the nature of the mass because of factors like breast density and scarring. In these cases the specialist must rely on years of experience palpating breast lumps to determine whether the mass should be biopsied for diagnosis. Because palpation is an inexact art, many biopsies are done when the specialist feels that the lump is benign but is not sure of the diagnosis. Most biopsies (some statistics put it at 9 out of 10, Parker 1997) turn out to be benign and the lump must be followed in subsequent clinical examinations. Hence, in the case of a palpable but otherwise clinically occult lump, the best method for monitoring is clinical breast examination (Dalton 1998, Kern 1998, Krag 1998).

The problem with this method is that it is difficult to accurately verbalize and record tactile sensations, prompting one physician to remark “I can only deplore tumor size expressed in terms of fruits, nuts, or vegetables, but ... medical students ... continue to prefer these agricultural analogies” (Haagensen 1986). Even assessing the size of a lump can be problematic, as one study reports that nearly 100% change in the size of a lump is required for it to be considered a noticeable clinical change (Lavin and Flowerdew 1981). This has serious implications for the patient, because small tumor size correlates with successful treatment outcome (Harris et al. 1996). A method for accurately recording tactile sensations from physical exams would make CBE a more objective tool, and greatly improve the ability to detect changes in lumps across time. If it were also widely used in the primary care office, it could provide greatly enhanced communication between primary care physicians and breast specialists.

The difficulty in examining breasts and determining whether a lump is malignant or benign has prompted much research into alternative technologies that could supplement or even supplant ultrasound and mammograms. A number of previous researchers have proposed breast examination technologies that rely on the contrast in elastic stiffness between normal and abnormal tissues (Cespedes et al. 1993, Fowlkes et al. 1995, and Muthupillai et al. 1995). Frequently these are based on the use of an array of pressure sensors pressed into and scanned over the surface of the breast. The intended application has most often been screening, where the primary challenge is the detection of the presence of a lump in the breast (Dario, Bergamasco and Sabatini 1988, Frei, Sollish and Yerushalmi 1978, Gentle 1981, Koganezawa, Takanishi and Sugano 1991). Because the elastic stiffness contrast between normal and abnormal tissues can be quite

large (as much as 100:1 in some cases, see Chapter 3) these techniques do potentially offer increased sensitivity when compared to mammograms or ultrasound.

In contrast, the monitoring application described above assumes that the lump has been detected, and the challenge is to accurately document parameters such as lump size, shape, and hardness. Sarvazyan (1997) has proposed a method that can be used for both screening purposes and documentation purposes that uses distributed pressure measurements at the surface of the tissue to estimate the properties of breast and prostate lumps. He uses an iterative solution of a finite element model in order to estimate the properties of these lumps by matching the pressure distributions predicted by the model to those measured with the sensor. He claims that the model converges in only a few iterations, given a reasonable starting estimate. Unfortunately, there is a wide variation in the anatomy of the breast and it could be difficult to develop an accurate enough initial guess for the model. Fortunately, the prostate offers a much more constrained geometry and he has demonstrated the technique for use in imaging this organ for screening for prostate cancer (Sarvazyan, 1997). A primary difficulty with these techniques is that they are extremely complex, require elaborate instrumentation and will likely require skilled operators.

In contrast our goal was to develop a simple and easy-to-use system that can document the properties of palpable lumps in soft tissue. The system will be used directly by the physician. We have begun the development of this medical imaging technology by concentrating on the problem of documenting the results of clinical breast examination. However, this basic technology and the algorithms we have developed, with suitable modifications to account for geometric differences in the organs to be

imaged, can be readily extended. It can be used for the detection of disease in a number of other applications, such as screening for prostate cancer, or even palpating the liver and spleen during routine physical examinations. These applications share a common thread: the goal is to discover areas of tissue which are palpably different (softer or harder) than the surrounding tissue. For this thesis, we have chosen to focus on breast cancer documentation because we believe a tight focus on a problem of clinical significance coupled with frequent input from specialists in the field will produce clinically relevant technology.

1.2 Tactile Imaging

In this thesis we develop a simple method for documenting breast lumps from measurements of contact pressure. The clinician strokes a “scan head” containing an array of pressure sensors over the breast. Signal processing algorithms assemble a “tactile map” of the breast and estimate the lump parameters of size and shape. The central goal is to provide objective and repeatable documentation of palpation information in a form that is easily understood by the clinician and even the patient. These images may be incorporated into the patient record as a means of tracking lump changes across time. The technique is designed to be inexpensive, noninvasive, quick, and easy to use. It will enable follow-up examinations to be conducted frequently with minimal risk and inconvenience for the patient.

We believe that tactile imaging will provide a solution to the problem of documenting the results of physical examination. In particular, we hypothesize that tactile maps made with the tactile imaging system will provide more accurate and

repeatable estimates of lump size than the currently available widely used methods for breast examination specifically, CBE, ultrasound and mammography.

1.3 Research Questions and Thesis Outline

In order to develop an effective tactile imaging system there are five steps that need to be completed. In the first step we developed the necessary hardware and algorithms for this imaging system. In Chapter 2, we discuss the physical components of the tactile imaging system and the design choices made in its development. We also discuss the tactile mapping algorithm, which assembles many individual pressure images measured with the sensor scan head into a form which is easily understood and which also suppresses sources of noise. Rubber model experiments are presented which validate the ability of the tactile mapping algorithm to suppress noise.

In order to develop feature extraction algorithms to determine the size and shape of the lumps for documentation purposes, we need to develop a forward model that relates the geometric and tissue properties. However, very few measurements of these tissue properties have been made and thus the second step in this thesis was to measure them. We have developed a measurement apparatus and a method in order to measure the mechanical properties of breast tissue in compression and this work is the subject of Chapter 3.

These measurements are essential to the third step, which is the development of the mathematical forward model. We use the model to examine the question of invertibility – given a particular pressure distribution, is it possible to recover the properties of interest. This model was validated using rubber models under laboratory conditions. Then, as a fourth step, we used it to develop two different inversion

algorithms that take the pressure map as input, and produce the size and shape of the lump as the two diameters of an ellipsoidal model, as output. These algorithms and their evaluation in rubber model tests are also presented in Chapter 4.

Finally, to be sure that the system performs adequately in the clinic we undertook a fifth step to see if our hypothesis, that tactile imaging was more accurate and repeatable than CBE, ultrasound or mammography, is true. In Chapter 5 we discuss a limited clinical trial of surgical patients where the device was tested. In this trial we compare the size estimates made with the two feature extraction algorithms developed in Chapter 4 to the ex vivo palpable size of breast lumps after they have been extracted from the patient. We also compare the accuracy of tactile imaging to the other available modes of breast examination (CBE, ultrasound and mammogram) on these same surgical patients.

Finally, in Chapter 6 we discuss our conclusions about the system, algorithms and models. We also discuss some ideas for the future directions of this research.

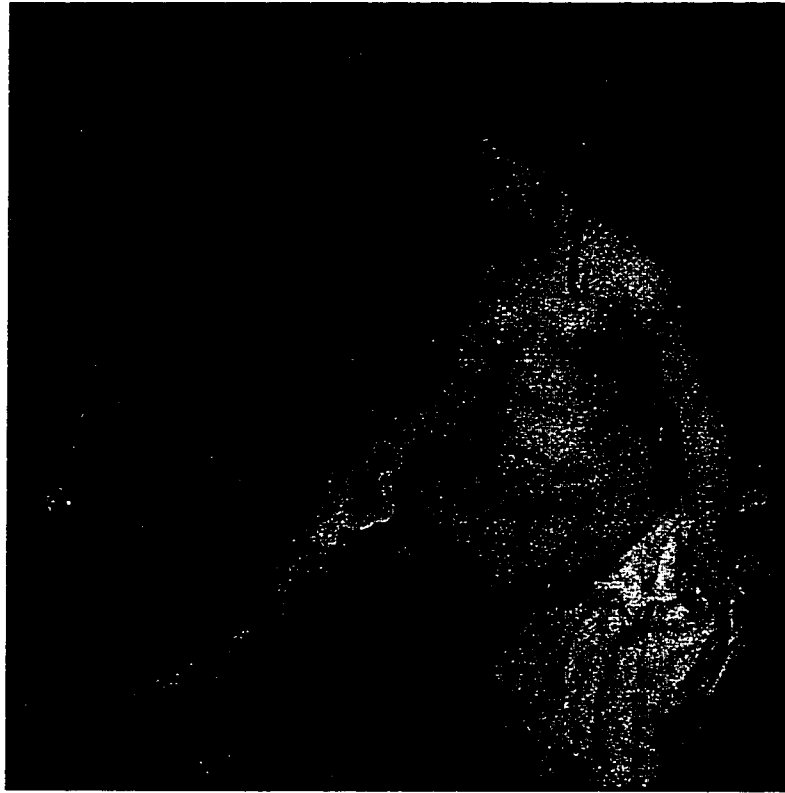


Figure 1.1: “Bathsheba bathing” by Rembrandt. Rembrandt’s mistress was the model for the painting, and there has been discussion whether or not the shadowing in her left breast represents an underlying malignancy. Obvious retraction or distortion of the breast is uncommon; the most commonly referred symptom of breast disease is a palpable breast lump. (This figure was first published in the *BMJ* by Dixon JM and Mansel RE. *ABC of Breast Disease. Symptoms Assessment and Guideline for Referral. BMJ.* 1994;309:722-726 and is reproduced with the permission of the *BMJ*.)

Chapter 2

The Tactile Imaging System

2.1 Overview

There have been a number of technologies developed to image breast lumps and aid in the detection and diagnosis of breast cancer (Cespedes et al. 1993, Manduca et al. 1996, Konofagou et al. 1996, Sarvazyan 1997). In contrast, our approach is to develop an inexpensive, quick and easy to use device that the physician can use to document the palpable features of breast masses. Better documentation of breast lump size and shape will facilitate comparison of lumps from one examination to another examination and could improve the ability to diagnose cancer.

In order to develop an effective clinical breast examination documentation system, it is necessary to make the device easy and quick to use such that the physician, and not a technician, will operate it. There are many possible configurations for such a system which could include specially modified mammogram paddles that include distributed pressure sensors on their surface (as proposed by Gentle 1981), but this would

likely restrict its use to only those patients who receive mammograms. Other possible implementations include probes mounted on robots which are used to scan the entire breast (Koganazawa, Takanishi and Sugano 1991, Dario, Bergamasco and Sabatini 1988). However, such systems are complex and require skilled personnel to operate.

Instead, we developed a system that uses a hand-held “scan-head” that has a distributed pressure sensor mounted on its surface and is used directly by the physician to make images of suspicious breast lumps. The requirements for such a hand-held system are straightforward. The force required to make images must be kept low in order to make the device comfortable for both the patient and the physician. It must be possible to image at least a 4 cm by 4 cm portion of the breast (to be sure that typically encountered lumps will be entirely contained within the image). And, there must be a way of registering the images to the patient’s body to facilitate later comparison. In this chapter we discuss the design and laboratory testing of a system that fulfills these goals. As the physician strokes the scan head across the breast, the system acquires a series of individual pressure frames, or *tactile images*, from the pressure sensor. A position tracking device that is contained in the scan head records the position and orientation of each of these frames with respect to each other. These frames are then assembled to form a composite *tactile map* of the structure that gives a more intuitive representation of the structure than the individual tactile images alone.

2.2 The Tactile Imaging System

2.2.1 System Description and Design

The system described here is the result of a tight collaboration between Assurance Medical, who lead device and product development and the author, who lead algorithm and system development. Our current implementation of a tactile imaging system is shown in Figure 2.1. The system uses a personal computer for data acquisition and analysis and a scan head that incorporates a distributed pressure sensor and a position tracking device to measure the position and orientation of the scan head in space. We track the position of the scan head in space in order to know the position of each pressure frame with respect to the others. This allows us to use an algorithm to assemble these individual pressure frames, or *tactile images*, and form a composite *tactile map* of the lump. These maps are easy for the clinician to interpret and averaging the pressure distribution measurements from many strokes provides for noise reduction in the composite map.

It is necessary to determine an appropriate size and shape for the indentation head of the device. One might argue that a finger sized head with a comparable radius of curvature would be appropriate, because it would allow the examiner to press deeply into the tissue with little input force. However, this poses a problem because we have observed that small probes like the finger produce a great deal of structure motion within the tissue and it would be very difficult to account for this motion in subsequent processing. Indentors with small radii also have large variations in the stress field across the surface of the indenter when they are pressed into tissue. These variations would make the appearance of a lump vary greatly as the head of the sensor is moved across it.

In addition, because of its small size, it could take much longer to examine the patient than is desirable. The converse of this option is to use an indenter large enough to image most of the breast at one time, which would reduce or eliminate many of these effects but could require excessive force from the examiner in order to produce adequate tissue compression. It could also fail to produce enough compression to image the lumps clearly.

The indenter needs to be large enough to image the breast in a reasonable amount of time and yet small enough to not require excessive force from the examiner. One possible shape for the indenter would be that shape which produces a uniform pressure distribution between the indenter and breast as shown in Figure 2.2(a). This means that the individual tactile images will be approximately flat (all values across the surface of the indenter are within 0.5 kPa of the mean) when indented into tissue without a lump present. These images will then clearly show the lump as a peak in the pressure distribution as the scan head passes over it. In order to produce a constant stress field across the face of the indenter, it would be necessary to make the head have two radii of curvature, e.g. be football shaped. This shape would be a difficult one on which to mount a distributed pressure sensor.

Instead, we make the assumption that the shape of the indenter is a cylinder as shown in Figure 2.1(a). This shape will produce stress concentrations at the ends but keeping the active area of the sensor confined to the central portion of the head ensures that we see a nearly flat distribution in this direction. Given this choice it is a reasonable approximation to assume that the head is long enough that we can treat it as two-dimensional (an infinitely long semi-cylinder). If this head is required to produce the

uniform normal pressure, p , as shown in Figure 2.2(a), we can find its shape by matching the shape of the deformed tissue surface that would be produced by such a pressure loading. This shape can be calculated by solving the elasticity equations that relate stress to strain and integrating to get the displacement of the surface. Johnson (1987) has done just this and we can find the shape of the deformed surface from,

$$u_z = -\frac{(1-\nu^2)}{\pi E} p \left((a+x) \ln\left(\frac{a+x}{a}\right)^2 + (a-x) \ln\left(\frac{a-x}{a}\right)^2 \right) \quad (2-1)$$

where E is the elastic modulus of the tissue, ν is Poisson's ratio, p is the average pressure and a is the half distance over which the load is applied, and u_z is the deformation of the surface. Although this shape was derived using the infinitesimal strain assumption, Konofagou et al. (1996) have shown through the use of finite element simulation that this equation can be applied in the finite strain case with which we are dealing. In our case, since the indenter will be pressing into breast tissue that can be assumed to have $E = 15$ kPa average (Krouskop et al. 1998) and $\nu = 0.5$, we can solve for this shape, provided we know the operating pressure, p . We choose to operate in the neighborhood of 10 kPa, because the total force required from the physician to produce this average pressure is acceptably low (approximately 5.4 N, for the head shown above) and tests show that it produces good images. Figure 2.2(b) shows the theoretically ideal shape for the indenter, and our single radius of curvature approximation to it. The actual shape of the head in the sensor active area is a cylinder of 3.8 cm radius and closely approximates that of the ideal shape, with mean squared difference less than 0.5%, for this input load and modulus.

Our finite element calculations demonstrate that the pressure distribution is uniform to within $\pm 3.5\%$ (absolute) at this load condition. Because equation 1 reveals that the ideal shape of the head varies with input pressure p , and elastic modulus, E we need to examine variations that are caused by these sources. We examined these variations using a finite element model of the head and tissue and allowed user input pressure to vary between 5 and 14 kPa (corresponding to the operating range of pressure) while we varied the elastic modulus of the tissue between 15 and 25 kPa, the range of values reported by Krouskop et al (1996). Within these variations the deviation of the pressure distribution from uniform across the active region of the sensor is less than 12.5% maximum, and 6.5% mean.

A close up view of the imaging scan head is shown in Figure 2.1(b). We use a piezo-resistive distributed pressure sensor mounted on the surface of the indenter. It has 416 active elements, arranged in 16 rows and 26 columns spaced 1.5 mm on center. The sensor is piezoresistive and the resistance of each element is inversely proportional to the applied pressure. The sensor range is 0 to 34 kPa, digitized to 8 bits, to give a resolution of 0.134 kPa per least significant bit. The sensor is calibrated in the clinic before each use with a pneumatic bladder to improve accuracy. The accuracy of each element of the transducer on a single sensor element basis is $\pm 10\%$, while the average of all elements is accurate to $\pm 5\%$ of full scale.

Appendix A discusses the characterization of the distributed pressure sensor. The most important discovery of the characterization process was that the pressure value reported by an individual sensor element can be considered to be Gaussian with mean equal to the applied pressure provided the sensor experiences multiple loading-unloading

cycles. This means that the applied pressure on the face of the sensor must reach zero between each cycle. In terms of user technique this means that an examiner must perform multiple strokes with the scan head. Techniques such holding the head in contact with the breast and rocking it, or sliding it in small circles, should be avoided because they will produce considerable errors in the composite map.

A six degree-of-freedom magnetic position and rotation tracker is mounted in the handle. This tracker uses pulsed DC magnetic fields to minimize its sensitivity to magnetic eddy currents produced by metals in the environment and provides the three positions and three orientation angles of the sensor in space. Positions can be resolved to 0.01 mm and rotations to 0.01 degree. All data is digitized at approximately 20 pressure images per second using a portable computer. The individual pressure images are stored for later analysis while a tactile map, described below, is created in real time and displayed on the computer monitor to provide visual feedback to the clinician.

2.2.2 Clinical Technique

Clinician imaging technique and patient placement are two important variables to control in order to obtain repeatable results. In order to minimize the errors introduced by these variations the patient is placed supine so that the breast is stabilized by gravity. The ipsilateral arm is placed over her head to help stabilize the lump and also to flatten out the breast as much as possible to improve imaging quality. Figure 2.3 shows a sketch of the typical patient position and clinical scanning pattern. The physician can image any portion of the breast (e.g. upper outer quadrant, lower inner quadrant etc.) by stabilizing it with the free hand, and performing this stroking pattern.

In order to compare the orientation of the lump being imaged from examination to examination, we use two of the patient's bony structures to serve as landmarks to orient each examination. These two structures are the sternal notch and the xiphoid, chosen because they are readily palpable on most patients and because they will not move with respect to each other between examinations. The clinician begins the examination by pressing the scan head into the tissue over each landmark when prompted by the system. The clinician then presses the sensor into the tissue directly above the suspect mass and proceeds with the examination. Typical examinations consist of multiple, overlapping strokes in a repeated raking motion over the top of the lump, shown schematically in Figure 2.3. To assist the clinician in maintaining appropriate pressure, an audible tone is generated when the average pressure on the scan head is between 5 and 14 kPa. In order to minimize the effects of patient motion, an examination is performed for at most 60 seconds. An image of the tactile map is presented on the computer monitor and the clinician is instructed to continue stroking until the map satisfactorily reflects the palpable extents of the lump. A typical tactile map takes between 30 and 60 seconds for the examiner to complete.

2.2.3 Tactile Mapping Algorithm

In order to present the sequences of individual pressure frames in a form that is easier for the clinician to interpret, the frames are combined by spatially registering and then averaging to form a tactile map of the lump. There are many reasons to create this composite map that uses all of the data in the examination, rather than single images for determining lump properties. One is that a single pressure image may not contain sufficient information to accurately represent a structure. For example, an image could

contain only half of the lump, or the lump could be difficult to discern from the background noise in the image. A single image is also sensitive to noise that is produced by variations in user technique, small tissue inhomogeneities, variations in breast thickness and sensor electronic noise. We require a method to suppress all of these sources of noise, integrate information about lumps which do not show up clearly in a single image and which produces a map that is easily understood by the clinician.

One way to do this is to collocate, assemble and average all of the images in the examination on a surface that represents the breast. The breast has a complex shape and is highly deformable but because we are interested in a local map of the palpable mass, it is a reasonable approximation to find a plane which best fits the motions of the examiner in the neighborhood of the lump. The individual pressure images are then projected onto this plane and averaged to produce the complete map. This method treats all of the sensor elements equally. This is acceptable because the pressure distribution is approximately uniform and the local deformation of a particular point is approximately the same, no matter what part of the scan head is above it. Thus averaging many elements together does not change the local pressure. Because the noise in each pressure frame is approximately Gaussian, averaging many readings effectively increases the signal-to-noise ratio of the map.

Producing a composite tactile map consists of the following steps:

- i. Determine the patient orientation and reference direction from the xiphoid and sternal notch and determine the plane that best fits the data in the neighborhood of the lump.

- ii. Eliminate the images that are outside the acceptable pressure range and account for the remaining variations in user input pressure by normalizing the value of each sensor element with the average of the frame.
- iii. Use the tracker data to determine the spatial location of each image and then project and average the value of each sensor element into the appropriate location in the tactile map (see Equation 2-5).

2.2.4 Determining the Reference Frame and Best Fit Plane

Figure 2.4(a) shows a schematic representation of the tactile map and the coordinate frames required to produce it. Frame S is the moving frame corresponding to the location of the scan head during each image while frame P is the frame corresponding to the best fit plane. The orientation and position of the best-fit plane that contains the tactile map are selected for each examination based on the motions of the scan head during the beginning of the examination. Because the orientation and location of the scan head are measured by the magnetic tracker with respect to the 0 frame, as shown in Figure 2.4(a), it is necessary to transform them to the appropriate locations in the best fit plane. It is also necessary to align this best fit plane to the reference axis defined by the sternal notch and xiphoid in order to know the relationship of the tactile map to the patient's body. The locations of each of the sensor elements in the best-fit plane can be found using,

$${}^c\rho(j,k) = T_c^s [{}^s\rho(j,k)] \quad (2-2)$$

where ${}^c\rho(j,k)$ is the location of the $(j,k)^{th}$ element of the sensor in the reference frame selected by the clinician, T_c^s , is the 4x4 homogeneous transformation from the location

of the current image to the C frame and ${}^S\rho(j,k)$ is the location of each of the elements of the sensor with respect to the center of the scan head which is frame S. Finding the location of each element in the best fit plane reduces to finding T_C^S for each of the individual pressure images. Details of the calculation of this transformation and selection of the best-fit plane are given in Appendix B.

2.2.5 Accounting for Variations in Input Pressure

Although the user is instructed to maintain a constant contact force when performing the examination, this is not strictly possible. Individual frames of pressure data are at different average pressure levels and this variation must be accounted for before including them in the map. In order to determine the relationship between average input force and peak pressure in the map, a simple experiment was conducted on rubber models. The rubber models were constructed from silicone rubber with elastic modulus 5 kPa containing hard plastic spheres that simulate cancerous breast lumps. One examiner made three different maps of the simulated breast lumps at each of nine different average pressure levels ranging between 3 kPa and 16 kPa. The average maximum pressure across the three maps at each pressure level was determined and the results are summarized in Figure 2.5. There is a linear relationship between average input pressure and the peak pressure in the map.

In order to be sure that this result holds for real breast lumps, a similar experiment was performed on two cancers during clinical testing. The clinician made three maps of each lump, at each of 6 different average pressure levels ranging between 3 kPa and 8 kPa. Figure 2.5 illustrates that in these cases as well, there is a linear relationship between average input pressure and peak map pressure. These results indicate that it is

plausible to account for variations in average input pressure by normalizing the individual pressure values, $P_i(j, k)$, in each frame by the average input pressure of that frame, F_i .

Thus

$$\bar{P}_i(j, k) = \frac{P_i(j, k)}{F_i} \quad (2-3)$$

and

$$F_i = \sum_j^c \sum_{k=1}^r \frac{P_i(j, k)}{r \cdot c} \quad (2-4)$$

where r is the number of rows and c is the number of columns in the sensor image, and $P_i(j, k)$ is the pressure at the $(j, k)^{th}$ element.

The sensor output from each element saturates at 34.5 kPa. If we were to allow images with saturated elements to be added to the map, this could produce errors in the pressure at each location in the map as well as making the individual image means untrustworthy. Thus, images that have saturated sensing elements are excluded.

2.2.6 Assembling the Tactile Map

Once the locations of the sensor elements are found with respect to the reference plane, each pressure frame from the sensor is normalized for input force and frames with saturated pixels are rejected, it is a straightforward matter to construct the tactile map. The pressure at each point in the tactile map can be found by sub-sampling the individual pressure elements into a three by three matrix so that each element in the matrix has the same value as the original sensor element, which effectively triples the resolution of the map. They are then projected onto the image and averaged at each element location as shown schematically in Figure 2.4(b),

$$P_{map}(l, m) = \frac{\sum_{i=1}^n \sum_{j=1}^r \sum_{k=1}^c P_i(j, k) \cdot q(j, k, l, m)}{\sum_{i=1}^n \sum_{j=1}^r \sum_{k=1}^c q(j, k, l, m)} \quad (2-5)$$

where $P_i(j, k)$ is the pressure of the $(j, k)^{th}$ element of the i^{th} data image, $P_{map}(l, m)$ is the pressure of the $(l, m)^{th}$ element within the tactile map and

$$q(j, k, l, m) = \begin{cases} 1 & l = \lfloor T_c^S [\rho(j, k)]_x \rfloor \quad m = \lfloor T_c^S [\rho(j, k)]_y \rfloor \\ 0 & otherwise \end{cases} \quad (2-6)$$

The denominator serves the role of a counter to see how many elements have passed over a particular location in the map to make sure that the average is properly weighted, and q is a function which maps the elements in each individual image to the correct map elements. In this equation $\lfloor T_c^S [\rho(j, k)]_x \rfloor$ is the x location of the $(j, k)^{th}$ sensing element with respect to the magnetic tracker (S frame) and $\lfloor T_c^S [\rho(j, k)]_y \rfloor$ is the y location of the $(j, k)^{th}$ sensing element with respect to the S frame. The mathematical floor operator is $\lfloor \rfloor$ which is used to truncate the index to the next lower integer; the round or ceiling operation would produce comparable results.

2.3 Testing Methods

We have taken a two-fold approach to assessing the repeatability and accuracy of the composite tactile maps. First, five examiners mapped 4 different rubber bench models of the breast, and we evaluated the repeatability of the tactile map as a function of examiner technique and number of strokes made with the scan head. Second, as discussed later in Chapter 5, we use the inversion algorithms developed in Chapter 4 to determine the size estimate accuracy and repeatability on these same rubber models.

The rubber bench models of the breast were made of a uniform layer of silicone rubber that has an elastic modulus of approximately 5 kPa (similar to fatty breast tissue at low strain levels). Four acrylic spheres that simulated cancers (12.5 mm, two 15.5 mm and 22.0 mm) were mounted to the rigid backing of the models and covered to different depths in the silicone rubber. The 12.5 mm lump was 11.3 mm deep, the 15.5mm lumps were 15.5 and 23.3 mm deep and the 22.0 mm lump was 27.5mm deep. All depths are reported from the surface of the model to the center of the lump. The lump sizes were chosen to span the typical range of sizes that would be encountered in a clinical setting. In addition, the 15.5 mm lump was placed at two depths in order to determine if the later size estimates show any significant variation with the depth of the lump, or if the map shows any significant difference in variation because of geometry.

Five different examiners used the imaging device to make two kinds of tactile maps of the lumps using two different stroking techniques. The first kind of map was made from ten strokes in a single direction and each examiner completed three trials. The second kind of map used multiple strokes from many different directions and subjects were instructed to continue to map the lump until its visual appearance in the map no longer changed. Each examiner made three different maps of this second kind.

2.4 Laboratory Testing Results

Figure 2.6 shows three typical tactile maps generated by one examiner making ten strokes in the same direction on the model with the 12.5mm diameter, 11.3mm deep lump. Maps of each lump were created after each of the strokes, and the percent root mean squared (*%RMS*) difference between them and the map created after the final (tenth) pass was computed as

$$\%RMS = 100 * \frac{\sum_{i=1}^r \sum_{j=1}^c (P_{map,k}(i, j) - P_{map,10}(i, j))}{\sum_{i=1}^r \sum_{j=1}^c \frac{P_{map,10}(i, j)}{r \cdot c}} \quad (2-7)$$

where $P_{map,k}(i, j)$ is the pressure at the $(i, j)^{th}$ location of the k^{th} map. Figures 2.7(a) and 2.7(b) summarize the results of this experiment. Figure 2.7(a) shows the $\%RMS$ difference in the map averaged across each examiner and shows little difference among subjects. Figure 2.7(b) shows curves for the trials averaged across lump size and depth and demonstrates no systematic variation with lump geometry. Both sets of curves show a similar shape, and fall to less than 2.5% variation (mean) after seven passes.

2.5 Discussion

While characterizing the sensor we discovered that the noise in a particular sensor element can be modeled as Gaussian provided multiple strokes with the pressure falling to zero between them are included in the sequence of images analyzed. Thus proper technique is essential in order to produce repeatable, accurate tactile maps. We have also seen that proper technique is easy to specify, we simply instructed examiners to make maps using a repeated stroking motion and to continue mapping until the map accurately reflects the perceived palpable extents of the lump. Our rubber model experiments showed that map repeatability was within 2.5%, independent of choice of technique across examiners, and validates that these instructions are adequate.

The tactile mapping algorithm is also successful at suppressing the noise that is present in the individual frame readings. We have shown that each individual sensor element has about a 5:1 signal to noise ratio on a single image basis. Given this level of noise on the input images, what is the signal to noise ratio of the composite tactile map?

This question can be answered by looking at the maps in Figure 2.6(c) far from the lump. In these areas, the value of the map should be 1, since that is the value to which we normalize. One standard deviation of a 20 x 20 element section of the map is 0.45%. This implies that 95% of the elements fall within +/- 1% of the mean and therefore the signal to noise ratio on the map level is about 50:1. This should not be surprising because we know the sensor noise is Gaussian, and each element in the map is the average of about 120 sensor elements that have passed over it. Basic signal processing tells us that we should expect the noise to decrease by the square root of the number of samples averaged, or in this case about a factor of ten.

While this algorithm is successful at suppressing the noise in the individual frames that is due to changes in sensor gain, variations in user technique and other sources, it does introduce some limitations to the tactile mapping process. First among these is that the lump is not truly registered to the patient's breast, but rather to the patient's sternum. Because the breast is a pendulous organ, it is possible that the lumps will be in different locations with respect to it depending on patient positioning. Properly placing the patient supine with her arm raised should alleviate this difficulty. Second, because the scan head is tracked with respect to a fixed location in space, it is imperative that the patient does not move with respect to it. Again, this can be accomplished through proper patient placement and by instructing the patient not to move during the course of the examination. Third, the validity of the best-fit plane as an approximation to the breast in the neighborhood of the lump is unknown. The effect of these limitations will be evaluated clinically as discussed in Chapter 5.

As successful as the tactile mapping algorithm is at suppressing noise, it may be useful to have access to the data on a tactile image by tactile image level in order to develop sophisticated feature extraction algorithms. However, it is necessary to reduce the amount of noise present in each frame. One possibility is to develop algorithms that average the sensor readings by averaging the sensor values for coincident locations and orientations of the scan head. While this sounds appealing, in practice, there are far too few frames that fall in exactly the same location to make this practical. An alternate way to get at the same information is to recognize that the pressure on each sensor element may vary from location to location on the surface as it is stroked across the tissue. Making composite maps which treat each sensor element as unique is perhaps one way to extract this information.

The other problem with this algorithm is that it assumes that we are only interested in a particular location on the breast. While this is certainly true in many cases, there are a fraction of cases where the physician would like to map the whole breast (Dalton 1998, Kern 1998). The problem is that the breast is a pendulous, mobile organ. To get repeatable results, it would be necessary to fix the breast the same way for each examination. This might be accomplished by using the nipple as a location landmark, and then stretching a flexible sheet over the breast to flatten it in a repeatable way for each examination. Individual maps could be made of each quadrant of the breast, and the results saved for later comparison.

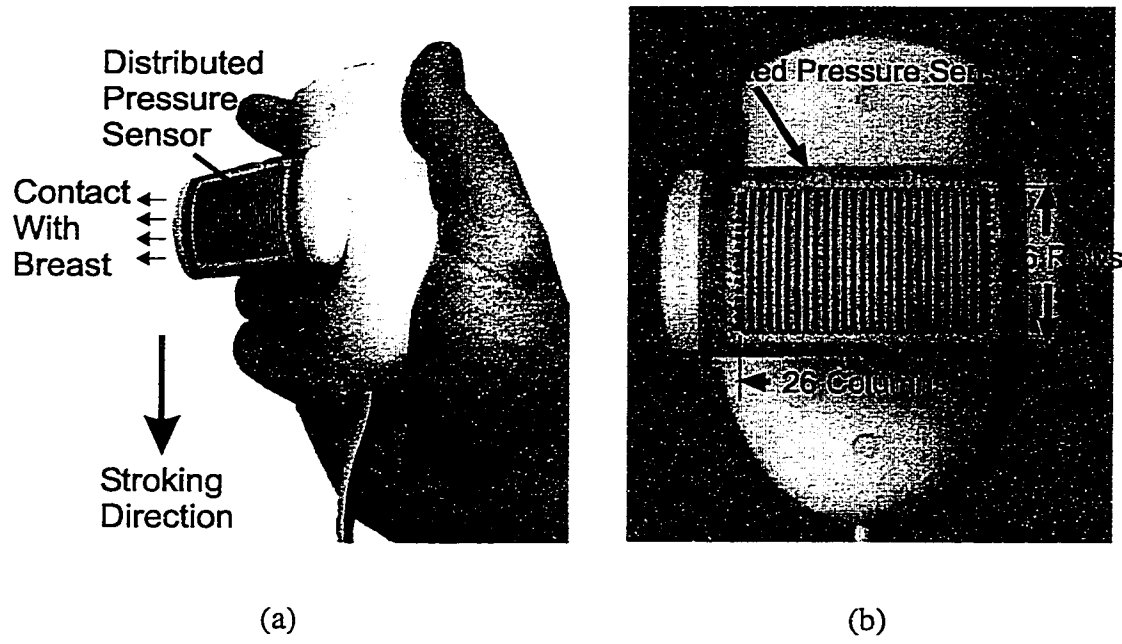


Figure 2. 1: The tactile imaging system comprises a hand-held scan head and a personal computer to acquire the pressure and position data. (a) The shape of the scan head is a section of a cylinder to produce a nearly constant pressure distribution when indented into soft tissue. (b) The scan head has a 16 x 26 element tactile array sensor which measures the pressure on the surface of the head at each sensor location and also contains a magnetic tracker to determine the position of the head.

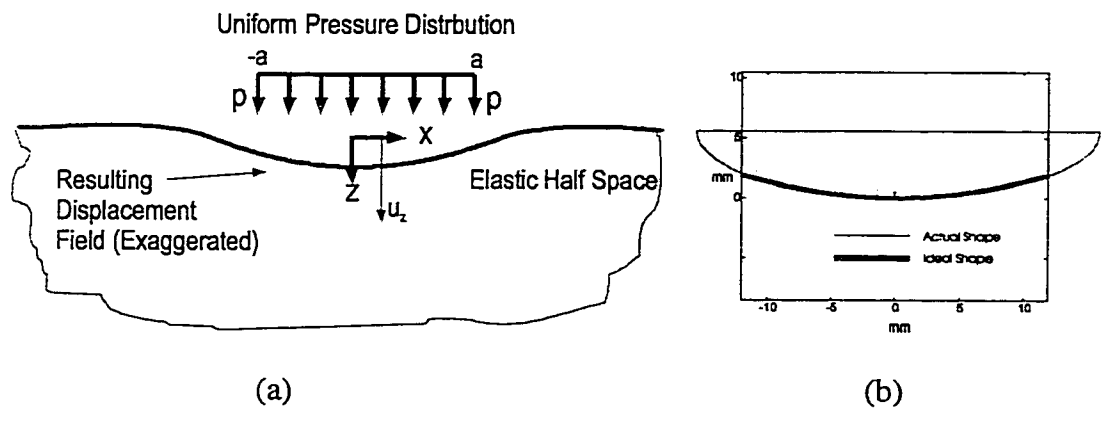


Figure 2. 2: The desired pressure distribution (a) and the shape of the indenter required to produce it (b) for an indentation pressure of 10 kPa and an elastic modulus of 15 kPa (which correspond to our desired indentation pressure and the nominal elastic modulus of the breast tissue to be compressed).

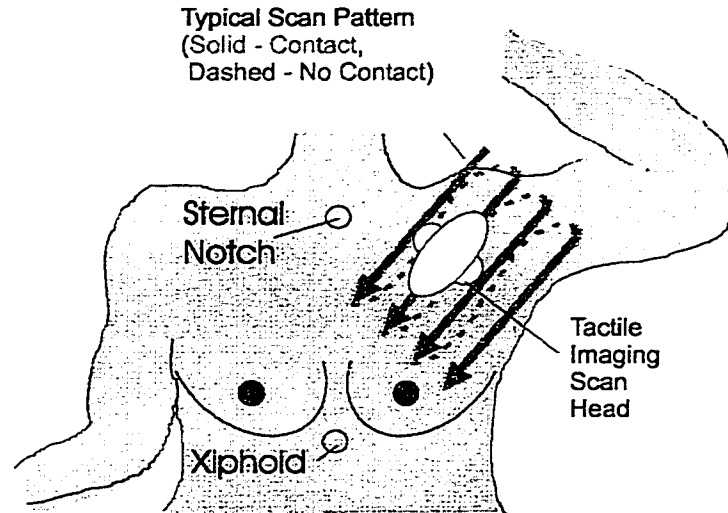


Figure 2. 3: The patient is placed supine with the ipsilateral arm over the head to stabilize the breast and minimize tissue thickness. The clinician begins the examination by indicating the location of the readily palpable sternal notch and xiphoid to facilitate comparison of follow-up examinations. The clinician then presses the indenter into the breast near the mass, and strokes the sensor repeatedly over the area of the mass and its immediate surroundings. The skin surface is lubricated to minimize friction.

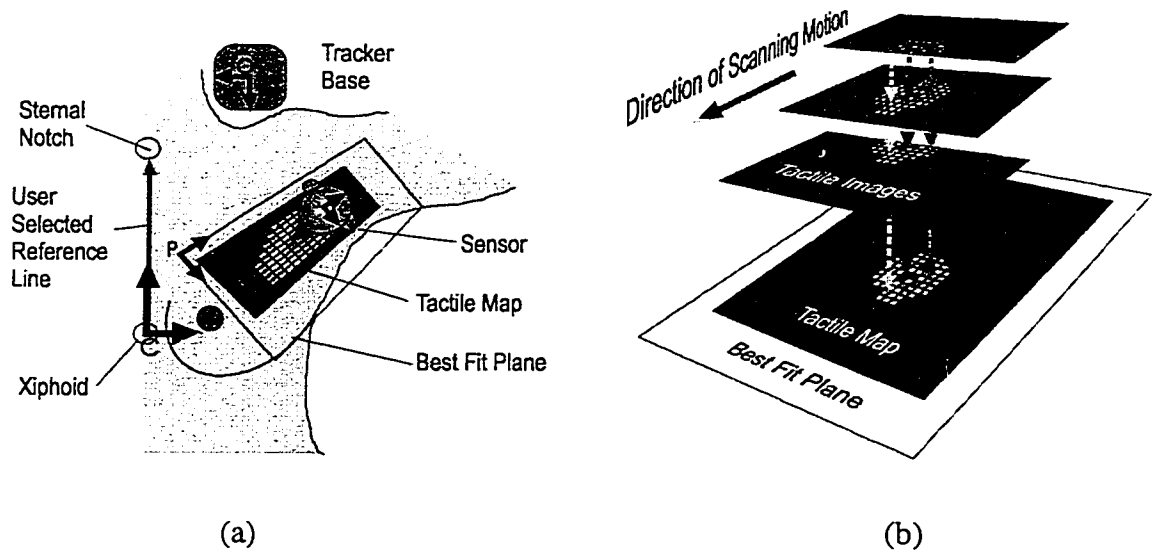


Figure 2. 4: (a) A tactile map is registered to the patient using coordinate frame C , determined by the sternal notch and xiphoid. Frame S is the location of the scan head during each image, frame P is the best-fit plane frame and Frame O is the base frame for the position tracker. (b) A tactile map is created by collocating each image, projecting and averaging the values onto the plane that best fits the sensor motion in the neighborhood of the mass.

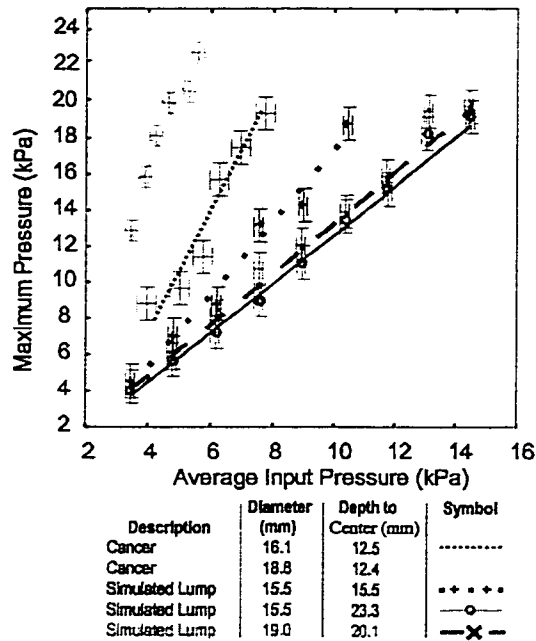


Figure 2. 5: The peak pressure scales linearly with the input force in rubber models and in clinical measurements made on cancerous lumps.

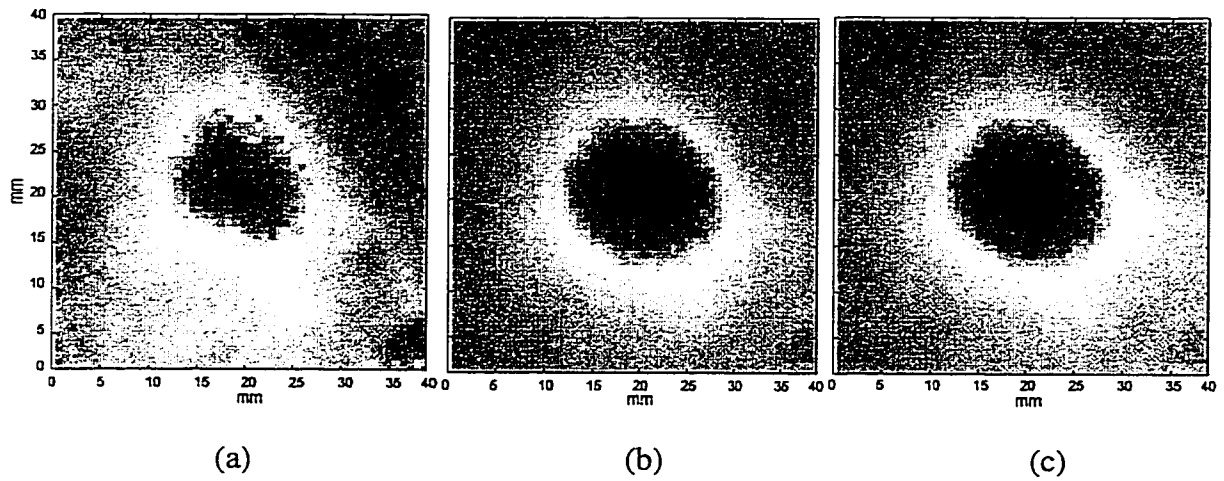


Figure 2. 6: Typical tactile maps of the 12.5 mm, 11.3 mm deep acrylic sphere. The map after (a) one stroke, (b) 7 strokes and (c) 10 strokes. There is a 23% RMS difference between the map in (a) and the map in (c), while there is only a 2.2% RMS difference between the map in (b) and the map in (c).

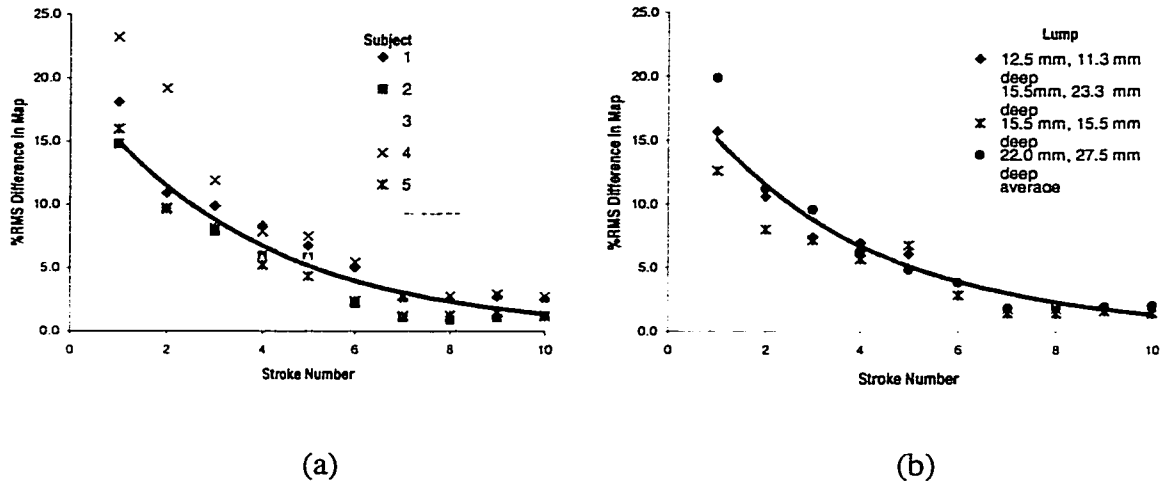


Figure 2. 7: Average percent RMS difference between the map formed after the tenth stroke and the maps after each of the nine strokes preceding it. (a) Trials on 4 different lumps are averaged for each subject, after six passes, the difference in the maps falls to less than 2.5%. (b) The trials performed by each examiner are averaged for each lump size and depth.

Chapter 3

The Mechanical Properties of Breast Tissues in Compression

3.1 Introduction

The breast is a many layered, inhomogeneous structure composed of many different kinds of tissue. The two predominant types of tissue within the breast are fat and normal glandular tissue which supports lactation. The contrast in elastic stiffness between these normal tissues and abnormal breast tissue has long been recognized (Harris et al. 1994). Many researchers have proposed techniques for examining abnormal breast tissue that rely upon the elastic contrast in order to image them (Garra et al. 1997, Lerner et al. 1987, Chenevert et al. 1997). Typically these techniques make images of the tissue at two different applied loads and compute a displacement field from them. This displacement field is then used to infer the stiffness of the tissue, given assumptions about the stress field. Other researchers have proposed techniques that rely on pressure distribution measurements made at the surface of the tissue when it is loaded (Gentle

1988, Sarvazyan 1997). There has also been some work to non-invasively measure the stiffness of tissue by measuring the propagation of elastic shear waves using magnetic resonance imaging (Muthupillai et al. 1995).

While these researchers have discussed visualizing the tissue stiffness distribution within a breast, there is surprisingly little available in the literature on its mechanical properties. In addition there is little formal work that relates the histological nature of the tissue directly to the estimated stiffness. While most biological tissues display both a viscous (velocity dependent) and elastic response, the great majority of the force developed in the palpation process can be attributed purely to the elastic response. Given this observation, in order to develop tractable mathematical models with which to characterize material properties, most researchers have idealized the tissue to be isotropic and elastic (Hayes et al. 1971, Krouskop et al. 1998, Sarvazyan, Skovoroda, Emelianov et al. 1995, Skovoroda et al. 1995, Zhang, Zheng and Mak 1997). In addition, the usual assumption is that the tissue is nearly incompressible, which has proven to agree well with experiment (Fung 1993). With these assumptions, it is possible to define the mechanical behavior of the tissue using a single elastic or shear modulus.

Under these assumptions, Skovoroda, Klishko and Gusakyan et al (1995) reported a study of 150 specimens of normal, fibroadenomatous and cancerous tissues which showed that fibroadenomas are typically 4 times as stiff as normal tissue, while cancer can be as much as 7 times as stiff. The authors used measurement of propagating elastic strain waves to estimate the stiffness at small strain, but do not provide a characterization for a more complete range of strain. Krouskop et al. (1998) recognized that the non-linear behavior of breast tissue requires the computation of an elastic modulus at more

than one strain level. At 5% strain he found that the ratio of the elastic modulus of cancerous tissue to that of fat was 5:1, while at 20% strain the ratio grew to 25:1. However these previous characterizations give at most a two-point measurement of the stress-strain relationship and do not characterize it adequately for all strain levels. Any new method of documenting and diagnosing breast cancer through stiffness measurements needs a thorough characterization of the tissue across a large range of strain, and that is one focus of this study.

We are also attempting to answer a more fundamental question: is there a relationship between tissue stiffness or change in the stiffness and histological diagnosis? To answer both of these questions we have made a series of measurements of the mechanical properties of a variety of breast tissues, both normal and abnormal, in compression. We have computed their elastic moduli and the constants to an exponential fit to the stress-strain data computed from force displacement data measured during punch indentation tests. In the remainder of this chapter we discuss the methods used to extract the elastic moduli at different strain levels of the tissue from the force-displacement curves, the verification of these methods in rubber samples and the results of our testing.

3.2 Methods

3.2.1 Tissue Testing Device Description

We have constructed a portable testing device that can be used in the operating room to measure the mechanical properties of tissue immediately after it is removed from the body because it is unknown how much these properties change with time (Fung 1993). The testing instrument shown in Figure 3.1(a) is used for both uniaxial

compression tests and punch indentation tests of tissue. A vacuum clamping fixture stabilizes the resected sample that has been cut to a uniform thickness and placed directly beneath the indenter as shown in Figure 3.1(b). The examiner applies repeated loads to the sample with a 4mm diameter flat-bottomed punch. The position of the punch and the force applied by it are measured using a precision linear potentiometer and a uniaxial load cell. These two transducers are digitized at 2 kHz using a 16 bit PCMCIA analog to digital card (PCMCIA16XE50, National Instruments Corp., Austin TX) and data acquisition software running on a laptop computer. The load cell (Omega Miniature F1000, Omega Engineering Ltd., Stamford, CT) with accuracy of 12mN (maximum deviation from linear across the full scale range). After digitization, the noise level is 3.3 mN (RMS). The linear potentiometer (Midori GreenPot LP100F-5K, Midori America Corporation, Fullerton, CA), has a range of 100 millimeters. The potentiometer has accuracy better than 11 μm (maximum deviation from linear) with a noise level of 11.5 μm (RMS) after digitization. Given a maximum load of 9.8 Newtons, applied over a minimum resolvable distance of 11.5 μm , these noise specifications imply that the maximum resolvable elastic modulus is on the order of 68 MPa for a 1mm thick sample and a 4mm diameter punch. The maximum elastic modulus that can be measured is therefore set by the intrinsic mechanical stiffness of the instrument with the 4 mm punch in place and is measured at 28 MPa, assuming a 1mm thick sample.

3.2.4 Experimental Procedure

In order to assess the accuracy of the instrument, five rubber tissue phantoms were constructed from silicone rubber, each with a different stiffness. These phantoms were molded to 5 cm in diameter and 1 cm thick. Cubes 1 cm on a side were cut from the

phantoms. Uniaxial compression tests using a 40 mm diameter flat plate mounted in place of the 4 mm punch on the testing apparatus were made of each sample. Each rubber sample was well lubricated by submerging it in mineral oil to minimize any effect of friction at the interface between sample and plate. The cubes were sectioned into specimens 2 mm and 5 mm thick and subjected to punch indentation tests using the 4mm diameter flat-bottomed punch. Again, they were submerged in mineral oil.

The breast tissues tested in this study were obtained during surgery after patients had signed a written informed consent document. To minimize any errors introduced from tissue aging after it is removed from the body, the fresh tissue samples were tested in the operating room within 10 minutes of excision, and the surgeon identified the gross type of the tissue (e.g. tumor, surrounding fat, gland etc.) A sample of the tissue was removed from the full specimen. The remainder was sent to a pathologist for a histological diagnosis (e.g. infiltrating ductal carcinoma). Each sample was resected to a minimum of 10mm by 10mm and a minimum thickness of 2 mm and then fixed onto the vacuum clamping apparatus shown in Figure 3.2. The samples were kept hydrated by periodic application of saline solution, and were tested at room temperature (21 °C +/- 2.5 °C). We preconditioned the samples 10 times with a 2 N load, which was chosen to keep the peak strain in the cancerous tissue samples at less than 10% to prevent damage to the tissue.

We investigated the variation in tissue modulus that is caused by viscous effects by varying the indentation speed. In order to examine the viscous behavior the data were recorded at a minimum of four strain rates. Because the instrument is hand operated it was not possible to set the strain rate exactly. These measurements were made at

approximately 50 percent/second, 200 percent/second, 1000 percent/second and 2000 percent/second. At least ten indentation trials were performed on each specimen.

3.2.2 Analysis and Modeling

In order to determine the elastic moduli of the tissue at various strain levels we need a mathematical model that relates the nominal stress and nominal strain developed during punch indentation tests to these moduli. We will assume that the different types of tissue (tumor, normal glandular, fat etc.) can be modeled as homogeneous, and that their behavior in compression can be modeled as approximately isotropic. Further, we will make the assumption, in keeping with results reported for other soft tissues (Fung 1993), that the tissue is approximately incompressible. This implies that the Poisson ratio is 0.5, and that only an elastic modulus is required to characterize the tissue - provided we also assume that viscous effects are negligible. Further, since we will be testing relatively thin samples of tissue, we need a method that accounts for the change in apparent stiffness that is a result of geometric non-linearity.

If the sample were linear elastic with constant modulus, and we were testing a sample in uniaxial compression we could write

$$\sigma = E\varepsilon \quad (3-1)$$

where $\sigma = \frac{F}{\pi a^2}$ is the stress on a sample of radius a being compressed by a force F , and

$\varepsilon = \frac{(x - x_0)}{h}$ is the strain in a sample which is h thick during indentation. If we assume

that the location of contact, x_0 , is known, it can be subtracted from the displacement to yield the compression of the tissue, so $x_0 = x$. Substituting these relations into Equation

(3-1) yields

$$E = \frac{h}{\pi a^2} \frac{F}{x}. \quad (3-2)$$

We require an analogous relationship for a punch indenting a thin sample of material.

Hayes et al. (1971) developed a relationship between the force-displacement curves measured during a punch indentation test of a thin layer of tissue to the elastic modulus of the material. Zhang, Zheng and Mak (1997) extended this model to include large deformations. This model suggests that

$$F = \frac{8E}{3} axK\left(\frac{a}{h}, \frac{x}{h}\right) \quad (3-3)$$

provided the material is incompressible (Poisson ratio = 0.5). Figure 3.2 shows the specimen geometry during punch indentation testing. The position of the indenter is x , the location of the plate is C and the input force is F . The punch radius is given as a , while the thickness (prior to compression) of the sample is h . Inspection of Zhang, Zheng and Mak's (1997) model reveals that

$$K = K_0 + K_1 \frac{x}{h} \quad (3-4)$$

where K_1 and K_0 are functions of specimen and punch geometry (a/h) alone, and are constant for a particular sample. These values, for Poisson's ratio = 0.5, are given in Table 3.1.

a/h	K		<i>Fit Constants</i>		
	K_0	K_1	$x/h = 0.01$	$x/h = 0.1$	$x/h = 0.15$
0.2	1.23	1.26	1.24	1.36	1.42
0.4	1.68	1.67	1.70	1.85	1.93
0.6	2.15	3.01	2.18	2.45	2.61
0.8	2.75	4.63	2.80	3.19	3.45
1.0	3.54	5.66	3.59	4.11	4.38
1.5	5.90	16.48	6.08	7.51	8.40
2.0	8.81	28.04	9.11	11.56	13.05

Table 3. 1: Constants $K = K_0 + K_1 \frac{x}{h}$ for the fit to Zhang's (1997) correlation ($r^2 = 1.00$ for all fits) for Poisson's ratio=0.5.

We can find E in terms of nominal stress and nominal strain by substituting Equation 3-4 into Equation 3-3 to get

$$\sigma_n = E \frac{8h}{3\pi a} (K_1 \varepsilon_n^2 + K_0 \varepsilon_n) \quad (3-5)$$

where $\sigma_n = \frac{F}{\pi a^2}$ and $\varepsilon_n = \frac{x}{h}$. Thus we can fit the data, provided it displays a nearly linear response using

$$\sigma_n = \mu (K_1 \varepsilon_n^2 + K_0 \varepsilon_n) \quad (3-6)$$

and find that

$$E = \frac{3a\pi}{8h} \mu. \quad (3-7)$$

The constant μ can be found using regression from the nominal stress-strain measurements.

However, the tissues being tested display an exponential stress-strain response and we must also account for the geometric nonlinearity introduced by the thinness of the sample in a manner analogous to that developed for linear materials in Equation 3-5. We expect the relationship to be exponential, since many other tissues display this kind of response (Fung 1993, Pawluk 1997). Above, we assumed that we knew exactly where

the location of contact between the indenter and the tissue was, which is not really the case. This practical difficulty is introduced by the exponential stress-strain response which make it difficult to accurately locate the point of zero strain because the slope goes to zero at $x=0$, which makes the zero crossing obscured by noise. We can find the point of zero strain if we model the data as

$$F = \frac{b}{m}(e^{m(x-x_0)} - 1) \quad (3-8)$$

where F is the total force on the indenter, x is its displacement, x_0 is the point of first contact with the tissue as shown in Figure 3.2 and b and m are constants for the material. This equation is analogous to that presented by Fung (1993) for tissues of constant cross section and can be solved if we take a derivative to get

$$\frac{dF}{dx} = mF + b . \quad (3-9)$$

A line can be fit to the data to find the slope m and intercept b (Fung 1993). The derivative was computed numerically by first filtering the data forwards and backwards in time to eliminate phase shift with a 4 pole symmetric digital low pass filter with cutoff frequency at 500 Hz. This frequency was chosen because the maximum frequency of interest in the data was 100Hz, and the noise was at approximately 1000 Hz. We computed $\frac{dF}{dx}$ by numerically differentiating the force with respect to position using a 5 point interpolating polynomial for unequally spaced points (Atkinson 1989). The value for x_0 was then found using a simplex search routine to minimize the squared error. Once the value for x_0 was found, we subtracted it from the displacement and we determined the thickness of the sample, $h=C - x_0$, as shown in Figure 3.2 where C was measured during

the experiment. The data were then scaled to nominal stress, $\sigma_n = \frac{F}{\pi a^2}$ and nominal

strain, $\varepsilon_n = \frac{x}{h}$ and we fit the curve

$$\sigma_n = \frac{b'}{m'} (e^{m'\varepsilon_n} - 1). \quad (3-10)$$

Now we assume that Zhang, Zheng and Mak's relationship still applies and we equate Equation 3-5 and Equation 3-10. We solve for the elastic modulus as a function of nominal strain and sample geometry to get

$$E = \frac{3a\pi}{8h(K_1\varepsilon_n^2 + K_0\varepsilon_n)} \frac{b'}{m'} (e^{m'\varepsilon_n} - 1). \quad (3-11)$$

To further simplify this expression, we desire values for b' and m' that relate stress and strain directly to E and do not depend on sample geometry. These constants can then be used to determine the elastic modulus of the material as a function of nominal stress and nominal strain alone. We define, analogous to Equation 3-1,

$$\sigma_n^* = E \cdot \varepsilon_n \quad (3-12)$$

in which σ_n^* is calculated from the nominal strain, ε_n , and E as defined by Equation 3-11.

It can be thought of as the stress that would have been produced if the sample thickness did not produce a geometric nonlinearity. We observe from the data that this new curve can be fit by an exponential

$$\sigma_n^* = \frac{b^*}{m^*} (e^{m^*\varepsilon_n} - 1) \quad (3-13)$$

which allows us to calculate E directly from the constants b^* and m^* . Differentiating Equation 3-13 with respect to ε_n (and ignoring the small variation in b^* with strain) gives

$$E = b^* e^{m^*\varepsilon_n} \quad (3-14)$$

because $\frac{\partial \sigma_n^*}{\partial \varepsilon_n} = E$.

If we examine the original equations this should not be surprising because if we substitute Equation 3-11 into Equation 3-12 and then equate this with the right hand side of Equation 3-13, we get

$$\frac{3\pi a}{8h(K_1\varepsilon_n + K_0)} \frac{b'}{m'} (e^{m'\varepsilon_n} - 1) = \frac{b^*}{m^*} (e^{m^*\varepsilon_n} - 1) \quad (3-15)$$

from which we see that $m^* = m'$ and $b^* = \frac{3\pi a}{8h(K_1\varepsilon_n + K_0)} b'$. Examining Table 3-1

reveals that the expression $(K_1\varepsilon_n + K_0)$ varies by less than 15% for the samples tested (which were at least 2mm thick).

Once the stress-strain data were recorded, they were analyzed and curves fit to them to determine the exponential fit constants and the elastic moduli at various levels of strain. Quality of fit was computed from variation accounted for, *VAF*, which is in turn computed from fractional mean squared error,

$$MSE = \frac{\sum_{i=0}^n (\sigma_{measured}(i) - \sigma_{fit}(i))^2}{\sum_{i=0}^n (\sigma_{measured}(i) - \bar{\sigma}_{measured})^2} \quad (3-16)$$

and *VAF* is simply

$$VAF = 1 - MSE. \quad (3-17)$$

3.3 Results

3.3.1 Rubber Testing

Figure 3.3 shows representative nominal strain - nominal stress curves for the rubber samples tested for both punch-indentation tests and the uniaxial compression tests. Table 3.2 summarizes these results. The variation across multiple trials and across both sample thickness is less than 2.7%. while the variation across trials for a particular sample thickness is 1.9%. There is good agreement between the elastic moduli predicted

from the uniaxial tests and the punch indentation tests, with the slope of the best fit line = 1.08 ($r^2 = 0.99$). The average deviation of the uniaxial compression is less than 4%.

Sample Number	1	2	3	4	5
Punch Average.	2.1	4.5	10.5	425	2370
Punch Standard Deviation.	0.04	0.2	0.3	13.9	25.8
Variation Accounted For	0.992	0.995	0.996	0.998	0.995
Uniaxial Compression Average.	2.5	5.0	11.4	446	2130
Uniaxial Standard Deviation	0.06	0.5	0.5	10.2	19.4
%difference	-16.0	-10.0	-7.9	-4.8	9.9

Table 3. 2: Elastic moduli of five different silicone rubber samples. All punch trials are averaged across sample thickness since the elastic modulus values estimated for both sample thicknesses tested were within 1.8% (less than one standard deviation) of each other. The slope of the best-fit line between the two methods is 1.08 ($r^2=0.99$).

3.3.2 Tissue Testing

Figure 3.4 shows that there is a wide range in behavior for the various samples of tissue tested. Carcinomas are seen to be highly nonlinear and quite stiff, while fat is nearly linear and extremely soft. Figures 3.5(a) and 3.5(b) reveal, somewhat surprisingly, that there is very little variation (less than 5%) in elastic modulus that depends on strain rate and confirms Krouskop's (1998) finding. Tables 3.3 and 3.4 summarize the results of the testing for the various specimens. The values in Table 3.4 were computed from Equation 3-14 and are extrapolated to 15% strain for the cancer specimens. Pilot testing revealed that the cancer specimens were damaged by application of strain greater than 10% (the elastic modulus of the specimen at all strain levels permanently decreased when they were subjected to larger strains).

Tissue Type	N	m^*	SD	b^*	SD	VAF (%)
Fat	26	7.4	4.0	4460	2350	98.2
Gland	7	12.3	7.4	15100	6750	96.7
Phyllodes Tumor	1	11.9	0.0	50300		95.9
Papilloma	2	21.4	2.8	17700	4200	98.3
Lobular Carcinoma	1	20.9	0.0	2820		96.5
Fibroadenoma	5	20.0	1.4	37500	6040	99.4
Infiltrating Ductal Carcinoma	25	19.9	5.5	37900	6140	97.6
Ductal Carcinoma in Situ	1	24.4	0.0	55700		97.2

Table 3. 3: Average fit parameters for the exponential fit $\sigma_n^* = \frac{b^*}{m^*}(e^{m^* \epsilon_n} - 1)$, standard deviations of the parameters across specimens (SD), percent mean squared error (MSE) and number of samples, N , for each of eight different types of breast tissue tested. No standard deviation is reported for those types for which there was only one specimen.

Tissue Type	N	Elastic Modulus at Strain	SD	Elastic Modulus at Strain	SD	Elastic Modulus at Strain	SD	Elastic Modulus at Strain	SD
		0.01		0.05		0.10		0.15	
		(kPa)	(kPa)	(kPa)	(kPa)	(kPa)	(kPa)	(kPa)	(kPa)
Fat	26	4.8	2.5	6.6	3.7	10	7.9	17	8.4
Gland	7	18	8.6	33	12	88	66.7	270	170
Phyllodes Tumor	1	57		91	8.6	160		300	
Papilloma	2	22	5.8	54	20	170	80.6	540	210
Lobular Carcinoma	1	35		79		220		630	
Fibroadenoma	5	46	20	100	39	290	110.9	890	200
Infiltrating Ductal Carcinoma	25	47	20	120	43	380	126.9	1400	350
Ductal Carcinoma in Situ	1	71		190		640		2100	

Table 3. 4: Average elastic moduli and the standard deviation of the moduli (SD) for each of eight different types of breast tissue tested. SD is not reported for those tissue types for which there was only one specimen.

Tissue Type	N	Elastic Modulus Ratio to Fat at				Modulus Ratio Strain = 0.15 : Strain = 0.01
		Strain = 0.01	Strain = 0.05	Strain = 0.10	Strain = 0.15	
Gland	7	4	5	8	16	4:1
Phyllodes Tumor	1	12	14	16	17	2:1
Papilloma	2	5	8	16	31	6:1
Lobular Carcinoma	1	7	12	21	36	5:1
Fibroadenoma	5	9	15	28	51	6:1
Infiltrating Ductal Carcinoma	25	10	18	37	79	8:1
Ductal Carcinoma in Situ	1	15	29	61	124	8:1

Table 3. 5: The ratio of elastic modulus of each tissue type to fat at 4 strain levels.

3.4 Discussion

The rubber model testing shows good agreement between elastic moduli estimated from punch indentation tests and uniaxial compression tests of the same samples and validates our methodology. For a particular strain rate, there is less than 2.7% difference in modulus estimated across multiple trials and both thicknesses of samples. The average standard deviation between two measurements on the same thickness of sample is less than 1.9% and taken together these results indicate that the testing method is quite repeatable, independent of sample thickness. The slope of the best fit line between punch indentation tests and uniaxial compression tests was 1.08 ($r^2=0.99$) indicating that the relations presented here overestimate the stiffness of the material being tested but this error is less than 8%, provided that the uniaxial compression tests were perfectly accurate. It is difficult to measure the exact size of the uniaxial compression specimen and because the modulus measurement depends linearly upon it, it is a source of significant error. To quantify the error multiple measurements of the size of each sample were made; the standard deviation of these estimates was approximately 5%. This result implies that the area of the specimen could be

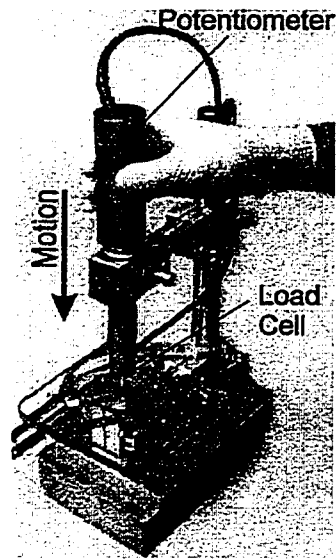
misestimated by as much as 10%. Because the punch indentation tests are not subject to this error, this could explain the discrepancy between the measurements. For this reason, we did not adjust the correlation to eliminate the error.

Figure 3.5(a) shows the variation in the stress-strain curves for indentation tests of infiltrating ductal cancer while Figure 3.5(b) shows the same curves for fat made at different indentation velocities. There is less than a 5% difference in the elastic modulus measured across all strain rates tested. These figures show that the first major conclusion of this work is that breast tissue displays a primarily elastic response with a less than 5% change in modulus estimated across test velocities (which agrees with Krouskop et al. 1998). Therefore it is a reasonable approximation to assume that breast tissue in bulk can be modeled as an elastic material whose stiffness does not depend strain rate.

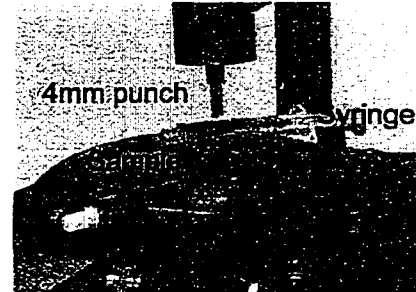
The second major conclusion of this work is that there is a significant correlation between tissue histology and stiffness. As shown in Table 3.5, infiltrating ductal carcinoma is not only much stiffer than fat and normal glandular tissue, but displays a much more non-linear increase in stiffness (it exhibits an eight-fold change in stiffness whereas glandular tissue and fat displays a four-fold increase). These figures are reflected in the model fits presented in Tables 3.3 and 3.4, where the amount of nonlinearity is reflected in the constant of the exponential and the large increase in stiffness from 0.01 strain to 0.15 strain. For normal glandular tissue and fat the exponent of the exponential fit is approximately 10, while for the cancerous tissues it is approximately twice that. Matched pair t-tests reveal that there is a significant difference between the cancer and fat ($t=7.5$, while $t_{significant} = 1.73$ at $\alpha=0.05$, for $n = 25$) and the cancer and gland at all strain levels ($t=3.52$, average, while $t_{significant} = 2.01$ at $\alpha=0.05$, for

n=7). They also reveal that there is a significant difference between the fit constants for fat and infiltrating ductal cancer ($t=7.2$ and $t=6.9$ for m^* and b^* respectively). There is also a significant difference between the fit constants for infiltrating ductal cancer and glandular tissue ($t=3.34$ and $t=3.25$ for m^* and b^* respectively). We observe that the other types of tissue also exhibit the same trend, but it is difficult to draw quantitative conclusions because of the small sample size.

We note, as did Krouskop et al.(1998), that diagnostic specificity may be gained by exploiting the difference in non-linearity between cancer and the benign breast tissues. For instance, if an image of the elastic modulus distribution throughout the breast was made at one strain level and then the strain level was doubled, all of the tissue compressed would see an increase in stiffness. However, the malignant tissues would see a greater increase, perhaps allowing them to be discriminated from the surrounding tissue with better resolution than currently available methods.



(a)



(b)

Figure 3.1: (a) The tissue testing instrument and a close-up photograph (b) showing the sample location and typical geometry.

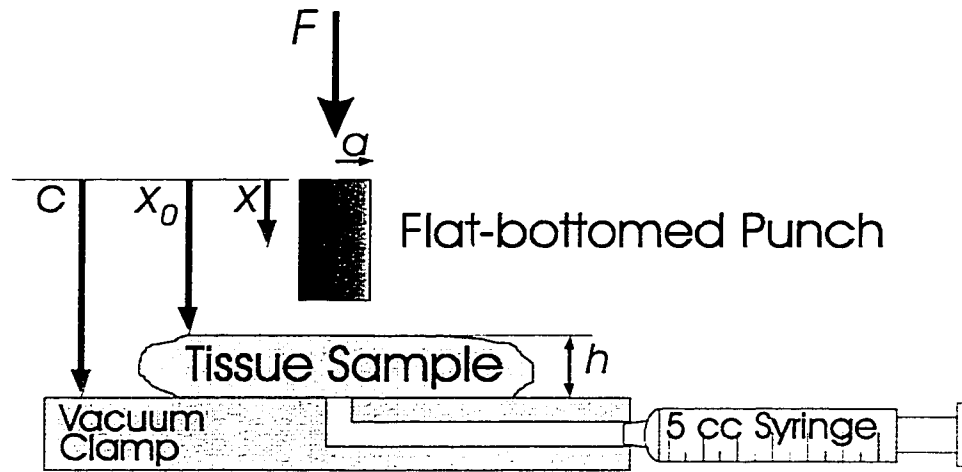


Figure 3.2: The specimen geometry during punch indentation testing.

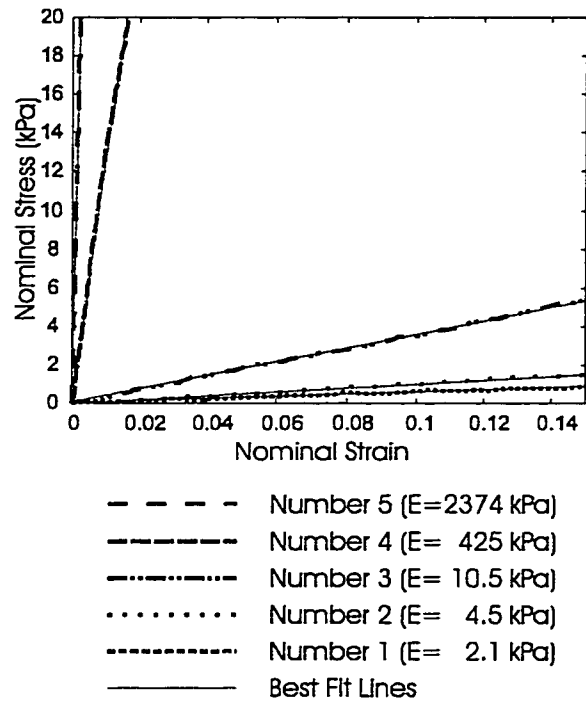


Figure 3.3: Typical nominal strain–stress curves for five silicone rubber specimens.

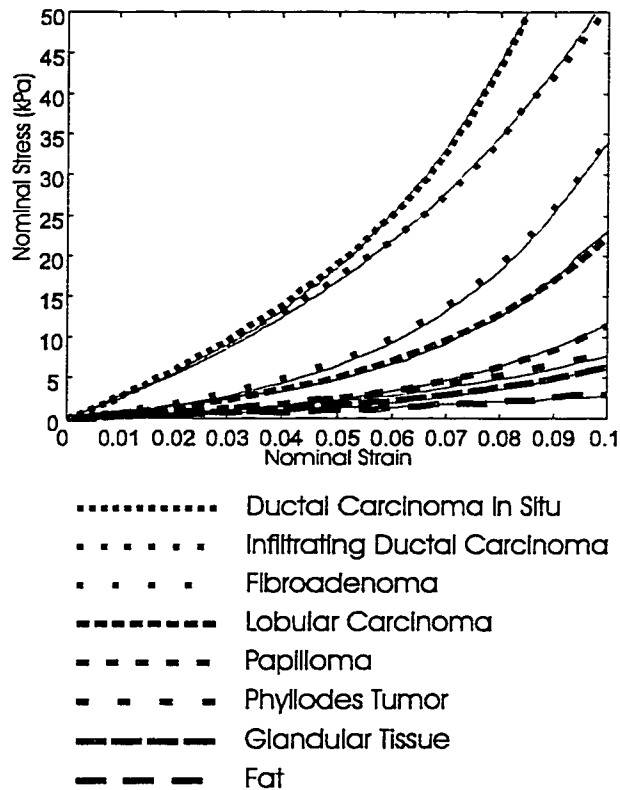


Figure 3.4: Typical strain-stress curves for 8 different kinds of breast tissue measured at approximately 500percent/second indentation strain rate.

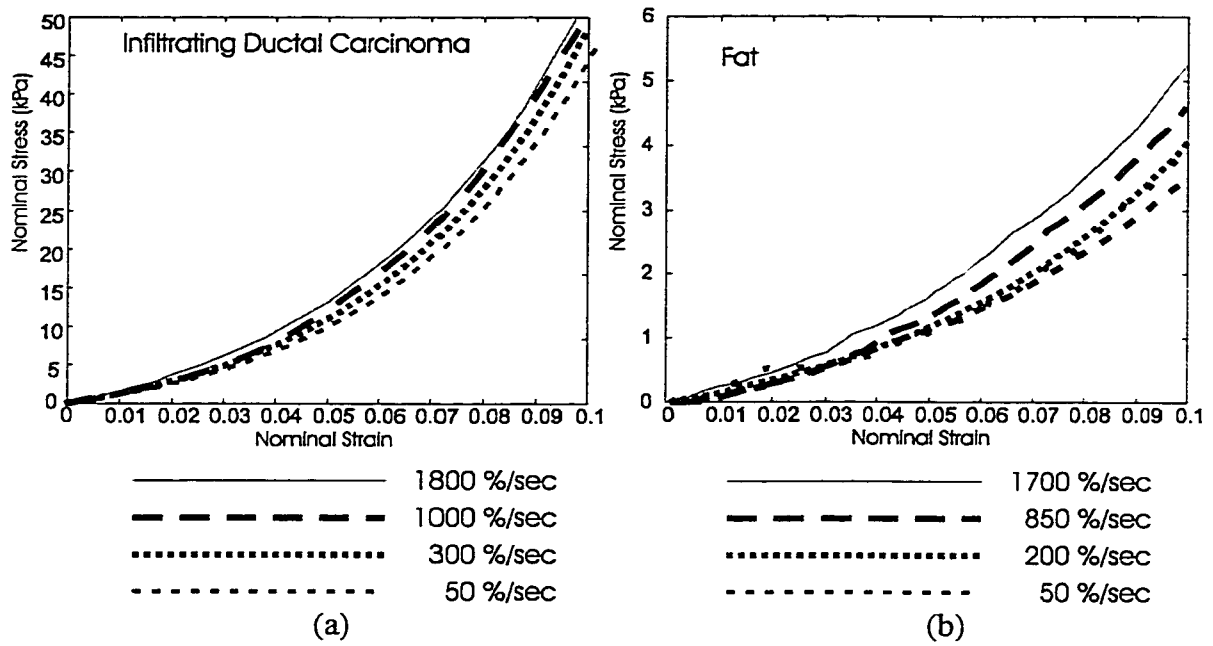


Figure 3.5: (a) Typical strain stress curves for infiltrating ductal carcinoma at four different velocities. There is less than a 5% difference in the modulus across all strains from the highest to the slowest indentation strain rates. (b) Typical strain-stress curves for fat at four different velocities. There is less than a 4.5% difference in the elastic modulus at all strain levels between the largest and the smallest strain rates.

Chapter 4

Mechanical Modeling

4.1 Introduction

In this chapter we develop algorithms that are used to extract the features of lumps that have been imaged. In order to develop these algorithms we have developed a forward model, relating lump and tissue properties to pressure distributions, and an inverse model which extracts lump properties from distributed pressure measurements. Figure 4.1 presents a block diagram of the development process. Development was separated into three major parts. The first part; data acquisition and construction of tactile maps is discussed in Chapter 2.

In the second part we require an inverse model that takes a tactile map or a sequence of pressure frames as input and produces the size and shape of the mass that has been imaged as output. In order to develop this function we first developed an understanding of the mechanics of the situation using a forward model. The model takes material and geometric properties as inputs and produces individual pressure images and

composite maps as output. Because we are looking for a tool that allows us to develop inversion methods, we minimize the complexity of the forward model as much as possible but retains enough detail that it captures the trends of the real physical situation. This model is presented in Section 4.2. We then use this forward model to develop an inverse model that relates pressure distributions to geometric and material properties as discussed in Section 4.3. Both of these models are validated using experiments on rubber models presented in the latter portion of this chapter. In Chapter 5 we discuss the evaluation of the inverse models in a limited clinical trial on surgical patients.

4.2 Forward Model

A cross section of a typical mature, pre-menopausal female breast is shown in Figure 4.2(a). The typical breast has an almost conical structure that has multiple layers. Working outward from the chest wall, the four layers are: the pectoralis major muscle, the glandular tissue layer which contain lactiferous ducts near its surface that feed into the nipple, an overlying layer of fat and finally the skin. The glandular tissue is supported by estrogen; when a women reaches menopause the estrogen levels decrease and the glandular tissue atrophies and eventually disappears completely, leaving only muscle, fat and skin (Harris et al. 1994).

The most common form of breast cancer is infiltrating ductal carcinoma. It forms in the lactiferous ducts and then grows into the surrounding tissue layers as shown in Figure 4.2(a), with characteristic tendrils of tissue that give the lump a spiculated appearance in mammograms and pathology sections and result in it being well tied to the surrounding tissue. Cancers become palpable when they protrude into the layer of fat that is above the glandular layer, or produce a lump in the glandular tissue that protrudes

into the fat and becomes palpable (Dalton 1998, Kern 1998, Krag 1998). In the case of post-menopausal women, cancer usually forms in the ducts and as the normal glandular tissue disappears, the cancer remains, leaving it completely embedded in a layer of fat.

Other normal breast structures that can feel like cancer can be found in the breast. These are typically irregularly shaped lumps of normal glandular tissue that can be quite hard. These masses are prevalent in peri-menopausal women because the glandular tissue does not disappear uniformly and can leave islands of isolated glandular tissue that can cause difficulty in interpreting physical examinations (Dalton, Kern, Krag 1998). Depending on how well attached to the surrounding tissue these lumps are, they can be quite mobile as they slide through the tissue planes. The location of these palpable lumps within the tissue layers allows us to make a number of reasonable simplifying assumptions.

4.2.1 Forward Model Derivation

We assume that all lumps are found at the interface of the glandular tissue and the fat and protrude up into the fat layer from the glandular tissue. We also observe that the tissue is of relatively uniform thickness in the neighborhood of the lump, particularly in the upper outer quadrant and axilla of the breast which are shown in Figure 4.2(b), where the majority of cancer is found (Harris et al. 1994). Therefore, we assume that the breast can be modeled as three layers of uniformly thick tissue: the chest wall which incorporates the muscle, a layer of normal glandular tissue, and a layer of fat. We have ignored the effect of the skin because it is thin compared to the other tissues and is extremely flexible. In the clinic the effect of the skin can be minimized by placing the patient so the skin is not tensioned. We model the lump as a single round nodule that occurs at the

boundary of the normal glandular tissue and the fat. Most biological tissue is nearly incompressible (Fung 1991) and we make this assumption for each of tissue layers in the model. We idealize the behavior of fat as nearly linearly elastic and isotropic because our measurements (see Chapter 3) have shown that fat does not undergo much change in modulus with strain. We also take the normal glandular tissue and the tumor to linearly elastic and isotropic and will explore the effect of their nonlinear elastic modulus by varying the stiffness ratio of the tumor to the surrounding fat. The chest wall and the indenter are taken to be rigid. We assume that the normal glandular tissue stiffness is fixed at 10 times the stiffness of the fat (based on our measurements of normal glandular tissue in Chapter 3) and that it is 1cm thick in all models. The fat stiffness, E_1 , is set to 5.5kPa, to approximate the average stiffness of breast tissue in the patients tested at the 5% strain level (see Table 3.4). The radius of the indenter, R , is 1.9 cm, which is the device radius of curvature.

Even with these simplifying assumptions, we still must solve a three-dimensional, inhomogeneous, multi-layered contact problem. While there is extensive literature on contact mechanics, beginning with Hertz' classic solution of the contact of two elastic bodies (Johnson 1985), this model does not include consideration of inclusions beneath the surface. There have also been models of elastic inclusions in elastic media. Goodier has computed a model of a spherical inclusion in an infinite media (Goodier 1936) while Eshelby has extended this model to include transformation strains of an ellipsoidal region in an infinite elastic media with constant stresses at infinity (Eshelby 1957). Neither of these models accounts for the contact of two different media. More recently, other researchers have treated the problem of two bonded semi-infinite half spaces with

different elastic moduli where one contains an inclusion (Yu and Sanday 1991). Unfortunately this model does not relate contact mechanics to measured stress distributions. There has even been some work done relating measured stresses of contact to object shape but this work does not examine the effect of a thick intervening layer of tissue (Fearing and Hollerbach 1985). Since no analytical solution for the problem exists, we have developed a solution using the finite element method.

To make the problem more tractable, we have made one more simplifying assumption: that the breast can be modeled with a two dimensional plane strain model, as shown in Figure 4.3. A two dimensional model makes a reasonable approximation to the pressure along the center line of the real indenter, shown in Figure 2.1a, because the indenter is relatively long compared to its width. Since we are developing a model which will enable us to develop inversion algorithms, and thus must capture the trends but not necessarily the exact magnitudes of the real case, a two dimensional model should suffice. This assumption will be tested experimentally, as discussed later in the chapter. Finally, as a first approximation, we assume that all lumps are circular in the plane and therefore are circular cylinders in three dimensions.

4.2.2 Finite Element Model

The geometry shown in Figure 4.3 was meshed for use as a finite element model and pilot studies were used to determine the mesh size and geometric parameters for the model. The mesh was chosen so that the elements at the contact surface were square with a side length of 0.2 cm. Finite element pilot studies were performed that showed that reducing this length resulted in less than a 1.5% mean squared difference, MSD, in the pressure distribution at any point on the surface. The half width of the model, w_m , was

chosen to be 4 indenter widths (4.8 cm) as further finite element analysis pilot studies revealed that increasing the width resulted in less than a 1% MSD in the pressure distribution. Finally, we assume that the thickness of the normal glandular tissue, c , is 1 cm. To determine the effect of changes in this parameter on the output pressure distributions, we varied the glandular tissue thickness between 0.5cm and 2 cm while holding the thickness of the fat, t , at 0.55 cm.

The fat thickness was set at 0.55 cm because this is the minimum thickness that would be encountered with a 0.5 cm diameter lump buried 0.6 diameters deep, and is the limit of the range of parameters. This case should show the most pronounced effects of varying the glandular tissue thickness because it provides the least intervening tissue. The output pressure distributions varied by less than 3%, MSD, for across this range. Larger lumps would have greater fat thickness and the effect of changes in the thickness of the glandular tissue would be even less. The two remaining geometric parameters in Figure 4.3 are h , the depth of the lump, and d , the diameter of the lump and were variables in the study. The variable h was set at the values 0.5 cm, 1.0 cm, 1.5 cm, 2.0 cm and 2.5 cm while h was set to $0.6d$, $0.8d$, $1.0d$, $1.2d$, $1.5d$ and $1.8d$ in order to span the range of typically encountered lumps. We normalize to the lump diameter because it is a fundamental length scale in the model and will facilitate comparison. The geometric parameter t is the thickness of the fat and is $t = h + d/2$. Finally, the elastic modulus of the tumor, E_2 , was set to 2, 5, 8, 10 and 100 times the elastic modulus of the fat, E_1 .

Figure 4.4 shows an illustrative sample result from the finite element modeling. Figure 4.4(a) shows the pressure distribution on the face of the indenter when it is centered over the lump, and appears to be Gaussian, with some offset. Figures 4.4(b)

through 4.4(d) show the pressure on the face of the indenter as it slides off of the lump. The pressure distribution far from the lump is nearly flat, while the others appear as though they could be a weighted sum of the pressure distributions in Figure 4.4(a) and Figure 4.4(c). This is an important observation because even though finite element models can give results for specific cases, it is still only a discrete representation of the pressures. It would be useful to have an analytical expression that predicts the pressure at any point on the surface of the indenter as a function of geometric and material properties. This function will be useful to determine the distributions for cases not evaluated with the finite element models and will also be useful in exploring inversion algorithms and invertibility issues as well as exploring the effects of the different parameters on the output pressure distributions.

4.2.3 Empirical Model

We have developed a model that is a curve fit to the finite element results and is motivated by our observations of Figure 4.4. It is also loosely motivated by the principle of superposition that suggests the pressure distribution on the face of the indenter for each location of the indenter along the surface of the tissue can be represented as the weighted sum of two pressure distributions shown in Figure 4.5. The first, P_1 , is the pressure distribution across the face of the indenter that would be produced with no lump (and corresponds to the pressure distribution shown in Figure 4.4(d)). The second, P_2 , is the difference between P_1 and the pressure distribution that is measured on the face of the indenter when it is centered over the lump, P_0 (which corresponds the pressure distribution in Figure 4.4(a)). Each of these pressure distributions is shown in Figure 4.5, where $P_2 = P_0 - \alpha P_1$ and $\alpha = 0.5$ is an arbitrary parameter chosen to be sure that $P_2 > 0$.

The analysis presented in Chapter 2 reveals that the exact shape of the head required to produce a uniform pressure distribution varies with the indentation force, F , and the thickness of the tissue being indented, t . Because the shape of the head is fixed, and not all tissue is infinitely thick as presumed by the model, there will be some deviation from a perfectly flat distribution that must be examined using the finite element models. Figure 4.6 shows the pressure distributions calculated from the finite element models with no lump. Twelve different cases are shown; in Figure 4.6(a) the thickness of the tissue, t , is varied from 1 cm to 6 cm, while in Figure 4.6(b) the indentation force is varied from 0.8 N/cm to 1.6 N/cm. These curves reveal that P_I depends on both the thickness of the tissue being indented and the indentation force applied. All curves have been normalized by the integral of the pressure. After normalization there is less than a 4% mean squared difference between curves at different total indentation force levels. Because the thickness of the tissue in the real case is close to a constant in the neighborhood of the lump, and because its effect is so small, we choose to ignore this variation. However, we do not ignore the variation in the distribution that is caused by input variations because the force level can change considerably as the head is stroked across the breast during a real examination and we need to see how this force variation affects the maps. To capture this variation we parameterize P_I using a Hertz like pressure distribution (Johnson 1987) as a function only of location on the face of the sensor, s , and the thickness of the tissue, t from,

$$P_I(s,t) = \begin{cases} P_o(t) \cdot \left(1 - \left(\frac{s}{a(t)}\right)^2\right)^{\frac{1}{2}} & -w \leq s \leq w \\ 0 & otherwise \end{cases} \quad (4-1)$$

where $2w$ is the width of the head (1.2 cm), $P_o(t)$ and $a(t)$ are found by linear interpolation in Table 4.1 and were determined by fitting the curves in Figure 4.6(a) with Equation 4-1.

t (cm)	0.5	1	1.5	2	3	4	5	6	10
a (cm)	1.21	1.27	1.43	1.65	1.65	1.65	1.65	1.65	1.65
P_o (kPa/cm)	0.541	0.516	0.487	0.467	0.466	0.462	0.457	0.513	0.451

Table 4.1: The constants a and P_o for the Hertz like fit as a function of tissue thickness.

In Figure 4.4 we saw that P_2 looks very much like a Gaussian distribution and thus we parameterize it as one. We model the pressure distribution as a function of location along the surface of the tissue, x , lump diameter, d , stiffness ratio of tumor to surrounding fat E_2/E_1 , and depth ratio from the surface of the tissue to the center of the lump, h/d , as,

$$P_2(x, d, E_2/E_1, h/d) = g(d, E_2/E_1, h/d) \cdot e^{-\left(\frac{x^2}{2\sigma^2(d, E_2/E_1, h/d)}\right)} \quad (4-2)$$

where $g(d, E_2/E_1, h/d)$ is found by interpolating on the values in Appendix C, Tables C.1 – C.5, and $\sigma(d, E_2/E_1, h/d)$ is found by interpolating on the values in Tables C.6 – C.10 which were found by fitting the pressure distributions calculated by the finite element models with Equation 4-2. We will show later in this chapter that this is a good approximation.

Once both pressure distributions are determined, we define an empirical fit function which models the pressure in an individual tactile image or pressure frame, P_f , at any point on the indenter surface for any location of the indenter with respect to the center of the tumor

$$P_f(x, x_c, d, E_2/E_1, h/d) = \begin{cases} P_2(x, d, E_2/E_1, h/d) \cdot \left(\frac{P_1(x-x_c, t)}{P_0} \right)^2 + \kappa(x_c, d) \cdot P_1(x-x_c, t) & -w \leq (x-x_c) \leq w \\ 0 & \text{otherwise} \end{cases} \quad (4-3)$$

where x_c is the location of the center of the indenter with respect to the center of the tumor, and P_f becomes P_0 when $x_c = 0$. The $\frac{P_1(x-x_c, t)^2}{P_0}$ takes on values between 0 and 1 and is motivated by the roll-off in peak amplitude of the pressure distribution that is seen in Figure 4.4(b) and 4.4(c). It ensures the empirical pressure distributions fit the finite element model derived distributions accurately. The quantity $x-x_c$ is the location on the scan head reference to the center of the head and is restricted to $-1.2 \leq x-x_c \leq 1.2$, and the factor $\kappa(x_c, d)$ is a weighting constant and is defined from

$$\kappa(x_c, d) = \begin{cases} 0.5 \cdot \left(1 + \frac{8}{3d} |x_c| \right) & 0 \leq |x_c| \leq \frac{8}{3}d \\ 1 & \text{otherwise} \end{cases} \quad (4-4)$$

where the constants in the expression were empirically determined to ensure a good fit to the finite element and rubber model test data which is presented below.

Using Equation 3, it is possible to assemble a two dimensional tactile map which is the average of all of the pressure values passing over the tissue surface as the indenter slides across it.

$$P_{map}(x, x_c, d, h/d, E_2/E_1) = \frac{\sum_{x_c=-5}^{x_c=5} \sum_{(x-x_c)=-1.2}^{(x-x_c)=1.2} P_f(x, x_c, d, E_2/E_1, h/d)}{\sum_{x_c=-5}^{x_c=5} \sum_{(x-x_c)=-1.2}^{(x-x_c)=1.2} q(x, x_c)} \quad (4-5)$$

where x and x_c are spaced in 0.05 cm increments (which is 1/3 of the distance between elements on the pressure sensor, and accounts for the sub-sampling of the array as discussed in Chapter 2) and q sums up the non zero locations from

$$q(x, x_c) = \begin{cases} 1 & -w \leq (x - x_c) \leq w \\ 0 & \text{otherwise} \end{cases} \quad (4-6)$$

Equation (4-5) presents the map as the average of all of the data from all of the individual pressure frames P_f that pass over a particular location, as shown in Figure 4.8(a). Since P_f is defined as a continuous function of x , and x_c , we can actually write Equation 4-5 in an integral form. The crucial step to writing this integral is to recognize that the map can also be thought of as the average of all of the pressure curves produced by each point on the surface of the indenter as it slides across the surface as shown in Figure 4.8(b). This motivates a change of variables, $s = x - x_c$, to get a set of curves

$$P_{surface}(x, s, d, E_2 / E_1, h / d) = P_2(x, d, E_2 / E_1, h / d) \cdot \left(\frac{P_1(s, t)}{\max(P_1(s, t))} \right)^2 + \kappa(x_c, d) \cdot P_1(s, t) \quad (4-7)$$

that are a function of the point on the indenter surface, s , the actual location on the map surface, x and the geometric and material properties while κ is defined in Equation 4-4. Equation 4-7 allows us to write the equation for the map as the average of all of the curves produced by all of the locations on the surface of the indenter as

$$P_{map}(x, x_c, d, h / d, E_2 / E_1) = \frac{1}{2w} \int_{-w}^w P_{surface}(x, x_c, d, h / d, E_2 / E_1) ds \quad (4-8)$$

where $2w$ is the width of the sensor mounted on the indenter (in our case 1.2 cm). Substituting equations (7), (4) and (1) into (8) and performing the integration yields

$$P_{map}(x, x_c, d, h/d, E_2/E_1) = P_2(x, d, E_2/E_1, h/d) \cdot \left(1 - \frac{w^2}{3a^2}\right) + C \quad (4-9)$$

and

$$C = \frac{P_o}{w} \cdot \left(-A\sqrt{1-A^2} + \frac{w}{a} \sqrt{1-\frac{w^2}{a^2}} - \sin^{-1}(A) + \sin^{-1}\left(\frac{w}{a}\right) \right) + \frac{1}{2w} \left(A\sqrt{1-A^2} + \sin^{-1}(A) \right) \quad (4-10)$$

where $A \equiv \frac{3d}{8a}$. This is just a constant that depends only on the geometric parameters.

Since P_2 is a Gaussian distribution, Equation 4-9 shows that the map will also have a Gaussian form, with the same standard deviation as P_2 but different amplitude.

4.2.4 Forward Model Validation

To be sure that the empirical model predictions accurately reflect the finite element results, they were compared on a frame-by-frame basis. Figure 4.8 shows a representative set of frame by frame pressure curves for four lumps. The tests spanned a range of lump sizes from 0.5 cm to 2.5 cm in diameter, and depth ratios, h/d , from 0.6 to 1.8 diameters. Table 4.2 summarizes the mean squared error figures for ten cases. The average mean squared difference for these frames is less than 4.2%, while averaging across all frames in a sliding motion it is 4.3%, averaged across all cases. The finite element and empirical models were also compared on the map level, and Table 4.3 summarizes the results. Mean squared difference is less than 2.5% average.

For experimental verification, we constructed a set of breast models from a uniform layer of silicone rubber (modulus 5.5kPa), containing rigid plastic spheres mounted on a hard backing to simulate tumors. Because the real indenter is three-

dimensional and the models only have two dimensions, it is unknown at what force level to press the indenter into the rubber models. The force was set so that the average indentation pressure on the indenter was 3.4 kPa – determined so that the peak of the tactile map containing the 1.25cm diameter lump would be the same as the peak of the finite element derived map. This level was then kept constant for the remainder of the trials. The maps were made using the preferred clinical technique: many strokes made in a single direction.

The centerline values of the maps for four test cases are shown in Figure 4.9. There is a less than a 4% maximum difference in the maps, with average MSD = 2.1%. Table 4.4 summarizes the results for all maps tested. The individual pressure frames as the indenter slides across the surface were also recorded and compared along the centerline of the sensor with the two dimensional map frames P_f , from the empirical model. These frames are shown for two representative lumps in Figure 4.10. There is an average mean squared difference of less than 15%, with no more than 35% mean squared difference maximum between the model derived frames and the measured frames and is because of the extremely noisy measured frame signals.

h/d	d (cm) 0.5	1.0	1.5	2.0	2.5
0.6	4.1%	4.3%	4.1%	4.1%	4.2%
1.8	4.1%	4.2%	4.2%	4.0%	4.1%

Table 4.2: Mean squared difference between the empirical model and the finite element models for the frame centered directly over the lump for 10 sample cases.

h/d	d (cm) 0.5	1.0	1.5	2.0	2.5
0.6	2.4%	2.7%	2.5%	2.3%	2.2%
1.8	2.3%	2.5%	2.4%	2.5%	2.6%

Table 4.3: Mean squared difference between the empirical model and the finite element models for the maps generated for 10 sample cases.

Lump Diameter (cm)	Lump Depth to Center (Diameters)	Mean Squared Difference Between Maps	Maximum Mean Squared Difference Between Frames	Average Mean Squared Difference Between Frames
1.25	0.825	1.1%	23%	8%
1.55	1.0	2.0%	24%	13%
1.55	1.4	3.9%	35%	21%
1.875	1.2	1.5%	31%	12%

Table 4.4: Comparison of the empirical model derived maps and frames and the tests conducted in rubber models for four cases.

4.2.5 Forward Model Trends

Using this model, we have determined trends to allow us to develop signal processing algorithms to extract the features of the lump. Since the output pressure distributions depend on three primary parameters: depth, lump size and lump stiffness to background ratio, we have investigated these first. We will show that this is an ill-posed inverse problem: there are some combinations of size, depth and hardness lead to the same map pressure distributions and the same individual pressure frame distributions.

Figure 4.11 makes it clear that there are many combinations of size, depth and stiffness that will produce the same map pressure distribution, and also the same pressure distributions on the face of the indenter. In Figure 4.11(a) we see three map curves that have been normalized to the pressure far from the lump and which are nearly identical (mean squared difference less than 0.5%, maximum). These curves are presented for lumps with diameter of 25 mm, 15 mm and 5 mm and depths of 0.6, 0.73 and 1.02 diameters respectively. The stiffness ratio was set at 100 for all. Figure 4.11(b) shows the pressure distribution on the face of the indenter when it is centered over the lump and indented to a total force per unit length of 0.1N/cm for the same three masses. These too

are identical. Therefore the problem is not strictly invertible, since it is not possible to uniquely determine the set of size, depth and stiffness parameters that produces a given pressure distribution.

Since the pressure distributions in Figure 4.11(a) appear to be Gaussian and since we have shown in Equation 4-9 that if the individual frames are modeled as Gaussian, we can model the map pressure distribution as Gaussian. We model the map as

$$P_{map}(x, d, E_2 / E_1, h / d) = a(d, E_2 / E_1, h / d) \cdot e^{-\left(\frac{x^2}{2\sigma^2(d, E_2 / E_1, h / d)}\right)} + 1. \quad (4-11)$$

Figures 4.12 (a) and 4.12(b) show two representative finite element map pressure distributions and the Gaussian fit to them, with mean squared error less than 0.1%.

Figures 4.13(a), 13(b) and 13(c) show the variation in map width that results from variations in stiffness. The maps have been normalized to the peak pressure to make them easier to compare. Figure 4.14 shows the variation in the standard deviation of a Gaussian fit to these curves, and reveals a less than 5% variation in this parameter for stiffness ratios exceeding 8. And, since most lumps are at least this much stiffer than the surrounding fat (see Chapter 3) we assume that stiffness is not an important parameter to consider when estimating the size of a lump.

4.3 Inverse Modeling

4.3.1 Invertibility

Given the result in Figure 4.14, we assume that all lumps are 100 times as stiff as the surrounding tissue. We can restrict the range of depths to 0.6 to 1.8 diameters (which is a physiologically reasonable range), and fit the output pressure distributions calculated

from the finite element models to determine the shape of the surface that the two fit parameters a and σ fall upon. Figure 4.15 (a) shows the surface for the fit parameter a , while Figure 4.15 (b) shows the surface for the parameter σ as functions of h and h/d . This figure makes it clear that within this range the function is monotonic and increasing – which implies that it may be invertible. To check for invertibility, we note that we can write an equation for the surface in Figure 4.15(a) as

$$\sigma(d, h/d) = 0 \tag{4-12}$$

and for the surface in Figure 4.15(b) as

$$a(d, h/d) = 0. \tag{4-13}$$

To see if the functions are invertible, we can write the Jacobian (Hildebrand, 1976)

$$J \equiv \frac{\partial(\sigma, a)}{\partial(d, h/d)} \equiv \begin{bmatrix} \frac{\partial \sigma}{\partial d} & \frac{\partial \sigma}{\partial(h/d)} \\ \frac{\partial a}{\partial d} & \frac{\partial a}{\partial(h/d)} \end{bmatrix}. \tag{4-14}$$

According to the inverse function theorem these functions are uniquely invertible if,

$$\det(J) \neq 0. \tag{4-15}$$

Of course, this theorem assumes that there is no noise in the measurements. This is not the case. However, since it is difficult to determine an accurate model for the noise, we will evaluate its effect on the inversion experimentally.

4.3.2 Inverse Model: Gaussian Fit Algorithm

Figure 4.16 makes it clear that the inverse exists nearly everywhere in the space of interest, except for the few cases near the edges of the space (large shallow lumps, or small deep lumps, as shown in Figure 4.11). Since we now know that the functions are invertible for this range of parameters, the task is reduced to finding the pair of h and h/d that produce the pair of a and σ , in the absence of noise. The presence of noise in the signals would tend to make the space of non-invertible parameters larger. Because it is difficult to parameterize the noise accurately, we will assess the effect of noise in the maps on invertibility experimentally as discussed later. This could be accomplished through any number of means, including simply finding a polynomial parameterization for the surfaces in Equations (4-12) and (4-13) and then finding the roots of the polynomial. Alternatively, one could use a root guessing method on the original surfaces to find the pair of h and h/d that produce the given a and σ . However, the surfaces presented here based on the finite element models are unlikely to be exactly the same as the real surfaces. These could be refined as the device is used on more and more patients. Practically speaking, this is difficult to accomplish since it is difficult to know the geometry and material properties of the real cases exactly. It would also require a large amount of data to achieve a sufficiently accurate surface. As an alternative we will develop an approach that can be more easily adapted to the real physical situation.

We would like to extract the size of the lump from the pressure distributions and because we recognize that the width of the pressure distribution varies with the depth of the lump we need a way to find the depth of the lump. In Figure 4.17(a) we see that it is possible to find the depth of the top of the lump, $h_t = h-d/2$, exclusively as a function of

the peak normalized pressure a_p . The peak pressure can be found from the Gaussian fit proposed in Equation 4-11 and is

$$a_p = a + 1. \quad (4-16)$$

We see that the data in Figure 4.17(a) can be fit quite well (mean squared error, MSE < 3%) with an allotropic relationship,

$$h_t = f \cdot a_p^g. \quad (4-17)$$

The fit constants f and g are real numbers and can be found by taking the natural logarithm of both sides and finding the slope and intercept through linear regression. They are $f=1.8$ and $g=-3.21$ for the FEA and empirical models. We are interested in the depth of the lump primarily because it affects the apparent size of the lump at the surface. Because the overlying tissue produces spatial filtering which tends to broaden and lower the map pressure distributions, we must account for this change. We could use Equation 4-17 to find the depth of the lump and relate this depth to the change in width but we observe that Figure 4.17(b) shows that the change in width is directly related to peak pressure. Therefore we seek a function that relates the change in width of the pressure distribution, as represented by $\Delta\sigma$ which is the percent change in size of a lump, referenced to its size at 1.0 diameters in depth. The data in Figure 4.17(b) make it clear that an allotropic relationship produces a good fit (less than 5.25% mean squared difference),

$$\frac{\sigma_{fit}}{\sigma_{h/d=1}} = h \cdot a_p^n \quad (4-18)$$

where σ_{fit} is the standard deviation of the Gaussian fit to the data, $\sigma_{h/d=1}$ is the standard deviation of the Gaussian that would have been measured if the lump were one diameter deep and $h = 5.03$ and $n = -4.02$ for the FEA and empirical models calculated through regression. There is also a linear relationship between the standard deviation of the distribution and the lump diameter at one diameter depth which is shown in Figure 4.18.

Together, these observations suggest that a possible inversion algorithm is to fit a distribution like the one in Equation 4-11, and then use these fit parameters to estimate the size of the lump. Equation 4-18 allows us to find the width of the distribution at one diameter in depth from

$$\sigma_{h/d=1} = \frac{\sigma_{fit}}{h \cdot a_p^n}. \quad (4-19)$$

We can use these curves to find the depth of the lump and the width of the distribution at 1.0 diameters deep. The diameter of the lump that produced the distribution can then be found from a line fit to the data in Figure 4.19 ($r^2=0.99$) which is

$$d = 7.59\sigma_{h/d=1} - 1.36. \quad (4-20)$$

Note that Equation 4-19 can be written in the form $a(d, h/d) = 0$, while Equation 4-20 can be written in the form $\sigma(d, h/d) = 0$. These are exactly the equations that we checked for invertibility using the Jacobian, and therefore this pair has the same invertibility as discussed before. This algorithm can be generalized to the full tactile map created with the tactile imaging system by fitting

$$P_{map}(x, y) = a \cdot e^{-\left(\frac{x^2}{2\sigma_x^2} + \frac{y^2}{2\sigma_y^2}\right)} + 1 \quad (4-21)$$

using a simplex search algorithm. We assume that the two diameters, d_x and d_y , of an ellipsoidal model of the lump are related to the σ_x and σ_y by Equations 4-19 and 4-20.

4.3.3 Inverse Model: Thresholding Algorithm

Because fitting a Gaussian to the map can be computationally expensive, we also developed a second algorithm that simply thresholds the map at a particular level and then estimates the lump size. First, we threshold the map to get

$$P_{threshold} = \alpha * (P_{max} - P_{mean}) + P_{mean} \quad (4-22)$$

where P_{max} is the maximum pressure in the map and P_{mean} is the mean pressure in the map. The arbitrary parameter $\alpha=0.3$ was chosen by trial and error to ensure that the average diameter of the 15.5 mm diameter, 15.5 mm deep lump tested in laboratory trials described below was accurate to within 1 mm for two of the examiners. Pressures in the map above this value were set to 1, while those below were set to 0. The maximum and minimum diameters of the lumps were computed by finding the moments of the thresholded image from

$$I_{xx} = \iint P(x, y) \cdot y^2 \cdot dA \quad (4-23)$$

$$I_{yy} = \iint P(x, y) \cdot x^2 \cdot dA \quad (4-24)$$

$$I_{xy} = \iint P(x, y) \cdot xy \cdot dA \quad (4-25)$$

where $P(x,y)$ is the value in the thresholded image (either 1 or 0) and x and y are the distance of that value from the center of the image. We then formed the moment matrix

$$I = \begin{bmatrix} I_{xx} & I_{xy} \\ I_{xy} & I_{yy} \end{bmatrix} \quad (4-26)$$

and found its eigenvalues to obtain the principal moments, I_1 and I_2 . The maximum and minimum diameters of the lump are

$$d_{\max} = 2 \cdot \left(\frac{4I_1}{\pi} \right)^{\frac{1}{4}} \quad (4-27)$$

$$d_{\min} = 2 \cdot \left(\frac{4I_2}{\pi} \right)^{\frac{1}{4}}. \quad (4-28)$$

4.4 Laboratory Validation of Inversion Algorithms

In order to understand how the repeatability of the tactile imaging technique varies between examiners and to determine the appropriate threshold level for making tumor size estimates in the tactile maps, experimental trials were conducted on rubber bench models of the breast. These models were made of a uniform layer of silicone rubber that has an elastic modulus of approximately 5 kPa (similar to fatty breast tissue). Four acrylic spheres that simulated cancers (12.5 mm, two 15.5 mm and 22.0 mm) were mounted to the rigid backing of the models and covered to different depths in the silicone rubber. The 12.5 mm lump was 11.3 mm deep, the 15.5mm lumps were 15.5 and 23.3 mm deep and the 22.0 mm lump was 27.5mm deep. All depths are reported from the surface of the model to the center of the lump. The lump sizes were chosen to span the typical range of sizes that would be encountered in a clinical setting. In addition, the 15.5 mm lump was placed at two depths in order to determine if the size estimates show any significant variation with the depth of the lump.

Five different examiners used the imaging device to make two kinds of tactile maps of the lumps using two different stroking techniques. The first kind of map was made from ten strokes in a single direction and each examiner completed three trials. The second kind of map used multiple strokes from many different directions and subjects were instructed to continue to map the lump until its visual appearance in the map no longer changed. Each examiner made three different maps of this second kind. Two techniques were evaluated to determine if stroking technique produces any systematic variation in the estimated parameters.

4.4.1 Laboratory Validation: Gaussian Fit Algorithm

To validate the algorithm presented in Equations 19, 20, 21, and 22, the size of the lumps imaged in the laboratory experiment describe above were estimated using this algorithm. Figure 4.19(a) shows a tactile map of one of the test lumps ($d=12.5\text{mm}$, $h/d=0.825$) while Figure 4.19(b) shows the two-dimensional Gaussian fit of Equation 22 to it. There is less than a 2.8% mean squared difference between the two maps. The test results are summarized in Figure 4.20(a) and Table 4.5 and show that mean absolute error for the four models tested is less than 4%. The correlation between the size estimates and the true size is nearly one (slope = 0.99, $r^2=0.91$), indicating that the technique accurately determines the size of lumps, across the range tested. Two different depths of the 15.5mm diameter lump were tested and the estimated size was about 5% different. The variation across size estimates made using different mapping techniques is about 6% or about 0.8mm average for these two lumps across all subjects. Given the small number of samples there is no statistically significant difference between the size estimates from the two measurements.

Lump Depth (mm)	Lump Diameter (mm)	Estimated Diameter (mm)	Difference	Size Variation Between Mapping Techniques (Average of all subjects 1 standard deviation, mm)	Size Variation Between Subjects (Average of both techniques 1 standard deviation, mm)
11.3	12.5	13.2	5.3%	1.2	0.5
23.3	15.5	15.2	-1.7%	0.8	0.4
15.5	15.5	15.9	2.7%	0.5	0.4
27.5	22.0	21.0	-4.5%	0.9	0.6

Table 4.5: Summary of the rubber model tests of the Gaussian inversion algorithm.

4.4.2 Laboratory Validation: Thresholding Algorithm

Lump size estimates were made from the maps made in the laboratory experiment discussed above using the thresholding algorithm. Figure 4.20 (b) shows the ball size estimated from tactile maps versus the actual ball size for all subjects. Sizes are averaged for each subject and for each ball between the single direction mapping trials and the multiple direction mapping trials. The slope of the best-fit line that passes through zero is 0.96, with $r^2 = 0.89$. Table 4.6 summarizes the variations in predicted ball size depending on mapping technique and user variability. For a particular simulated lump there is less than a 2.5% difference between the maps created using the single direction stroking technique and the maps using stroking from many directions. The mean error is -1.1% across the range of models tested. The mean absolute error for this group of lumps was 7.1%. The size of the largest ball was underestimated by 12.1% and the smallest was overestimated by 4.1%. Two different 15.5 mm lumps are shown in the figure, one at 15.5 mm deep and one at 23.3 mm deep. The 15.5mm deep lump was estimated at 14.9 mm in diameter in the tactile images while the 23.3 mm deep lump was estimated at 16.7

mm in diameter. The variation in the size estimates across all subjects was 0.5mm (1 standard deviation) for these two lumps.

Table 4.7 presents size estimates averaged for all examiners for the maps made in a single stroking direction. The estimates are made with the direction of stroking (which represents the case presented in the models) and across the direction of stroking (to see if there are any differences). The average difference between these estimates across all test cases is 7.1%. Matched pair t-tests were conducted on each model tested (with pairings of across the stroke size and with the stroke size) to see if there was a significant difference between them and these results are also summarized in the table. There should be no difference between them since the lumps are spherical: any difference is an artifact of the imaging or inversion process.

Lump Depth (mm)	Lump Diameter (mm)	Estimated Diameter (mm)	Difference	Size Variation Between Mapping Techniques (Average of all subjects 1 standard deviation, mm)	Size Variation Between Subjects (Average of both techniques 1 standard deviation, mm)
11.3	12.5	13.0	4.2%	0.9	1.0
23.3	15.5	16.7	7.8%	0.5	0.5
15.5	15.5	14.9	-4.1%	0.6	0.6
27.5	22.0	19.3	-12.4%	0.9	0.9

Table 4.6: Summary of the rubber model tests of the threshold inversion algorithm.

Lump Depth (mm)	Lump Diameter (mm)	Estimated Diameter Along Stroke Direction	Estimated Diameter Across Stroke	Standard Deviation	P value (matched pair t-test with n=9)
11.3	12.5	13.3	12.3	4.9%	<0.005
23.3	15.5	17.1	16.4	2.6%	<0.005
15.5	15.5	16.5	15.4	3.3%	<0.005
27.5	22	20.4	18.4	4.9%	<0.005

Table 4.7: Size estimates across the direction of stroking and with the direction of stroking using the thresholding algorithm, averaged for all subjects.

4.5 Discussion

One purpose of this chapter has been to develop a forward model that relates geometric and material properties of the breast to output pressure distributions across the face of the indenter and at the map level. We have presented two models; a finite element model and an empirical model that fits the finite element model with less than 4.5% difference in individual pressure frames and less than 2.5% difference on the map level. For practical purposes they can be considered to yield equivalent results. These models were compared on the pressure image by pressure image level to rubber model tests of four different simulated breast lumps and had mean squared difference, MSD, of about 28% maximum and 13% average. These differences are due to the noise present in the image by image measurements. When the tactile maps are compared along the centerline of the map to the model derived maps the maximum MSD drops to about 4% across the four test cases, with mean difference less than 2.1%.

Because the forward models do a good job of predicting the trends present in the rubber models we can use them to develop inversion algorithms with some confidence of success. We have developed two algorithms; a thresholding based algorithm and a Gaussian fit algorithm. The thresholding algorithm demonstrates about 7% mean absolute error across all models and examiners tested, while the model-based algorithm demonstrates approximately 4% MAE. Given the roughly 5% average standard deviation of these measurement, there is no statistically significant difference between the two errors ($p \geq 0.085$). Given their rough equivalence in rubber models, further testing on maps made of real breast lumps is required to determine which algorithm performs better.

Using the thresholding algorithm, we looked at the variation of size estimated across the stroke direction and size with the stroke direction. There is a small, less than 7.5% or about 1mm, but statistically significant difference in the two measurements and for the cases tested the average $p \leq 0.005$. This effect is likely because the finite extent of the head causes some distortion in the pressure distribution along it. Our model does not capture this behavior because it is two-dimensional and assumes infinite head length. Even though the difference is small, it is important to consider because it helps to set the overall measurement noise floor of the device.

This is particularly important since we are supposing that serial comparison (separated by 6 months in time, for instance) will increase the diagnostic ability of physicians. For example let us suppose that a physician makes two maps of a perfectly spherical breast lump: one from top to bottom and one from left to right and that the only difference in these maps is the elongation of the pressure distribution in the direction of stroking. The minimum resolvable difference between them would be about 15% (at the 95% confidence interval, 2 standard deviations). For the testing presented here, this is slightly larger than the average standard deviation of the measurements and thus sets the size resolution limits of the device.

A further limitation of the modeling and algorithms presented here are that they do not account for changes in tissue stiffness with strain. While we have examined the effect of these changes by varying the stiffness ratio of the lump to background, it is possible that extending the model to include the non-linear material properties measured in Chapter 3 will provide insight into how to extract these features from the map. For example, the model predicts that the width of the pressure distribution increases as the

lump stiffness decreases. In the real non-linear case, the stiffness would be changing as well. For example, one straightforward way to use the device is to make maps at increasing force levels. It is possible that as the force increases from low to high levels (and correspondingly low to high strains) the width of the lump might change for some fraction of the force increase and then might stop changing as the stiffness of the lump reached 8 times the tissue stiffness. The linear model presented here provides no way to explore this hypothesis.

A further extension of this model is to include a fully three-dimensional model of the contact mechanics. This would allow for future algorithm development to eliminate the slight differences in lump size that are seen because of stroking direction. However, given the great increase in computational complexity that such a model would entail, and the minimal change (<10%) in accuracy that would result, it is probably better to explore the non-linear tissue mechanics first, and then proceed to the full case. In addition, the model assumes that the lumps are well connected to the glandular tissue. While this is certainly true of a large fraction of lumps, there is a smaller set of them (cysts in particular as will be discussed in the next chapter) that are mobile within the planes of breast tissue. A model that incorporates this behavior would be useful to develop extraction algorithms to measure the mobility of these lumps because it might prove to be a useful diagnostic parameter.

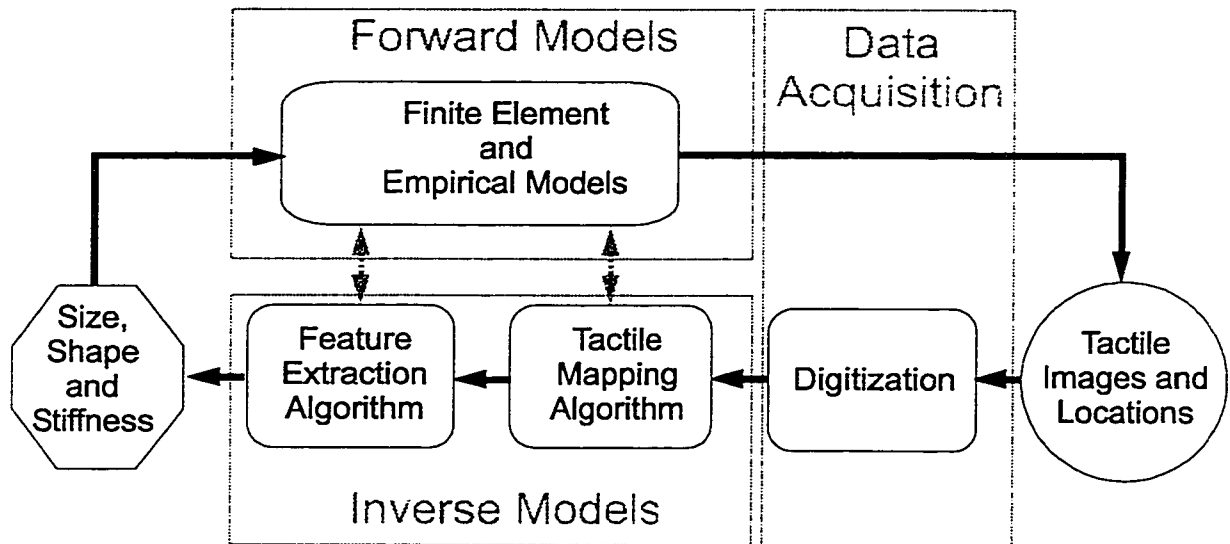


Figure 4.1: This chapter presents the finite element and empirical models (forward models) that are used to develop the feature extraction algorithms (inverse models). Tactile image acquisition and their assembly into a tactile map are detailed in Chapter 2.

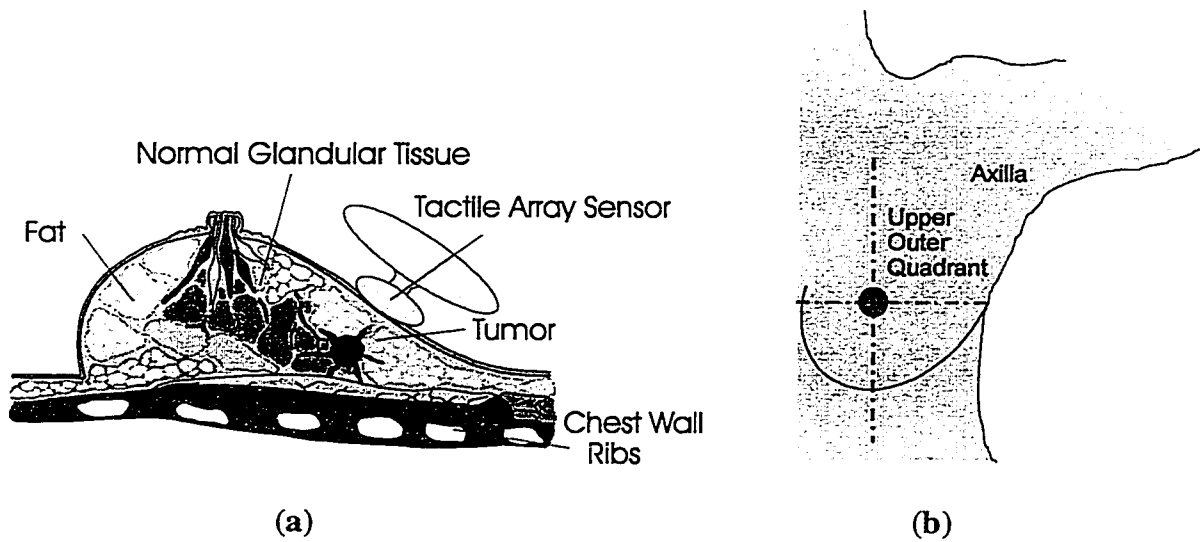


Figure 4.2: (a) The breast is many layered and inhomogeneous with a complicated three-dimensional shape. (b) It is also a pendulous organ whose thickness can be minimized when imaging by placing the patient with the ipsilateral arm raised over her head. The most common breast cancer, infiltrating ductal carcinoma, forms in the lactiferous ducts and spread into the surrounding tissue.

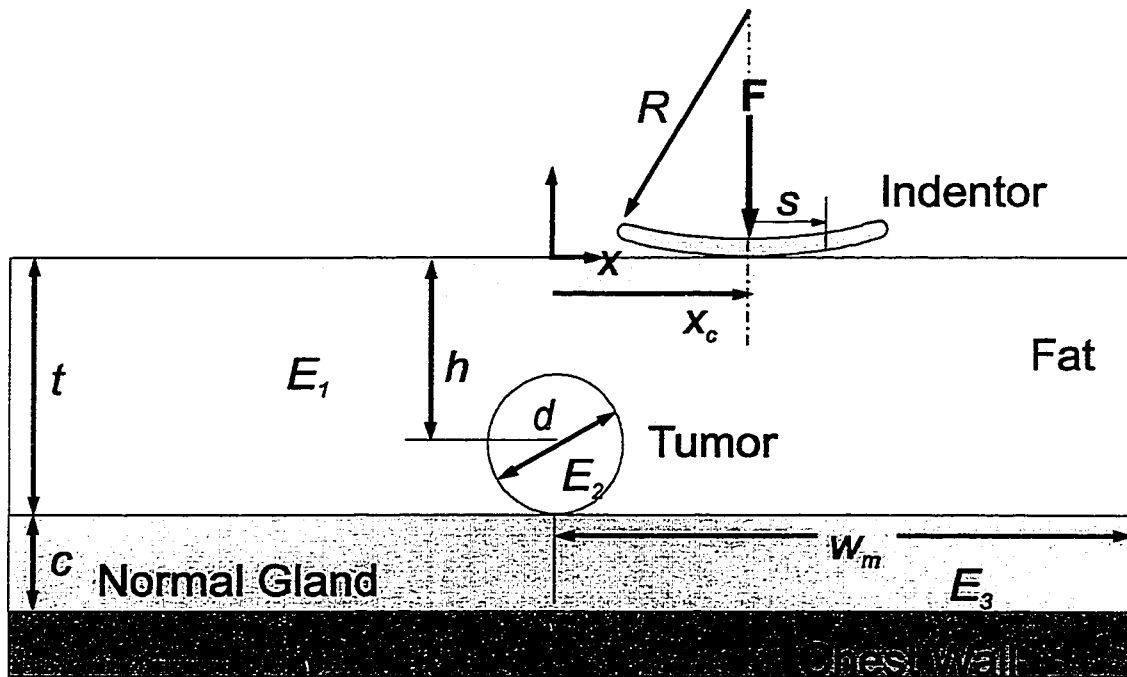


Figure 4.3: The geometry of the plane-strain finite element model.

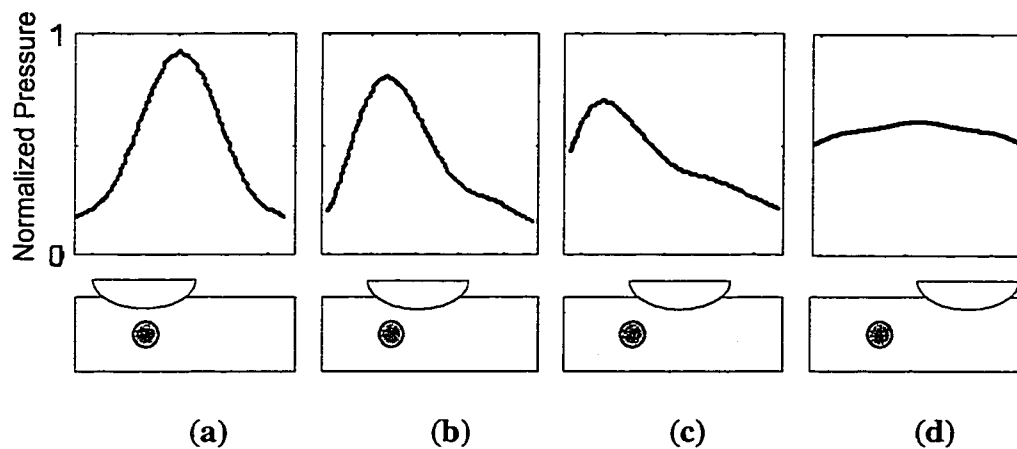


Figure 4.4: Upper plots are typical output pressure distributions from the finite element model. Lower drawings are the approximate location of the indenter for these frames. These are a sample from a 1.25cm diameter lump, 0.825 diameters deep.

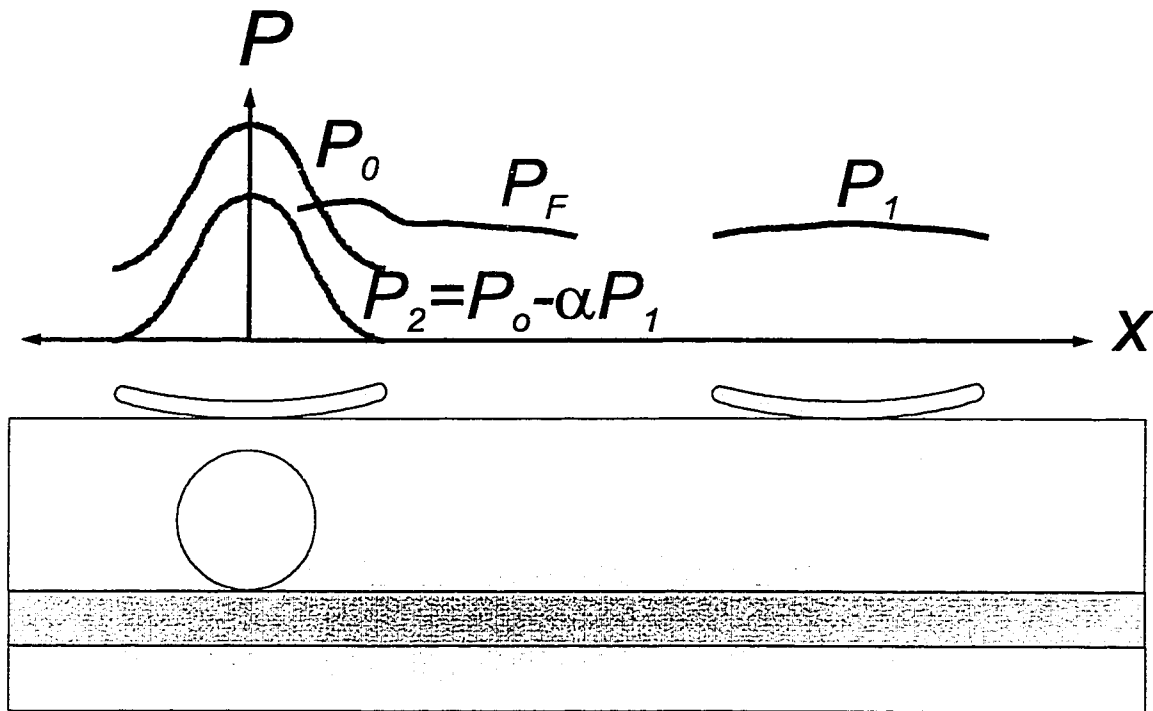


Figure 4.5: Definition of the pressure distributions P_0 , P_1 , P_2 and P_F .

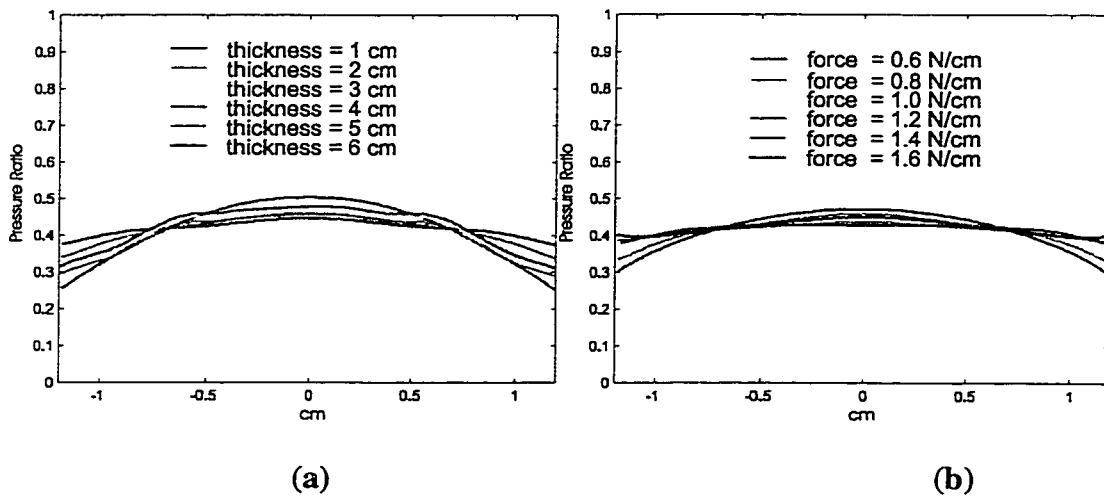


Figure 4.6: The pressure distribution P_1 normalized by the integral of the pressure as a function of, (a) tissue thickness for a force of 1.0 N/cm and (b) force for a representative tissue thickness of 3 cm. The difference between the curves in (a) is less than 5.1%, MSE, while the difference at the peak is less than 14% from 1 cm to 6 cm thickness. The difference between the curves in (b) is less than 3.7%, MSE, while the difference at the peak is less than 8% from 0.8 N/cm to 1.6N/cm.

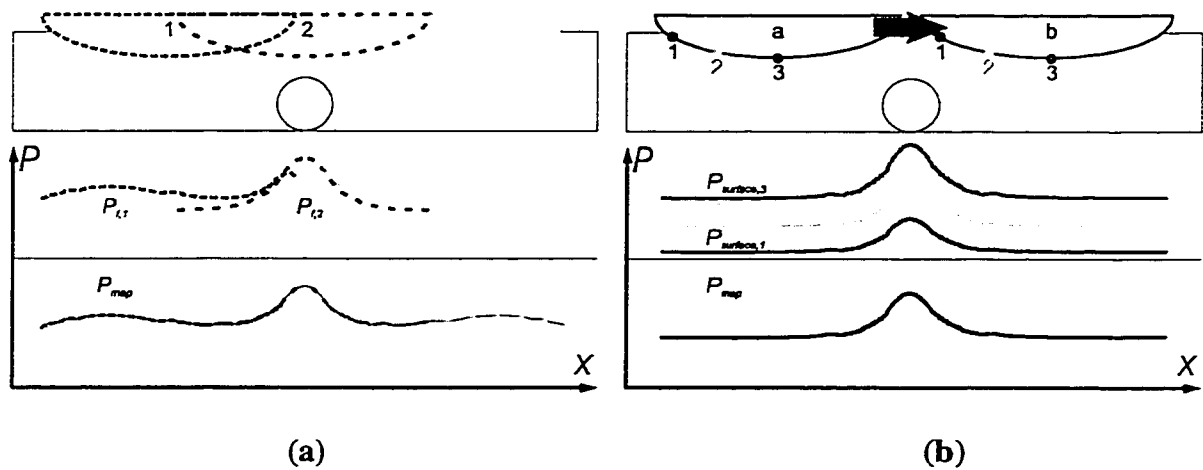


Figure 4.7: Two ways of describing the combination of individual frames into a tactile map. (a) The pressure map is the average of all of the data that passes over a particular point on the surface as the indenter slides over the lump. The upper drawing shows three representative locations of the indenter. The middle curves show the pressure distribution on the indenter at these locations while the lower curve shows the composite tactile map that is formed. (b) The map can also be thought of as the average of all of the curves produced by a particular location on the surface of the indenter as it moves from location a to location b. The upper figure shows the location of three points on the surface of the indenter as the indenter slides over the lump. The middle curves show the pressure distribution that is swept out by each of these points as the indenter slides from a to b while the bottom curve shows the tactile map that is formed.

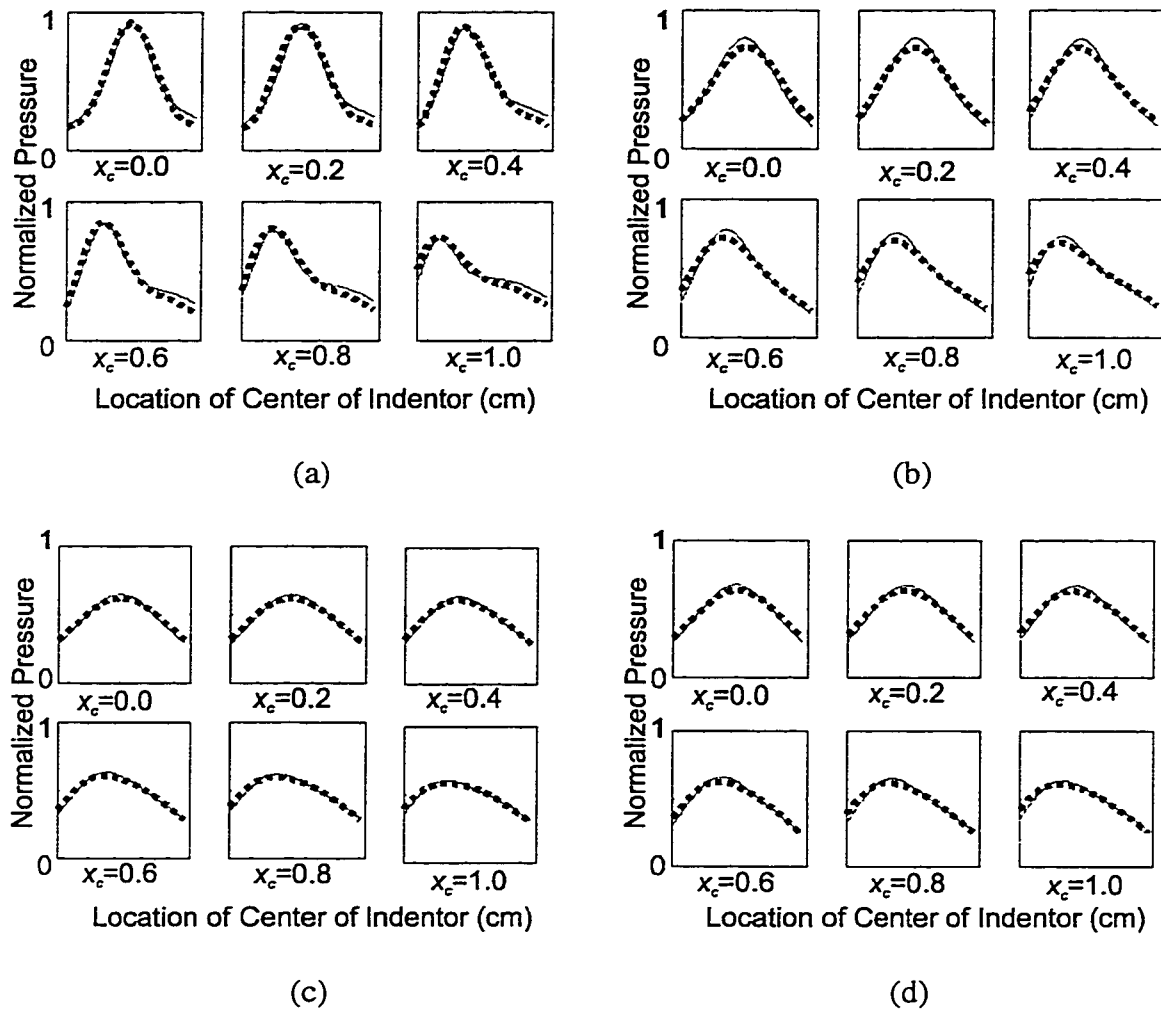


Figure 4.8: Representative pressure frames on the face of the indenter for four lumps (a) $d=1.25$ cm, $h/d=0.825$, (b) $d=1.55$ cm, $h/d=1.0$, (c) $d=1.55$, $h/d=1.4$ and (d) $d=1.875$, $h/d=1.2$. Dashed curves: empirical model, solid: finite element model derived curves.

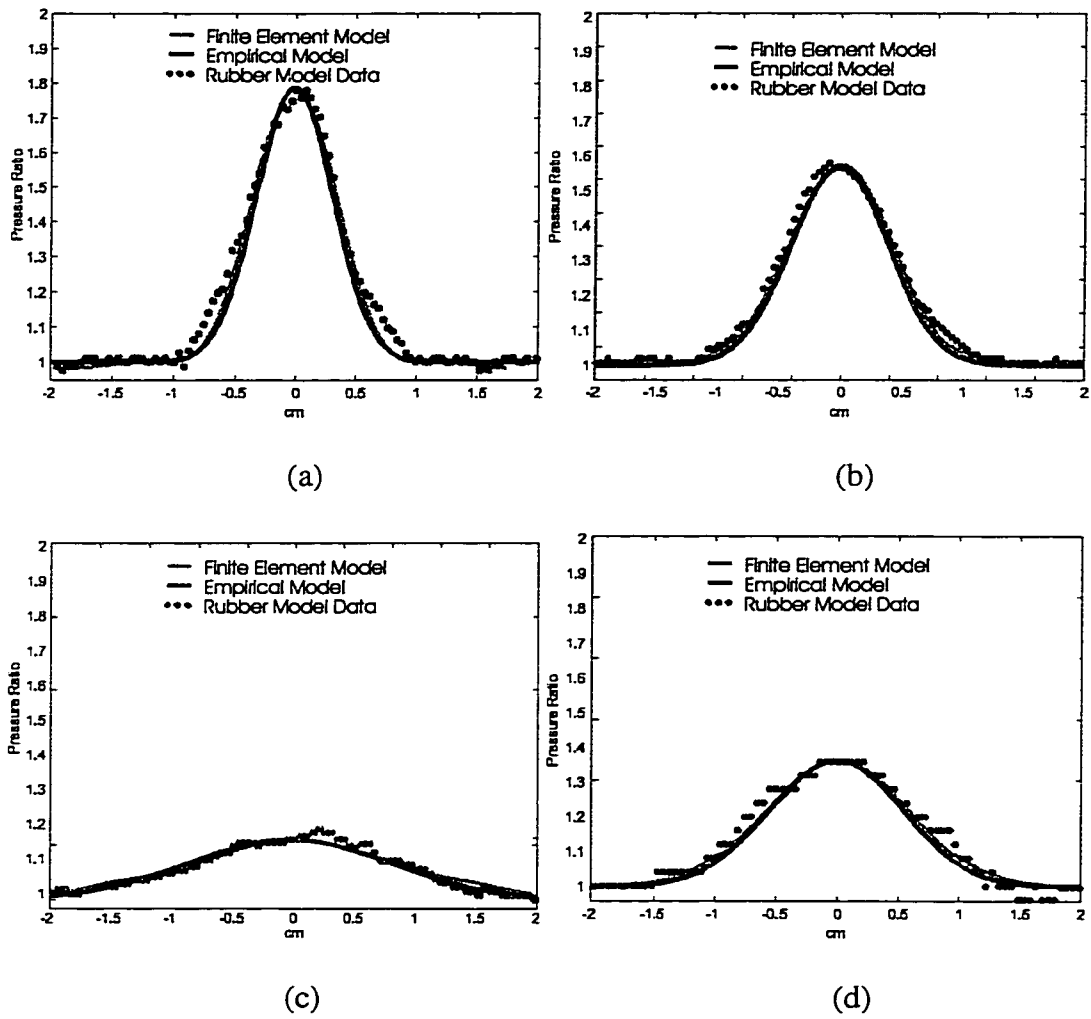
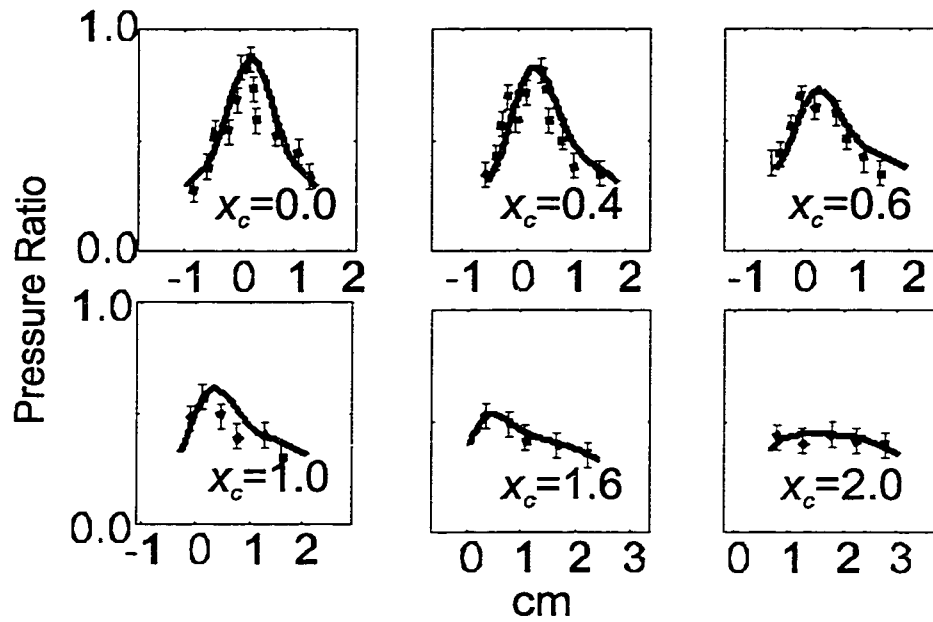
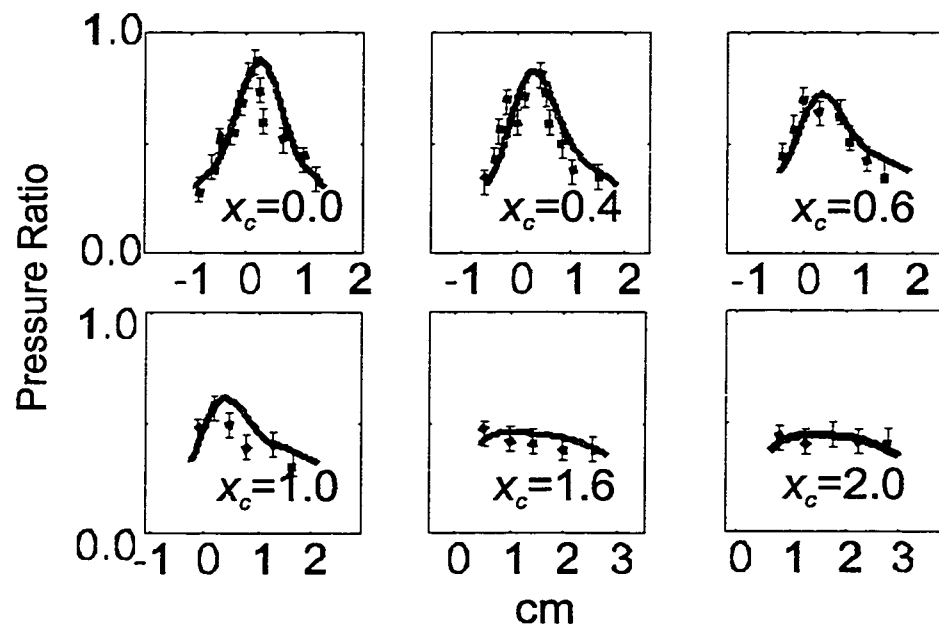


Figure 4.9: Representative maps for four lumps. (a) $d=1.25$ cm, $h/d=0.825$, (b) $d=1.55$ cm, $h/d=1.0$, (c) $d=1.55$, $h/d=1.4$ and (d) $d=1.875$, $h/d=1.2$.

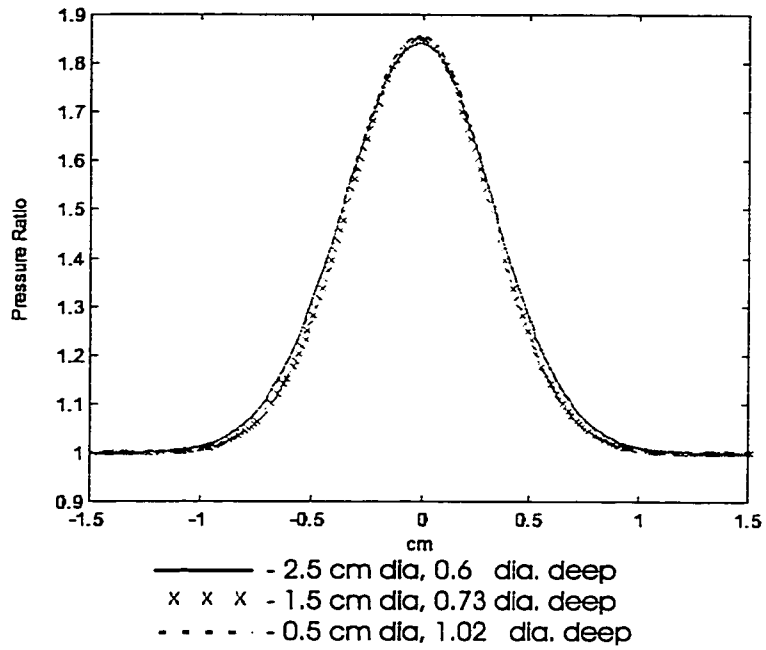


(a)

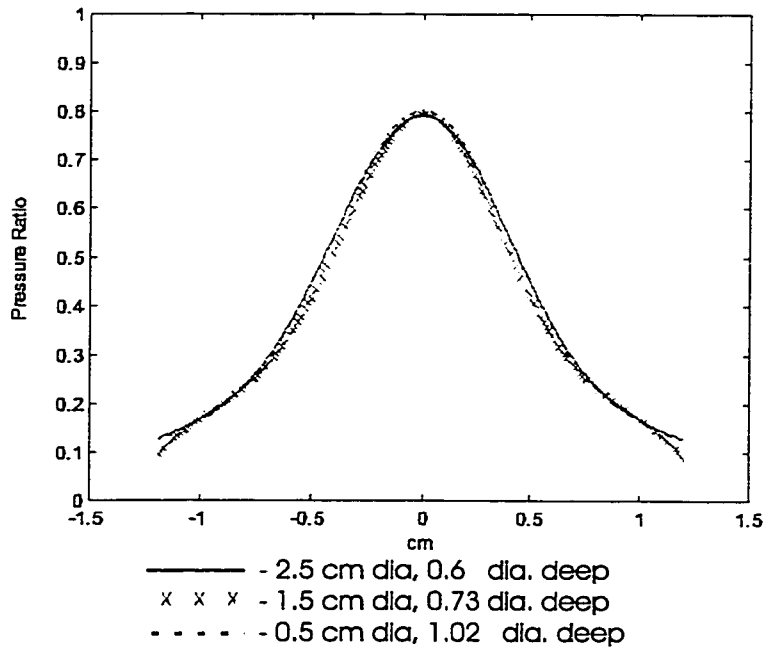


(b)

Figure 4.10: Representative single pressure frames for two lumps. (a) $d=1.25$ cm, $h/d=0.825$, (b) $d=1.55$ cm, $h/d=1.0$. Solid line: FEA model, small dashed line: empirical model, dotted line with error bars: rubber model measured frames.

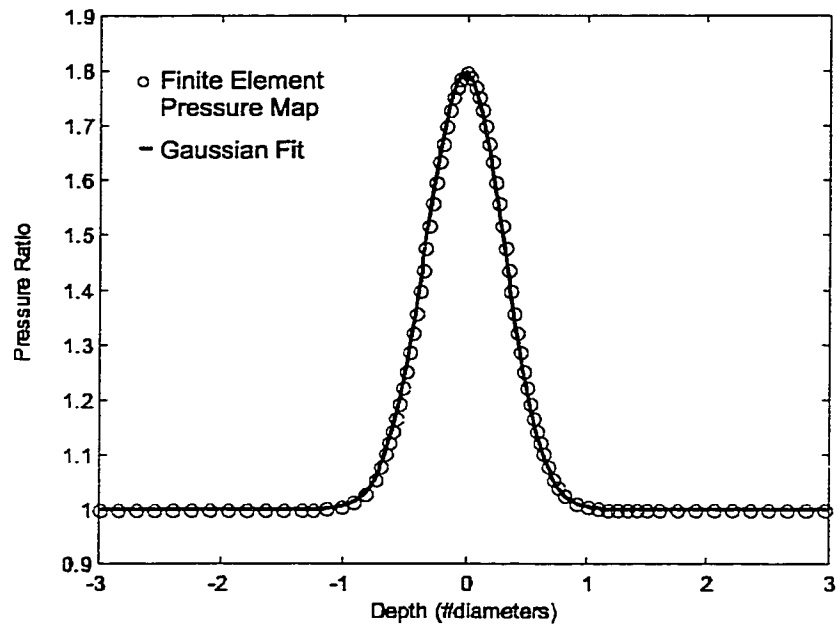


(a)

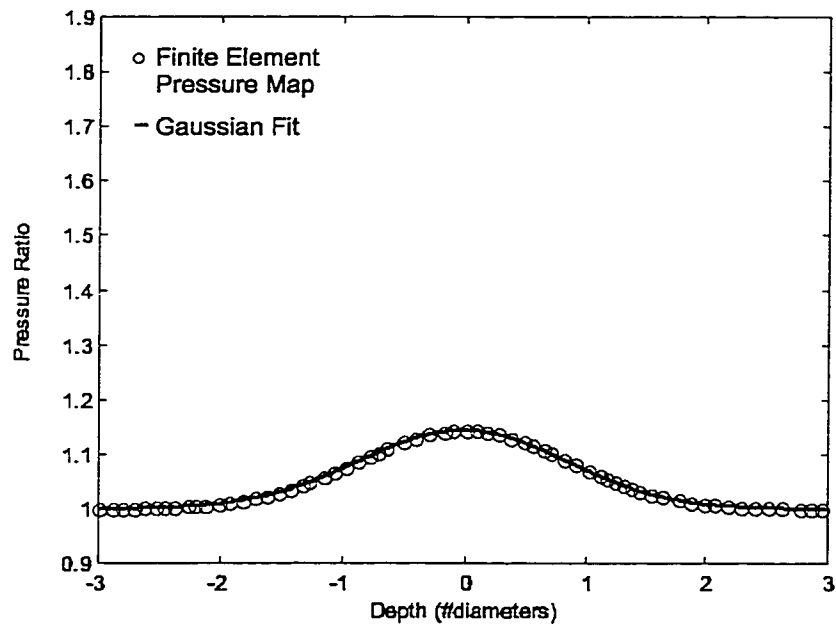


(b)

Figure 4.11: (a) The composite map pressure distributions are nearly identical (mean squared difference (MSD) < 0.5%) for three different hard lumps. (b) The single frame pressure distributions directly over the mass are nearly identical as well (MSD < 1.2%).



(a)



(b)

Figure 4.12: Representative map pressure distribution computed from the finite element models and Gaussian fits to them for (a) $d=0.5$, $h/d=1.0$ and (b) $d=2.5$, $h/d=1.0$. Circles are the finite element data, solid line is the fit to the data.

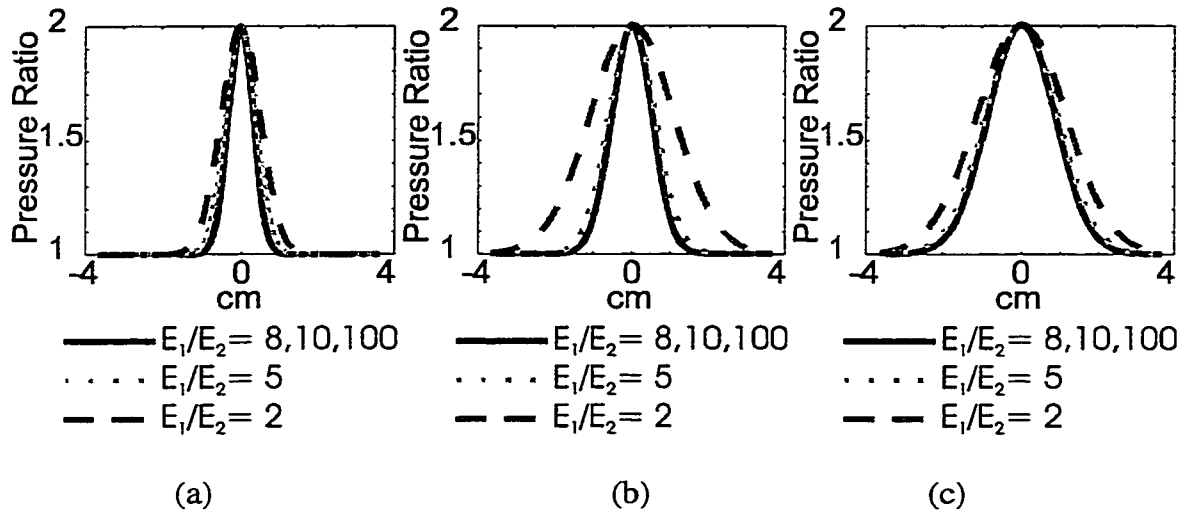


Figure 4.13: The variation in distribution width as a function of stiffness ratio. (a) For a 0.5cm diameter, 1 diameter deep lump there is less than 0.8% difference in the standard deviation of a Gaussian fit to the pressure distributions produced over a range of stiffness ratio from 8 to 100. (b) A 0.5 cm, 1 diameter deep lump and (c) a 2.5 cm , 1 diameter deep lump show the same trends as (a), with a 2.9% and 1.8% difference, respectively.

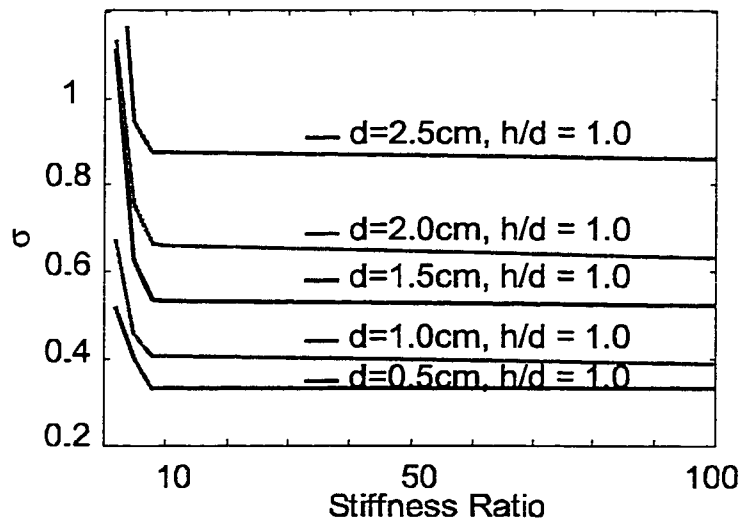


Figure 4.14: The standard deviations of a Gaussian fit to the pressure maps shown in Figure 4.12 for five different lump sizes. There is a less than 5% maximum difference in the standard deviation after the stiffness ratio is 8 or larger.

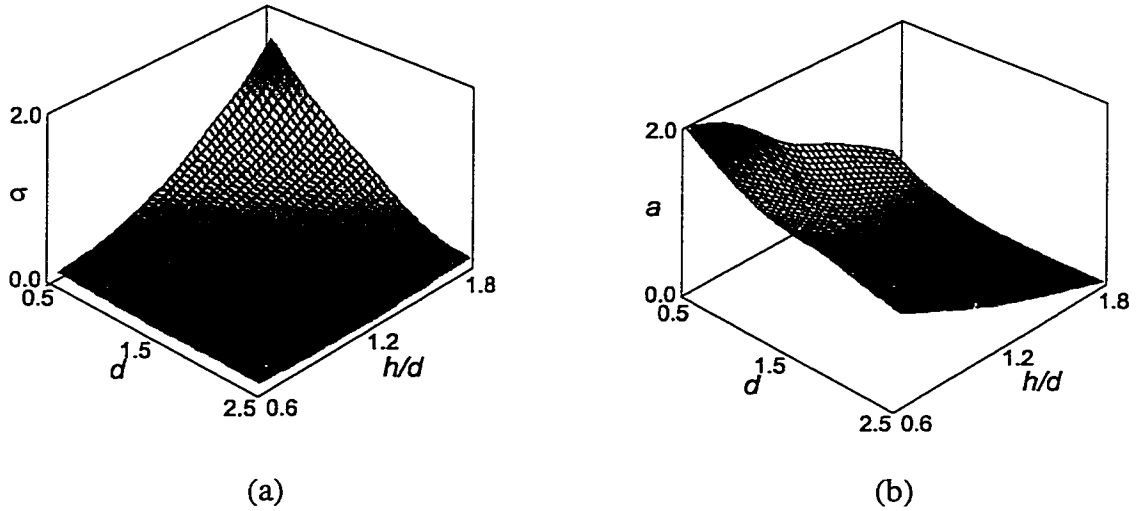


Figure 4.15: (a) The surface representing the fit parameter σ as a function of d and h/d . (b) The surface for the fit parameter a as a function of d and h/d .

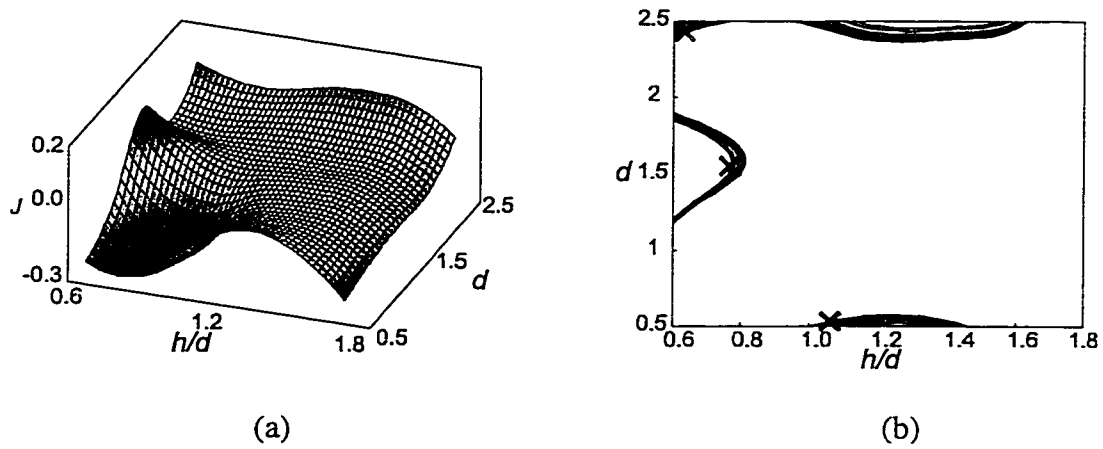
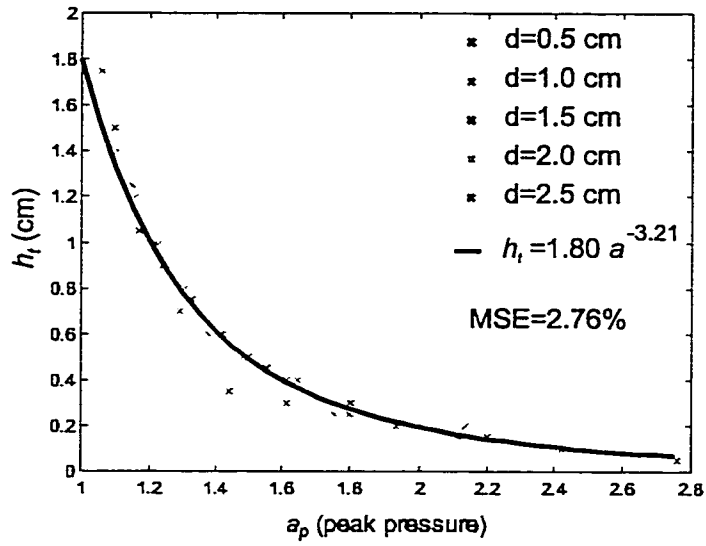
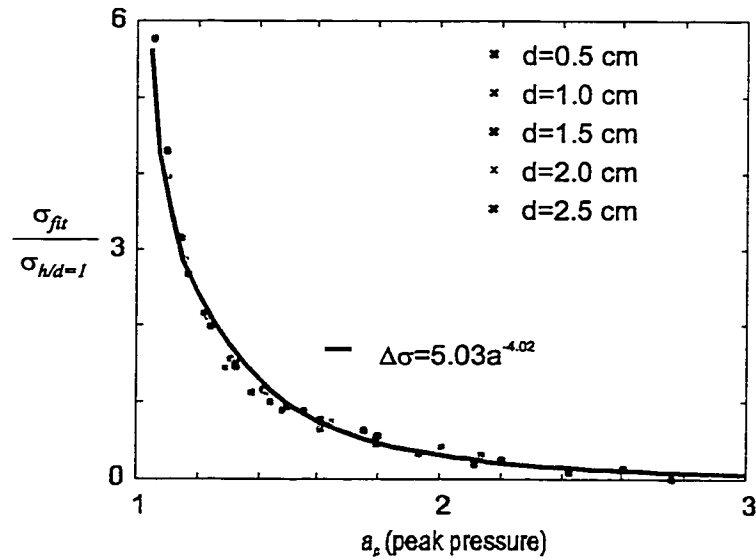


Figure 4.16: (a) Surface of $\det(J)$ as a function of σ and h/d . (b) Contour plot of the $\det(J)$ in the neighborhood of zero ($-0.05 \leq \det(J) \leq 0.05$). For depths more than 0.7 diameters, the space is nearly everywhere invertible provided there is no noise in the signal. The x symbols mark the cases presented in Figure 4.11.



(a)



(b)

Figure 4.17: Forward model trends. (a) The depth of the top of the lump from the surface of the tissue can be uniquely determined from the peak pressure in the map. (b) The percent change in apparent size of the lump is a function of the peak pressure.

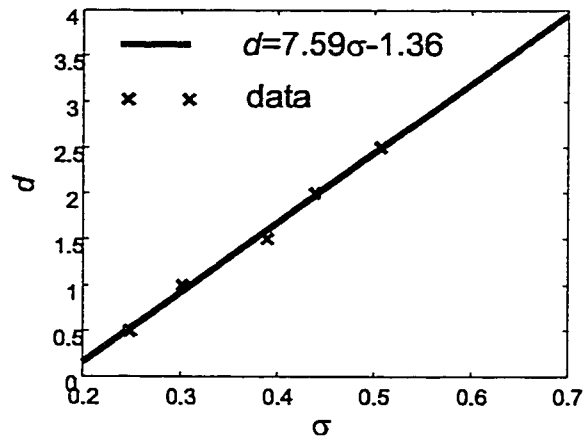


Figure 4.18: The diameter of the lump is linearly related to its standard deviation at one diameter deep, for finite element and empirical models.

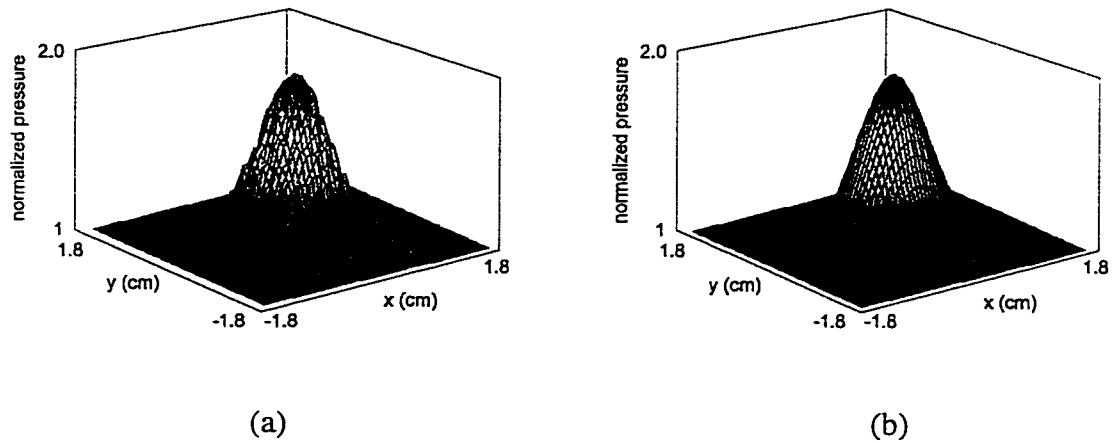
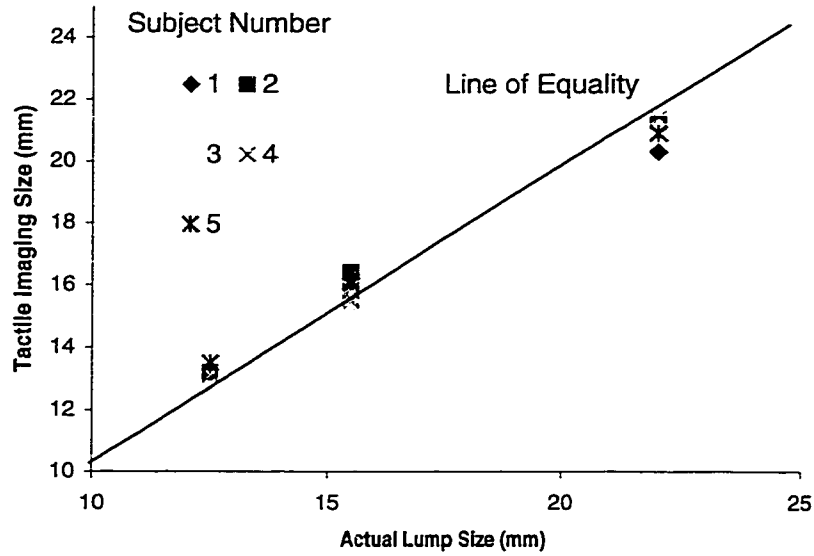
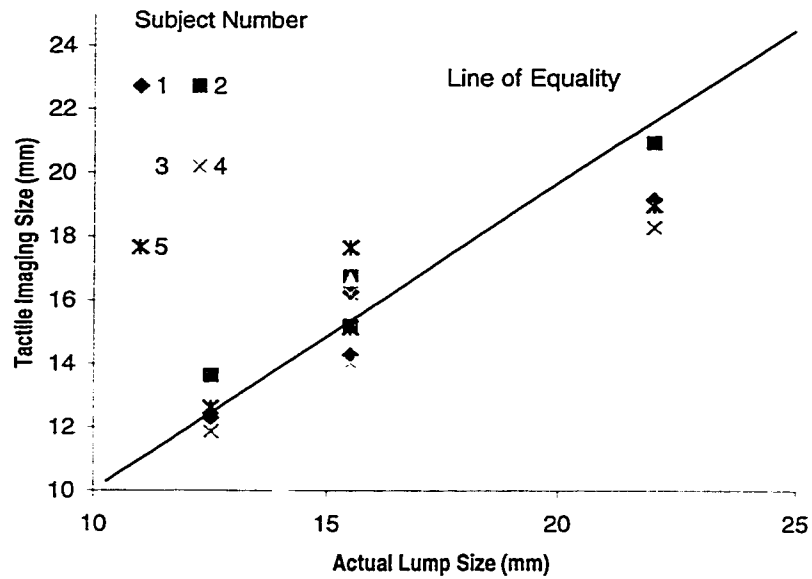


Figure 4.19: (a) Tactile map of a silicone rubber model containing a 12.5mm diameter lump, 0.825 diameters deep. (b) Two-dimensional Gaussian fit to the tactile map. There is less than a 2.8% mean squared difference between the two.



(a)



(b)

Figure 4.20: (a) Actual and predicted lump size the same lumps using the Gaussian fit algorithm. The slope of the best-fit line with zero intercept is 0.99 ($r^2=0.91$). (b) Actual and predicted lump size for 5 subjects for tests performed on four test lumps using the thresholding algorithm. The slope of the best-fit line with y intercept set to zero is 0.96 ($r^2=0.89$).

Chapter 5

Clinical Testing

5.1 Introduction

In Chapter 2 we discussed the algorithms developed to produce a tactile map and showed that they performed quite well in rubber models. They increased the signal to noise level of the pressure measurements from about 5:1 to about 50:1. In Chapter 4, we discussed forward models that led us to develop two inversion algorithms and demonstrated that they perform equivalently in rubber models, with mean absolute error less than 4% for both techniques and a mean repeatability of 8% (two standard deviations). While the performance in rubber models is quite good, these algorithms must also be validated in clinical testing because there are differences between the models and the real physical situation. Primary among these are the nonlinear tissue stiffness and the variation in tissue thickness throughout the breast that are not modeled. This chapter presents clinical experiments conducted to assess the accuracy and repeatability of the system and algorithms when two experienced breast surgeons used it.

Examining the accuracy and repeatability of the system allows us to determine just noticeable differences in size that can be used to compare one examination to subsequent ones.

5.2 Clinical Study

The clinical accuracy of tactile mapping has been assessed with a limited trial that took place in two parts. In the pilot phase of the study, a breast specialist used the device to examine women with palpable masses in their breasts. One purpose of this study was to see what range of structures (e.g. cysts, scars, ridges of normal glandular tissue) could be successfully imaged with the system. We also used the pilot study to refine the tactile mapping algorithm and system function. From this work we developed a protocol that was used to assess the accuracy of tactile imaging. We also observed that the various measurement modalities (ultrasound, CBE, mammogram) did not appear to be well correlated to each other. This raised the question of what technique should be used as a standard for lump size comparison.

Based on the observations of the pilot study, we performed the second portion of the study in a surgical setting where we could obtain accurate measurements of lump size by palpating and directly measuring the extracted tissue samples. By necessity this has restricted us to a patient population with predominantly cancer, but it is an essential first step toward evaluating the device. Also in this study, we can determine the relative accuracy of the other size estimates and decide which is the best one to use for comparison in subsequent studies. In addition to the size estimates, we also made tissue stiffness measurements of the extracted samples as described in Chapter 3.

The clinical studies were conducted in collaboration with Assurance Medical as a proof-of-concept for tactile imaging. Subjects were voluntary, unpaid participants who gave written informed consent. Following a protocol approved by the appropriate human subjects review boards, they received mammograms, ultrasound examinations and clinical breast examinations following the usual course of treatment. Because this is a preliminary study to demonstrate the feasibility of tactile imaging and because the experimental data taken in rubber models showed little variation (see Chapter 4) only two surgeons participated. These surgeons were Dr. Edward Dalton of Northern New England Surgical Associates, Bedford, New Hampshire and Dr. Kenneth Kern of Hartford Hospital, Hartford, Connecticut and the University of Connecticut School of Medicine, Storrs, Connecticut. One surgeon made two to five tactile maps of each lump just prior to surgery using different stroking techniques to examine the effect of examiner technique on map to map repeatability.

We estimated the maximum and minimum size of the lumps in each of these maps using the technique described above. The clinician also reported the maximum size of the lump as determined through clinical breast examination. Tumor size estimates were obtained from the mammogram report prepared by the radiologist and from the pathologist's report. The size of the lump was estimated from transverse and axial ultrasound images of the lump as marked by the ultrasound technician or clinician. The patients were then followed through surgery where the lump was removed. After excision, the lump was bisected parallel to the plane of the tactile map and a caliper was used to measure the maximum and minimum palpable extents of the lump. One African-American and twenty-four Caucasian women participated in the surgical study. They

ranged in age from 39 to 84 years old. Nineteen infiltrating ductal carcinomas, three fibroadenomas, one lobular carcinoma, one papilloma and one mass of fibrotic adipose tissue were examined. Of the women in the study, eighteen were post menopause while seven were pre menopause. Eleven of the lumps were in the upper inner quadrant, seven were in the upper outer, six were in the lower outer and two were in the lower inner quadrant.

5.2.1 Pilot Study Results

In the pilot phase of the study we made maps of women with palpable masses in their breast and tested the ease-of-use of the device. The clinicians found it to be simple to use and had minimal difficulty in learning appropriate clinical technique. It took between 20 and 40 seconds to generate each of the maps in this study. Good clinical technique was important to produce repeatable maps that subjectively reflected the palpable extents of the mass. To assess the effect of the clinical technique on map repeatability and size accuracy, we asked the physicians to use a variety of imaging techniques, subject to the restriction that they must included multiple passes where the sensor breaks contact with the skin. This restriction was included to be sure that the noise process of the sensor is Gaussian as described in Chapter 2. To stabilize the breast and minimize its thickness, the patients were placed into a supine position with the ipsilateral arm raised over the head, as shown in Figure 2.3. If the breast was particularly mobile (as was the case with older women with large breasts) the physician also stabilized the tissue with his free hand. We saw good subjective performance of the system (the physicians and even the patients remarked that the tactile maps appeared close to their perception of the shape of the mass during physical examination). We were

able to make tactile images of a wide variety of structures, ranging from scars, ridges of normal glandular tissue, cysts, fibroadenomas and infiltrating ductal cancers.

Figure 5.1 demonstrates that it is possible to image scar tissue and normal glandular tissue in the breast. It also shows that it is possible to image multiple structures during the same examination. Figure 5.1 and the maps that follow also show some noise around the edges of the map that is a characteristic artifact of the tactile imaging process. These edge effects result when the indenter makes and breaks contact with the skin, and are ignored during analysis. They are a result of normalizing frames that are acquired when the sensor is not fully in contact with the tissue. When this is the case, the pressure values over a portion of the sensor are higher than they would be for a given indentation force when the head is completely in contact with the tissue. When they are normalized by the average, and added into the map, they appear as high points in the pressure image. This can be corrected in subsequent generations by excluding those frames where only partial contact is made.

Figure 5.2 shows a cyst in the patient's left breast and demonstrates an interesting imaging artifact that is produced by motion of the structure within the tissue. The image was made with swipes of the scan head from upper right to lower left and the lump shows characteristic smearing or a "comet tail" in the direction of motion of the scan head. Figure 5.3 shows a ridge of normal glandular tissue that "feels like a suspicious" mass. It was not visible on mammograms and illustrates the real clinical utility of the device – following suspicious masses for changes in time, since both the radiologist and the surgeon remarked that neither the mammogram nor the ultrasound images were useful for examining this mass.

5.2.2 Surgical Study Results

Figures 5.4 and 5.5 show two tactile maps made during the surgical study. They are both of infiltrating ductal cancers, and demonstrate the imaging capabilities of the device in the surgical trial. Figure 5.5(c) shows a photograph of the infiltrating ductal cancer after surgical excision and bisection. The cancer is easily visible in the photo because the normal glandular tissue has been replaced by fat and there is good correlation between visual and palpable size. Typically, the cancer is not easily visible; we palpate the tissue to find the edges of the lump and measure its extents using a caliper. Multiple measurements made of 4 lumps by two different examiners reveal that the size estimates are repeatable to within about 5% (95% confidence interval).

The ex vivo size measurements make it possible to compare the size estimate accuracy of the various imaging modalities. Figure 5.6 shows the comparison of ultrasound maximum size estimates and CBE maximum size estimates to the ex vivo size of each mass. Figure 5.7 shows a comparison of the maximum size estimates made from the tactile maps using both size extraction algorithms to the maximum ex vivo size. In Figure 5.8, we compare the minimum size estimates made from tactile images using the two algorithms to ex vivo size estimates of minimum size. Typically, only maximum size was estimated from the other modes, and therefore there is no minimum size comparison for these modes.

Size is not presented from the mammograms because typically only presence or absence of the lump and level of suspicion were usually reported. Of the 25 masses in the study, 24 were visible on the mammograms. Figure 5.9 compares the pathology measurements of cancerous tumor size with the ex vivo palpable size measures; no

results are presented for other kinds of tissue because the pathologists did not report size for these cases. In one patient, the mass was not visible on ultrasound, and in one it was not palpable; they are shown as masses with zero diameter in the figures. In both cases they were visible in the tactile maps.

We chose the three maps that showed each lump most clearly and used the two inversion algorithms to estimate the size. The average standard deviation in size for the estimates made with the thresholding algorithm was 7.5% (1 standard deviation) for maximum size estimates and 7.5% for minimum size estimates, across all size estimates. The Gaussian inversion algorithm showed 15% and 19% for these statistics, respectively. The mean absolute error, MAE, in the average maximum size measurements made with the thresholding algorithm was 12% while for the Gaussian algorithm it was 17%. For the minimum size estimates the MAE was 19% and 17% for the thresholding and Gaussian fit algorithms, respectively. Ultrasound exhibited MAE of 34% when compared to maximum ex vivo size while CBE had MAE of 47% for this same statistic. Pathology showed 28% MAE on the patients with cancer. It was not possible to estimate the variation in these modes because only one examination was performed. Table 5.1 summarizes these statistics. . There is no statistically significant difference in any of the size estimates between the pre- and post-menopause patients.

Technique	CBE	Ultrasound	TI (Thresholding)	TI (Gaussian Fit)
Mean Absolute Error	47%	34%	12%	17%
Slope of Best-fit line (ex vivo size comparison)	0.9	1.26	0.96	1.04
Correlation Coefficient (r^2)	0.14	0.49	0.61	0.6

Table 5.1 Table of fit statistics for the various techniques examined.

5.3 Discussion

5.3.1 Examination Mode Comparison

Both inversion algorithms demonstrated significantly better accuracy than either ultrasound or CBE maximum size estimates. In fact, both schemes were more than twice as accurate as ultrasound and nearly three times as accurate as CBE (on the basis of MAE). Both inversion algorithms were also better correlated to the size of the lump than either ultrasound or CBE (r^2 for thresholding was 0.61, for Gaussian fit it was 0.62, while for ultrasound and CBE it was 0.14 and 0.39, respectively). These results demonstrate that tactile imaging is a more accurate way to determine the size of breast masses than either CBE or ultrasound. It is also potentially more sensitive than either, because in this set of twenty-five masses imaged, it was able to find one lump that was non-palpable, and one lump that was not visible on the ultrasound images. It is curious that ex vivo size estimates and pathology estimates of size are not better correlated. However, this can be explained by considering the nature of infiltrating ductal carcinoma, and the nature of pathology measurements of size. Pathologists typically measure the size of the tumor on

slides that are prepared from slices of it and look for microscopic infiltration in to the surrounding tissue. These microscopic tendrils of cancer may not be palpable

One of our goals was to develop images that are easy to interpret. Subjectively, the clinician and the patients who viewed the images found them easy to interpret, and often remarked that the tactile map closely resembled their mental image of the structure as they palpated it. Instructing the examiner to continue stroking until the map adequately reflects the palpable extents of the mass while immobilizing the breast with the free hand effectively specifies clinical technique.

While the thresholding algorithm and the Gaussian fit algorithm produce nearly identical average size estimates they show greatly different variances. The Gaussian fit algorithm produces a less repeatable estimate of lump size since one standard deviation of maximum size was 15%, while for the thresholding algorithm it was 7.5%. For the minimum size estimates, this statistic remains unchanged at 7.5% for the thresholding algorithm, but climbs to 19% for the Gaussian algorithm. This result seems counterintuitive, since one might expect that a model based approach would perform better than an ad hoc thresholding scheme. However, this difference can be explained by examining the noise in the tactile maps.

In multiple maps made of the same lump, the peak pressure varies by an average of 14% (one standard deviation), across all subjects. Since the inversion algorithm relies on this value to determine the depth of the lump and correct for its size, it is not surprising that the algorithm shows poor repeatability. The variation in peak pressure is a direct result of the signal-to-noise ratio of the sensor at the individual pressure image level. To see this, consider that the frame average is repeatable to only 10% and

therefore only changes in mean of roughly 10% or greater are observable. If we assume that a typical lump covers 20 elements in the individual image, then the pressure in those elements could be as large as 20 kPa in a frame with 6.9 kPa average, or almost a threefold variation.

In contrast, while the variation in peak also causes a variation in the threshold level in the thresholding algorithm, the distribution width does not change very much with threshold level. Thus this latter algorithm performs better. The Gaussian fit algorithm does not provide better performance than the simple thresholding algorithm and it is significantly more computationally complex: it took an average of 15 seconds to compute the size of lump, compared with a fraction of a second in the thresholding algorithm. Given the computational complexity of the fit algorithm and its relatively poor performance, the thresholding algorithm is the clear winner for finding lump size.

5.3.2 Repeatability

Using the thresholding algorithm to estimate size, rubber model experiments showed better than 5% repeatability (see Chapter 4), while in the clinic mean repeatability (across multiple maps of a single lump) is about 7.5% for the thresholding algorithm. This result implies that a just noticeable difference in size (95% confidence interval or two standard deviations), is a 15% change (e.g. if the original size was 10 mm and subsequently it is greater than 11.5 mm then it has changed). In contrast, the 95% confidence interval for CBE was measured to be larger than a 40% change in diameter (Lavin and Flowerdew 1980). Minimizing detectable lump size change is important because there is good correlation between small size at discovery and positive patient outcome (Harris 1994). These test results demonstrate that tactile imaging can improve

the repeatability and accuracy of breast examination when determining size of the mass, at least in this population of surgical patients. However, there are some significant experimental limitations to this study, discussed below, which make it difficult to generalize this repeatability number to the larger population of patients.

There are a number of possible reasons why tactile imaging performed so much better than ultrasound, which is considered by physicians to be highly accurate for estimating size (Dalton 1998, Krag 1998, Kern 1998). Because the physicians estimated the size of the lump directly from the ultrasound images, if the lump did not have clearly defined borders in the image, it would be difficult to assess its size. This was often the case; the borders of the cancer appeared to be ill defined. In contrast, the borders were clearly defined in the tactile images. One possibility is that the elastic stiffness contrast between cancer and normal tissue spans a greater range (about 10^2) than the bulk modulus contrast that is imaged by ultrasound. Because the fundamental contrast is greater, the tactile images have better resolution of the edge of the lump which in turn leads to more repeatable and accurate estimates of size. A further study, including multiple examiners for all examination modes is required to resolve this question.

5.3.3 Experimental Limitations

There are some significant limitations to the study discussed, make this study a proof-of-concept, not a proof of the effectiveness of tactile imaging. The first limitation is that the patient population tested in the surgical study is not the patient population that the device will likely be utilized in. A larger population composed of women with difficult breast examinations and benign breast lumps, must be included in the subsequent study in order to address this shortcoming. Second, this study only looks at map

repeatability at a single instant in time. Since the device will be used for time series comparisons, a study that compares maps made of lumps at different times (separated by a six month interval, for example) in the same patient must be conducted in order to assess the true repeatability of the device.

This latter study is a very difficult one to perform because our work shows that size estimates from the other commonly available modes are not well correlated to actual lump size. The best correlated modality, other than tactile imaging, of the ones tested was CBE, and this should be used for future comparison studies. The best way to do this study would be to ask multiple examiners to palpate the breast of a woman with a known benign breast structure. The examiners could separately report size information, and then make a tactile map of the structure. More than one examination allows for the different maps to be compared to each other, and also gives an idea of the innate variation in the measurements. The patient could return after six months, and the procedure could be repeated. Given a large enough sample of patients, this study should allow for the determination of the accuracy and repeatability of tactile imaging.

5.3.4 Future Work

In order to extend tactile imaging from a purely documentary function to a more diagnostic role, it is necessary to quantify features other than size. Two parameters that appear to be important to determining the nature of a lump from palpating it are its hardness and its mobility (Dalton 1998, Kern 1998, Krag 1998). In order to determine these parameters a model-based approach is required because the pressure distributions depend on a combination of lump depth, size and hardness. Provided it is possible to find a way to further reduce the variation in peak pressure that exists in the map, it should be

possible to extract the depth of the lump from this measure. Once the lump depth is known, it may be possible to develop algorithms that can extract the hardness. This perhaps could be accomplished by making multiple tactile maps at different pressure levels and measuring the changes in feature magnitude.

Additional information is also likely available on the individual tactile image level. If the pressure images are reasonably accurate on this level it may be possible to extract the mobility of the lump. Tracking the motion of the lump across the face of the indenter as the lump slides over it is one way to measure its mobility. In the simplest case if the pressure distribution remains fixed with respect to the face of the indenter, this indicates that the lump is being ploughed through the tissue by it and is therefore highly mobile. In contrast, if the lump slides across the indenter, then the lump is well anchored to the surrounding tissue. Since the individual pressure frames appear to be a relatively flat distribution with a lump-like distribution superimposed on them, it is likely that motion can be quantified by computing the motion of the center of pressure with respect to the motion of the indenter. It might also be possible to identify the motion effects by looking at the size of the lump perpendicular to the stroking direction because this size should be unaffected by smearing caused by motion.

We also note that much of our work in developing the system has involved correcting for, or suppressing imaging artifacts. However, some of these artifacts may contain information about the structures that were imaged. For instance, Figure 5.2 shows the characteristic “comet tail” that is associated with lump motion that may prove to be a useful diagnostic parameter. An analogy to ultrasound is appropriate here. When ultrasound first gained use as a breast imaging tool, it was used primarily for visualizing

structures in the breast. As its use became more widespread, physicians began to recognize certain characteristics of the images that were diagnostic in nature. For example, cysts usually appear as dark spots in the image with posterior amplification because the cyst acts like a lens that focuses the ultrasound (Harris et al. 1994). Other markers frequently associated with cancer are an oblique aspect ratio (cancers appear to be wider than they are tall) as well as posterior attenuation and edge shadows from cancers. These imaging artifacts have become recognized characteristics of ultrasound images and are accepted for diagnostic purposes (Harris et al. 1994).

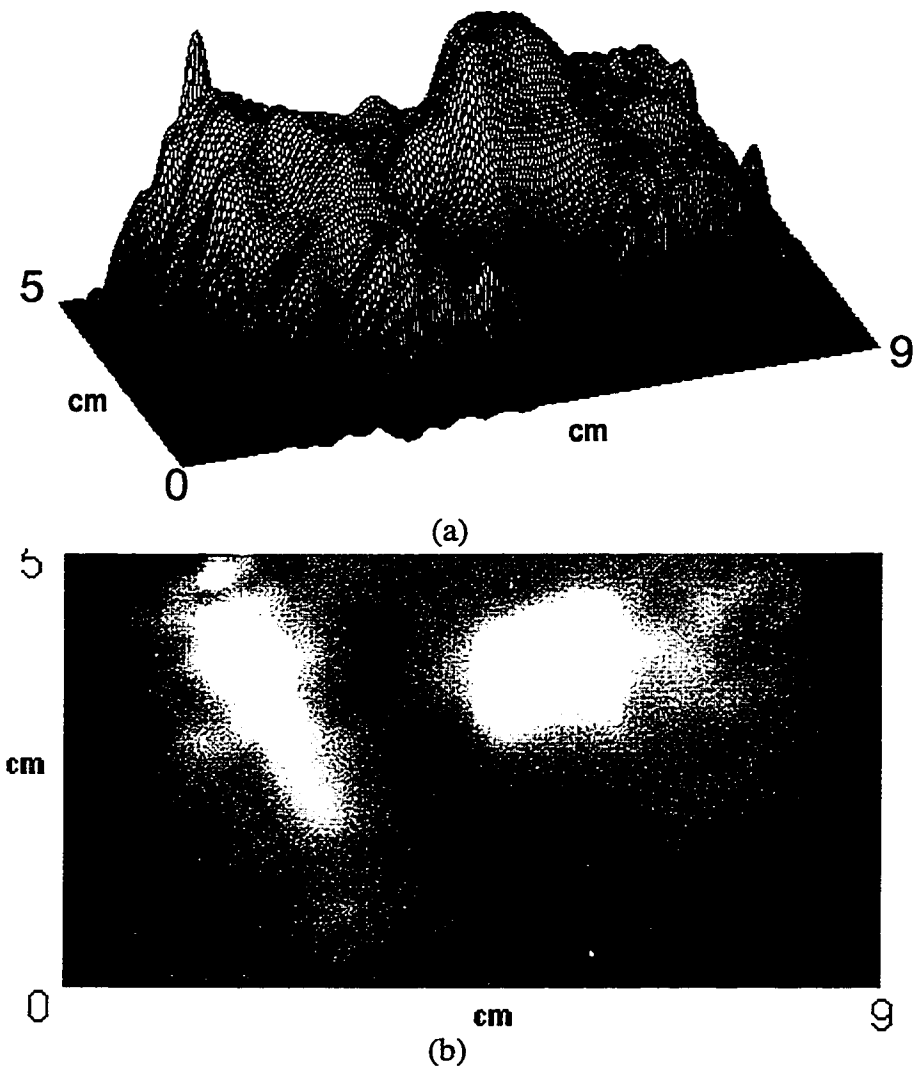
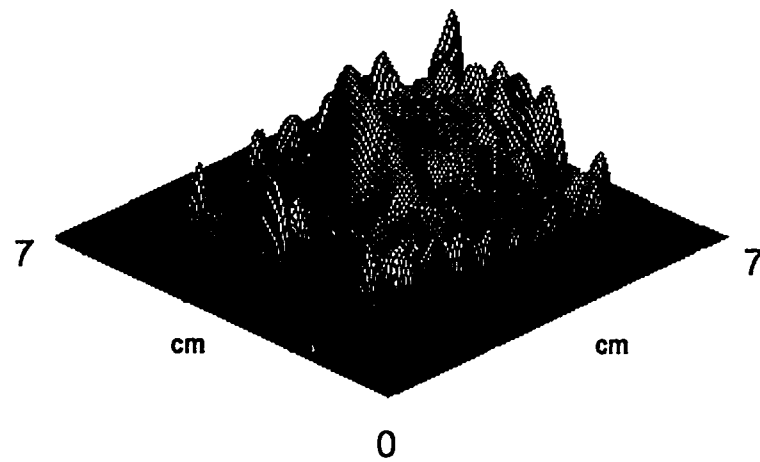
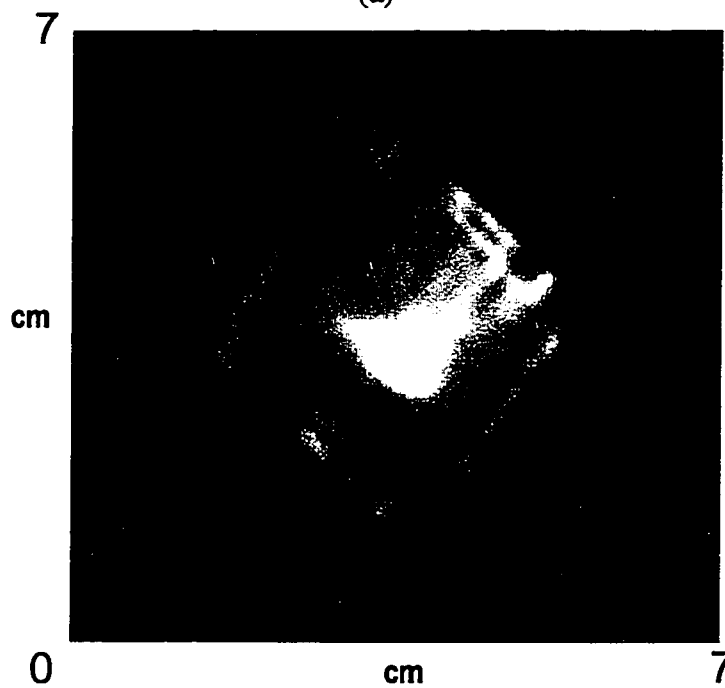


Figure 5.1: (a) A three-dimensional topographic view of the tactile map made of a portion of the right breast of a 47 year old Caucasian woman. (b) False color contour plot showing a scar from a previous biopsy (on the left) and a benign lump of normal breast tissue. The scar was estimated to be 5 cm by 2 cm using CBE, while the lump was estimated to be 5 cm by 5 cm, while in the tactile image the scar is 4.5 cm by 2 cm and the lump is 3 cm by 3 cm. The lump was 1.3 cm by 1.1 cm on the ultrasound images.



(a)



(b)

Figure 5.2: (a) A three-dimensional topographic view of the tactile map made of a cyst in the left breast of a 51 year old Caucasian woman. (b) False color contour plot showing the cyst in the center of the map. The cyst was imaged from upper right to lower left, and was slightly mobile. The map shows a characteristic “comet tail” smearing in the direction of motion of the scan head because it was not possible to completely immobilize it. The size of the cyst was 1 cm by 1 cm on CBE, 1.5 cm by 1.9 cm in the tactile image and 1.8 cm by 1.8 cm in the ultrasound image.

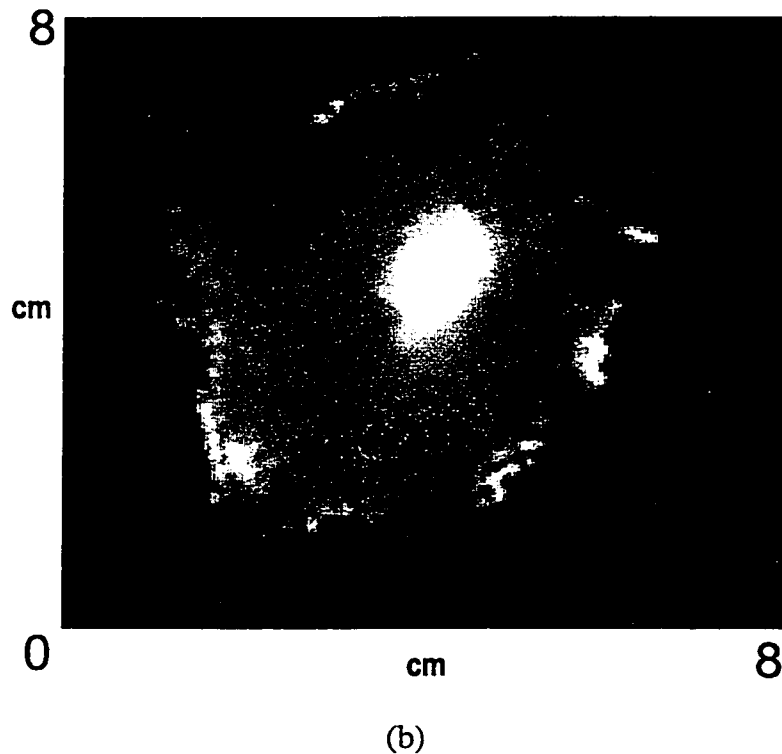
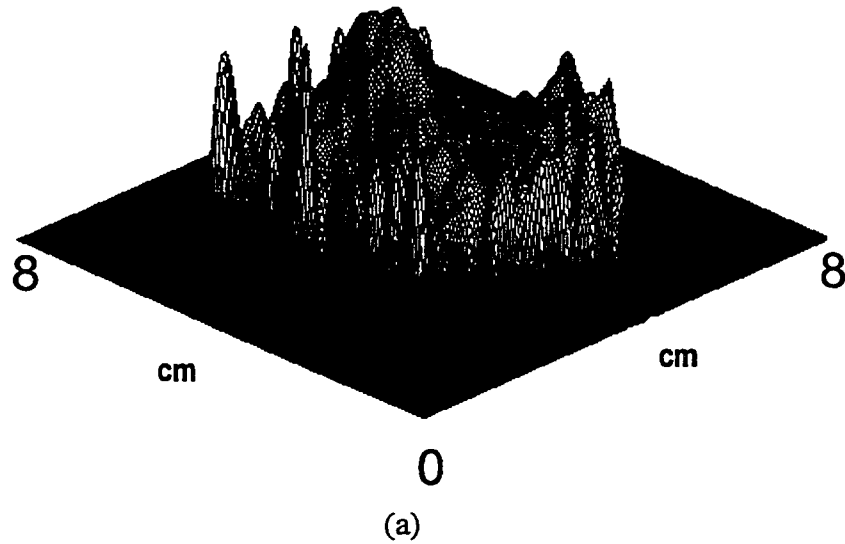


Figure 5.3: A three-dimensional topographic view of the tactile map made of a benign ridge of tissue in upper outer quadrant of the left breast of a 49 year old Caucasian woman. The ridge is the highest point in the back center of the map and follows the normal glandular tissue and tapers into the breast. (b) False color contour plot showing the ridge in the center of the map. In CBE assessment, the ridge is 2 cm by 2 cm while tactile imaging estimates it at 1.8 cm by 1.5 cm. The readily palpable lump was not visible on the ultrasound images nor on the mammograms, prompting the radiologist to report that evaluation of the lump “will have to depend on Dr. Dalton's physical examination, [with] careful clinical follow-up in 6 months.”

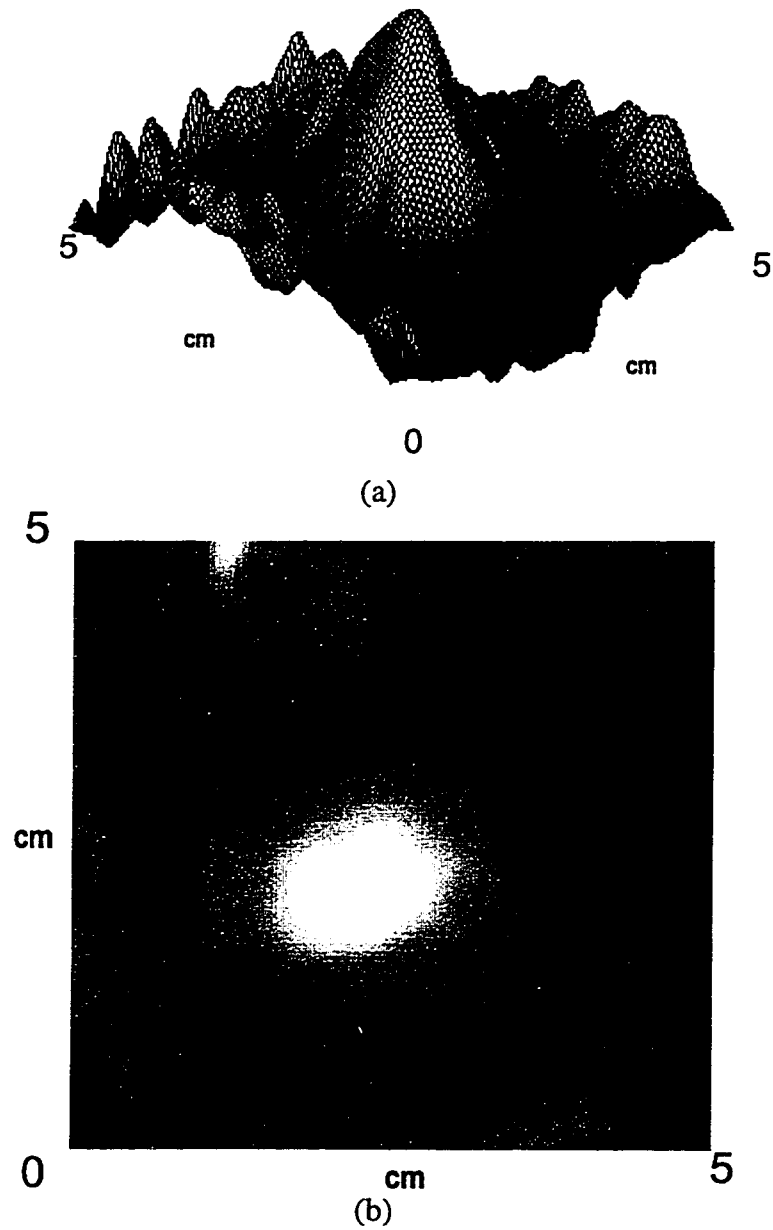


Figure 5.4: A three-dimensional topographic view of the tactile map made of an infiltrating ductal carcinoma in left breast of a 57 year old Caucasian woman. (b) False color contour plot showing the cancer in the center of the map. In CBE assessment, the mass is 1 cm by 1 cm while tactile imaging estimates it at 1.5 cm by 1.4 cm. Ultrasound puts its size at 0.8 cm by 0.8 cm. This patient was part of the later surgical trial, and upon excision the lump measured 1.1 cm by 0.9 cm.

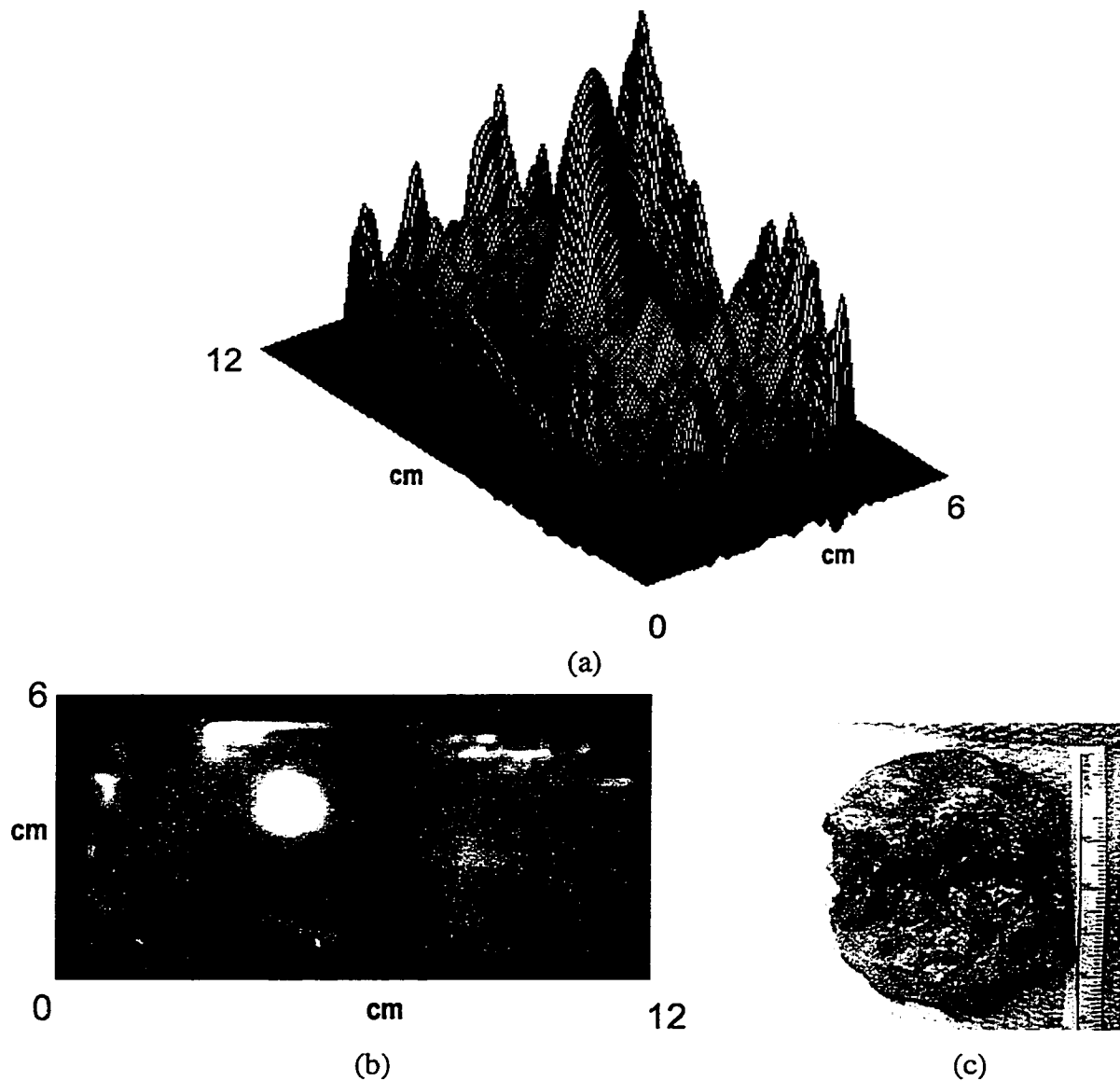
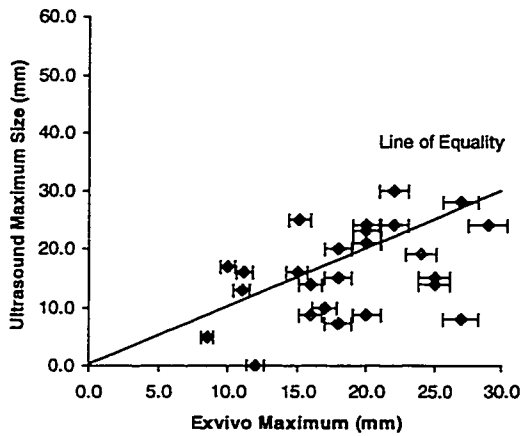
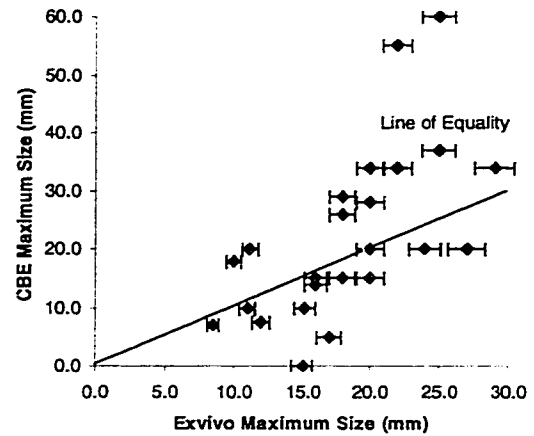


Figure 5.5: (a) A three dimensional topographic view of a tactile map of an infiltrating ductal carcinoma (red peak in center of map). (b) False color contour plot. The red spot in the center is the area of highest pressure, directly over the mass, while those along the right edge are due to the patient's rib. (c) Photograph of the same mass after surgical excision and bisection parallel to the imaging plane (the black ellipses are the approximate edge of the bisected halves of the tumor). The yellow tissue is normal breast fat. In the tactile map the mass size is estimated at 16 mm by 14 mm while its ex vivo palpable size is 16 mm by 12 mm.

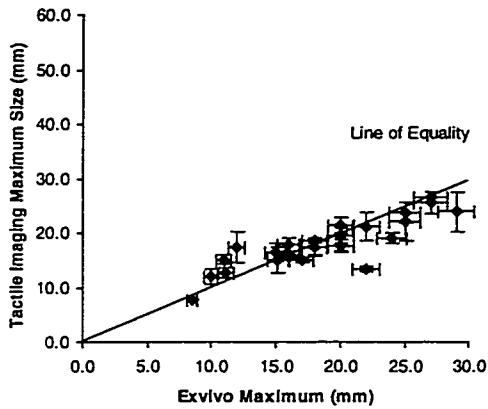


(a)

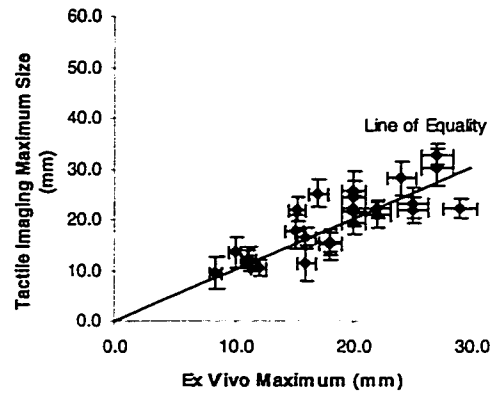


(b)

Figure 5.6: (a) Maximum size estimated from ultrasound compared to ex vivo maximum size. The slope of the best-fit line through zero is 0.90 ($r^2 = 0.14$) with mean absolute error, MAE, of 34%. (b) Maximum size estimated during clinical breast examination (CBE) compared with ex vivo measurements. The best-fit line through zero has slope 1.26 ($r^2 = 0.49$) with MAE= 47%. The abscissa error bars are $\pm 5\%$ standard deviation of the ex vivo size measurements (multiple measurements made by multiple examiners. Only one ultrasound or CBE examination was performed and therefore no error bars are shown in the ordinate. One mass has zero diameter in the CBE measurements because it was not palpable and one has zero diameter in the ultrasound measurements because it was not visible in the images.

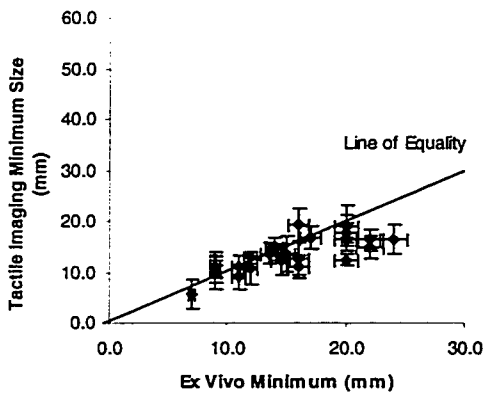


(a)

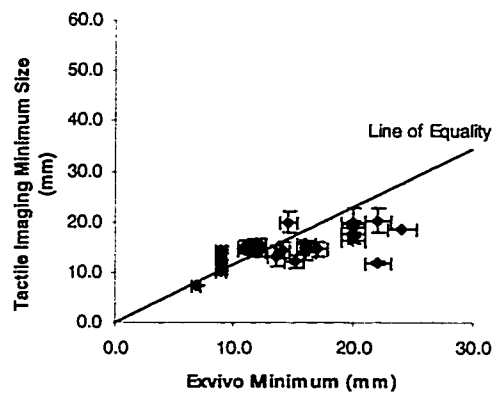


(b)

Figure 5.7: (a) Tactile imaging maximum diameter estimated using the thresholding algorithm compared to ex vivo maximum diameter. The best-fit line with zero intercept has slope 0.96 ($r^2=0.61$) with MAE = 12%. (b) Tactile imaging maximum diameter estimated from the Gaussian fit algorithm to ex vivo maximum diameter. The slope of the best-fit line is 1.04 ($r^2=0.60$) with MAE=17%. The error bars along the abscissa reflect the $\pm 5\%$ standard deviation of the ex vivo size measurements while those in the ordinate are ± 1 standard deviation of the three to five tactile images made of each lump.



(a)



(b)

Figure 5.8: (a) Tactile imaging minimum diameter estimated using the thresholding algorithm versus ex vivo minimum diameter. The slope of the best-fit line with zero intercept is 0.95 ($r^2=0.46$) with MAE = 19%. (b) Tactile imaging minimum diameter estimated using the Gaussian fit algorithm to ex vivo minimum diameter. The slope of the line with zero intercept is 0.87 ($r^2=0.40$) with MAE = 17%. The error bars in the abscissa reflect the $\pm 5\%$ standard deviation of the ex vivo size measurements while those in the ordinate are ± 1 standard deviation of the three to five tactile images made of each lump.

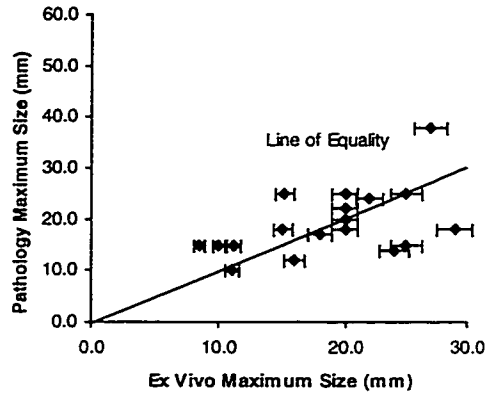


Figure 5.9: Maximum size measured by the pathologist compared to ex vivo maximum size. The slope of the best-fit line through zero is 1.04 ($r^2 = 0.49$) with mean absolute error, MAE, of 28%. The abscissa error bars are +/- 5% deviation of the ex vivo size measurements (multiple measurements made by multiple examiners). Only one pathology measurement was performed and therefore no error bars are shown in the ordinate. Only cancers are shown in this figure because no size was typically reported for benign lumps.

Chapter 6

Conclusions

6.1 Discussion

This thesis is an existence proof for tactile imaging. We have successfully developed a system that is more accurate and repeatable than the currently available breast imaging technologies, at least in a population of surgical patients. A significant limitation of this study is that it did not include a time series comparison of maps made at multiple times on a single patient, which makes it difficult to generalize repeatability and accuracy to the true patient population. However the system performed well in the larger patient population of women with benign breast lumps because we have shown in pilot studies that it can be used to image a wide variety of breast structures, ranging from scars to cysts to normal ridges of glandular tissue. In order to develop this system we have also created models of the interaction of tissue, tumor and indenter that were used to develop feature extraction algorithms. We have also shown that through frequent interaction with

physicians early in the development process it is possible to create a system that is not only effective but easy to use and interpret.

The tactile mapping algorithm that we developed to suppress noise and make the images easier to interpret performed admirably. It increased the signal to noise ratio from 5:1 in an individual tactile image to 50:1 in a typical tactile map. We have also succeeded, at least anecdotally, in making the maps easy to interpret. The two physicians who used the system most often remarked how similar the tactile images appeared to their mental image of the palpable breast lump being examined. In the breast clinic patients would often remark how easy the maps are to interpret and that they appeared as the lump felt to them. The most interesting thing about this pair of observations is that even though the patient was typically unable to explain how the lump felt to the doctor, they both could agree that it looked on the screen as they imagined it to look. Whether or not this is merely a case of the eye being more trusted than the hand would need to be proven, but it does bring up the interesting possibility of using tactile imaging as a way to improve communication between doctor and patient, as well as doctor to doctor.

During the course of this research we also made measurements of normal and abnormal breast tissue properties that we used for two purposes. The first was to develop empirical models of the interaction of the indenter and the breast tissue. The second was to see if there was any positive predictive value to tissue stiffness, a supposition that has been presented to us by many breast specialists. From this work we conclude that infiltrating ductal cancer and ductal carcinoma in situ, the two most common forms of breast cancer, are more than ten times as stiff as the surrounding breast fat and that there is a significant difference in stiffness between normal and abnormal tissue. We also

made another important observation: cancers show a much more nonlinear relationship between stress and strain than other normal breast tissues as evidenced by the larger exponent in the exponential fit to their stress-strain properties. These confirm anecdotal observations that were made by at least one breast specialist; that not only are cancers much harder than the surrounding fat and tissue, they also grow stiffer with applied load much more quickly (Krag 1998). This does not imply that all structures within the breast that are very hard are necessarily cancer: the fibroadenomas we measured were very stiff, but are benign abnormal tissue. We also arrived at a somewhat surprising result: breast tissue does not show a large viscous response, its behavior is largely independent of strain rate, at least for the rates at which we tested. These results all agree well with the work of Krouskop et al. (1998).

In order to use the tactile maps to estimate lump size, we developed two models of the indenter and tissue interaction. These finite element and empirical models were used to explore the invertibility of the maps and to develop algorithms that allowed for the estimation of lump size. These models agreed very well with each other and with tests made on simulated breast models made from hard plastic spheres embedded in soft silicone rubber. Two inversion algorithms were developed from these models: a model-based Gaussian fit method and a simple thresholding algorithm. These two inversion algorithms showed similar average performance in the rubber model and clinical tests. However, the simple thresholding scheme showed better repeatability (nearly twice as good) than the model fit scheme and points out one of the areas that the tactile imaging system can still be improved.

Although the tactile mapping algorithm does good job of suppressing the pseudo-random noise that appears at the image level, it does not adequately remove systematic errors in the maps that may be due to such sources as tissue non-linearity and improper normalization. These systematic errors are the likely cause of the relatively poorer performance of the model-based Gaussian feature extraction algorithm. Given the additional computational complexity of the algorithm and its relatively poorer performance, at this point in development it is better to use the thresholding algorithm to extract lump size. The Gaussian algorithm does illustrate the utility of the model for determining inversion algorithms for extracting features. These more sophisticated algorithms will become necessary when other features of the lump are desired such as lump stiffness or depth.

In this research we have also examined the accuracy of the other clinical examination techniques, which will enable future studies to be conducted with an estimate of the accuracy of these techniques. We have found that clinical breast examination is more accurate at estimating size than ultrasound or mammography and is accurate as pathology measurements of lump size when all techniques were compared to ex vivo measurements of palpable lump size. One could equivalently use pathology or clinical examination measurements for future trials. However, CBE is completely noninvasive (and pathology measurements certainly are not) it is the standard to use for subsequent experiments to further validate this or other imaging systems in the breast.

6.2 Future Development

Even though the tactile imaging system is relatively more accurate than the other methods of examining breast lumps, there are still many improvements that could be

made in the future. Perhaps the first improvement that should be made is to increase the repeatability of the pressure peaks in the map. Improving the physical hardware is the first thing that needs to be done to meet this goal. The most obvious change is to use a better distributed pressure transducer, but there are other alternatives available. One could include a single axis force sensor to measure the total applied load with more precision than is available currently. This would directly reduce normalization errors that account for the variation in the maps. It is relatively easy to increase the signal to noise ratio to 100:1 on a frame average basis using a single axis force sensor. This would provide a reduction in peak pressure variation in the maps of almost an order of magnitude and would not significantly increase the cost of the device.

Once the peak pressure variation in the maps is reduced, it is possible to develop a wide range of model-based feature extraction algorithms. One could hope to extract the stiffness of the lump by making multiple maps at different average input pressure levels. Because the tissue behavior is non-linear, one would see a non-linear increase in the pressure directly over the top of the lump. Measuring the ratio of peak pressure at different applied force levels is one way to estimate the change in stiffness of a particular lump and thereby extract additional diagnostic information. To validate this supposition and to develop algorithms to perform the extraction, it will be necessary to develop more sophisticated physical and mathematical models.

There are many avenues that can be pursued to improve the forward models. One that is likely to bear fruit is to extend the models so that they can be used to predict the maps at multiple average input force levels. Then, the nonlinear tissue properties measured in Chapter 3 could be included. As we have done in this thesis, looking for

general trends in the output of the forward models is likely to reveal simple ways of performing the signal processing that can extract these features from the maps. For example, one might look at the change in the amplitude of the Gaussian fit at different force levels as a measure of tissue non-linearity. This is analogous to looking at the change in the peak pressure ratio in the maps. The difficulty here is that we have shown that it is not possible to uniquely determine the depth, size and stiffness of a lump. If we could measure the depth using another means, it would greatly reduce the difficulty of the problem. Combining tactile imaging with ultrasound, perhaps in the same head, could be a solution, since ultrasound could be used to obtain depth information.

The models could also be extended to include the three dimensional geometry of the breast and the lumps that are being imaged. We have seen that there is a small, but significant, error in the size measurements that is a result of our two dimensional plane strain approximation. This could certainly be eliminated using algorithms developed from a fully three-dimensional model of head shape. Since we also know that most real breast lumps are not spherical, we can use three dimensional models to explore the effect that large and small aspect ratio of the lump has on the map and the individual images.

The clinical study presented in this work is a good proof-of-concept for tactile imaging, but it needs to be modified and expanded. In order to prove that tactile imaging can be used for lump size comparison across examinations performed by different examiners as well as serially across many examinations conducted at different times by a single examiner, another larger study will need to be performed. Serial repeatability can be assessed by having one clinician perform multiple maps at six month intervals on a group of patients with benign breast lumps. Having two different examiners perform

examinations on the same day can also be used to assess variation between examiners. Based on the results of our study, CBE is the best correlated to the ex vivo size measurements and should be used for future assessments of accuracy if ex vivo size measurements are not available.

6.3 Future Applications

A further use of the tactile imaging system in its current form was suggested by one of the breast specialists. He suggested that it could be used as a teaching tool to help women learn to perform breast self-examinations more effectively, because it would visually reinforce their mental image of what they are feeling (Dalton 1998). Other possibilities include use as a mass screening tool, if as suggested by the single lump found in the clinical study that was not palpable, it is more sensitive than well trained examiners. A clinician could use the tool to look for lumps in high risk patient populations who are not well served by currently available breast imaging techniques; for example younger women with a family history of breast cancer, or women who test positive for any of the newly discovered cancer oncogenes.

Both clinicians who participated in the clinical study indicated a desire to map the whole breast instead of just a single area (Dalton, Kern 1998). There are two basic problems that prevent the system from being used in this role. First the breast is too mobile to be imaged completely using a hand held head. Second, the plane approximation used in the mapping algorithm breaks down in such a large area. To alleviate both of these difficulties, it might be possible to stretch a membrane over the breast (using the nipple for alignment) and thereby immobilize it. The tactile imaging system could then be used to make four maps, one of each quadrant and these could be

used for tracking. Flattening the breast could potentially provide increased sensitivity as well because we know the cancers will get much stiffer than the surrounding tissue with increased strain and therefore be more visible in the tactile images and maps.

Another possibility is in the emerging field of telemedicine. Many primary care physicians do not routinely palpate cancerous breast lumps and therefore are unsure of what they feel like. This often leads to referrals to a breast specialist because the physician is unsure that the lump is benign that could be eliminated. One can imagine the situation where a primary care physician would have the device in his office, and would use it to make a tactile map of the indeterminate breast mass. This tactile map could then be sent to the specialist for reading, rather than sending the patient. This would lead to improvements in care through reduction in lead-time of diagnosis, and reductions in cost which is an ever more important challenge to the medical system.

Finally we note that although we have tailored our application to producing a tactile imaging system that is for use in the breast, the basic technology is not limited to documenting the features of breast lumps. There are many other possible applications. These include finding the liver and spleen during physical examination, or localizing lumps during lung surgery. One could even use a suitably modified system to find lumps in the prostate to screen for prostate cancer. However, because palpation is ubiquitous, the possibilities are nearly innumerable. It is even possible that one day a tactile imager could be as widely used as a blood pressure cuff.

Bibliography

American Cancer Society. Cancer Facts and Figures, <http://nysernet.org/bcic/acs2/communications/facts94.htm>. 1994.

Atkinson, KE. *An Introduction to Numerical Analysis*. John Wiley and Sons, 1989.

Bloom, H.S. et als. Major stimulus dimensions determining detection of simulated breast lesions. *Perception and Psychophysics*. 32:251-60. 1982.

Breast Cancer Facts and Figures, 1997. American Cancer Society, 1997.

Cespedes I, Ophir J, Ponnekanti H and Maklad N. Elastography: elasticity imaging using ultrasound with application to muscle and breast in vivo. *Ultrasonic Imaging*. 15(2):73-88, 1993 Apr.

Chenevert TL, Skovoroda AR, O'Donnell M and Emelianov SY. Elasticity Reconstructive Imaging via Simulated Echo MRI. *Magnetic Resonance Imaging*. 1997.

Dalton E. Personal communication, 1998.

Dario P, Bergamasco M and Sabatini A. Sensing body structures by an advanced robot system. *Proceedings of the 1988 IEEE International Conference on Robotics and Automation*. vol.3, p.1758-63 1988.

Dixon JM and Mansel RE. ABC of Breast Disease. Symptoms Assessment and Guideline for Referral. *BMJ*. 309:722-726, 1994 Sep. 17.

Eberly. D. Least Squares Fitting of Data. *Technical Report*. University of North Carolina - Chapel Hill, 1997.

Eshelby, J.D. The determination of the elastic field of an ellipsoidal inclusion and related problems. *Proc. R. Soc. Lond.*, A 241:376-396. 1957.

- Fearing, R. S. and Hollerbach, J. M. Basic solid mechanics for tactile sensing. *International Journal of Robotics Research*, 4(3):40-54, Fall 1985.
- Fowlkes JB, Emelianov SY, Pipe JG, Skovoroda AR, Carson PL, Adler RS, Sarvazyan AP. Magnetic-resonance imaging techniques for detection of elasticity variation. *Medical Physics*, vol.22, no.11, pt.1, p. 1771-8. Nov. 1995.
- Frei EH, Sollish BD, Yerushalmi S, Instrument for viscoelastic measurement. U.S. Patent # 4,250,894, (1981)
- Fung YC. *Biomechanics: Mechanical Properties of Living Tissues 2nd Edition*. Springer Verlag, NY. 1993.
- Garra BS, Cespedes EI, Ophir J, Spratt SR, Zuurbier RA, Magnant CM and Fennanen MF. Elastography of Breast Lesions: Initial Clinical Results. *Radiology* 1997; 202:79-86.
- Gentle, C.R. Mammobarography: a possible method of mass breast screening. *J. Biomed. Eng.*, Vol. 10. April 1988.
- Goodier, J.N. Concentration of stress around spherical and cylindrical inclusions and flaws. *Phil. Mag.*, 7(22):678. 1936.
- Hildebrand, F.B. *Advanced Calculus for Applications (2nd Edition)*. Prentice-Hall, Inc. Englewood Cliffs, New Jersey. 1976.
- Haagensen CD. *Diseases of the Breast, 3rd Edition*. p521-527 Philadelphia, Saunders 1986.
- Harris JR, Lippman ME, Morrow M and Hellman S. *Diseases of the Breast*. Lippincott-Raven. 1996.
- Hayes, WC, Keer, LM, Herrmann G and Mockros LF. A Mathematical Analysis for Indentation Tests of Articular Cartilage. *J. Biomechanics*, Vol. 5, pp541-551, 1972. Pergamon Press.
- Howe RD, Peine WJ, Kontarinis DA and Son JS. Remote Palpation Technology for Surgical Applications. *IEEE Engineering in Medicine and Biology* 14(3):318-323, 1995.
- Johnson, K.L. *Contact Mechanics*. Cambridge University Press. 1985.
- Kern K. Personal communication, 1998.
- Koganezawa K, Takanishi A, Sugano S eds. *Development of Waseda Robot: The Study of Biomechanisms and Kato Laboratory (3rd Edition)*. Waseda University. 1991.

- Konofagou E, Dutta P, Ophir J, Cespedes I. Reduction of stress nonuniformities by apodization of compressor displacement in elastography. *Ultrasound in Medicine & Biology*. 22(9):1229-36, 1996.
- Krag D. Personal communication, 1998.
- Krouskop TA, Wheeler TM, Kallel F, Garra BS and Hall T. The Elastic Moduli of Breast and Prostate Tissues Under Compression, *Ultrasonic Imaging*. 20:151-159, 1998.
- Lavin PT, Flowerdew G. Studies in variation associated with the measurement of solid tumors. *Cancer*. 46(5):1286-90, 1980 Sep 1.
- Lerner RM, Parker KJ, Holen J, Gramiak R and Wang RC. Sono-elasticity: Medical Elasticity Images Derived from Ultrasound. *Acoustical Imaging*. Vol. 16. June 10-12. 1987.
- Mack MJ, Shennib H, Landreneau RJ, and Hazelrigg SR, 1993. "Techniques for Localizing of Pulmonary Nodules for Thoracoscopic Resection," *J. Thoracic Cardiovascular Surgery*. 106(3): 550-553.
- Manduca A, Muthupillai R, Rossman PJ, Greenleaf JF, Ehman RL. Visualization of tissue elasticity by magnetic resonance elastography. *Proceedings of Fourth International Conference on Visualization in Biomedical Computing (VBC'96)*. p.xii+610, 63-8 22-25 Sept. 1996
- Muthupillai R, Lomas DJ, Rossman PJ, Greenleaf JF, Manduca A and Ehman RL. Magnetic Resonance Elastography by Direct Visualization of Propagating Acoustic Strain Waves. *Science*, vol. 269 p1854-1857. 29 September 1995.
- Parker SL, Tong T, Bolden S, Wingo PW. Cancer Statistics, 1997. *CA - A Cancer Journal for Clinicians*. 1997;47:5-27.
- Pawluk, DTV. A Holistic Model Of The Human Sense of Touch and a Dynamic Contact Model of the Human Fingerpad. *Ph.D. Thesis*. Harvard University, June 1997.
- Peine WJ. Remote Palpation Instruments for Minimally Invasive Surgery. *Ph.D. Thesis*. Harvard University, October 1998.
- Potchen, E. James and Sierra, Arlene E. The Detection and Cure of Breast Cancer. *Breast Disease*. Obstetrics and Gynecology Clinics of North America. 14-3: 667-684. September 1987.
- Ries LAG, Kosary CL, Hankey BF, Miller BA, Edwards BK (eds). *SEER Cancer Statistics Review, 1973-1995*, National Cancer Institute, Bethesda MD. 1998.
- Sarvazyan, AP, Skovoroda, AR, Emelianov, SY, Fowlkes JB, Pipe, JG, Adler, RS Buxton, RB and Carson, PL. Biophysical Bases of Elasticity Imaging. *Acoustical Imaging*, Vol. 21. Ed. JP Jones. Plenum Press, New York, 1995.

Sarvazyan AP. Knowledge-Based Mechanical Imaging. *Proceedings of the 10th IEEE Symposium on Computer-Based Medical Systems*. p120-125, 1997.

Sarvazyan AP, Skovoroda AR and Pyt'ev YP. Mechanical Introscopy – A New Modality of Medical Imaging for Detection of Breast and Prostate Cancer. *Eighth IEEE Symposium on Computer Based Medical Systems*. June , 1997.

Skovoroda AR, Klishko AN, Gusakyan DA, Mayevskii YI, Yermilova VD, Oranskaya GA and Sarvazyan AP. Quantitative Analysis of the Mechanical Characteristics of Pathologically Changed Soft Biological Tissues. *Biophysics* 40:6. 1359-1364, 1995. Elsevier Science Ltd.

Son, Jae , Cutkosky, Mark and Howe, Robert. Comparison of Contact Sensor Localization Abilities During Manipulation. *Journal of Robotics and Autonomous Systems*. 17(4). June/July 1996.

Wellman PS, Howe RD, Cundari MA, Dewagan N, Dalton E and Kern KA. Tactile Imaging. *Submitted to Science*. 1999.

Yu, H. Y. and Sanday, S.C. Elastic field in joined semi-infinite solids with an inclusion. *Proc. R. Soc. Lond. A* 434:521-530. 1991.

Zhang, M, Zheng, YP and Mak AFT. Estimating the effective Young's modulus of soft tissues from indentation tests – nonlinear finite element analysis of effects of friction and large deformation. *Med. Eng. Phys.* Vol. 19, No. 6 pp512-517, 1997

Appendix A

Distributed Pressure Sensor Characterization

A.1 Sensor Description

The distributed pressure sensor that we use is a TekScan Model 5208 (TekScan, Inc. South Boston, MA) piezo-resistive sensor. It was chosen primarily because it is expensive, flexible and durable. The sensor is created by printing lines made with a partially conductive ink onto a Kapton (polyimide) backer. These two layers are then brought into contact as shown in Figure A-1. Although the resistance of the ink changes with large applied pressures, in the pressure range we are interested in, it is more likely that the gain change is because of a change in the contact area of the rows and columns, as shown in Figure A-2.

A.2 Characterization Methods

An air pressure chamber that could apply loads to the surface of the sensor was constructed and the pressure inside the chamber was monitored with a Motorola MPX-5050 pressure transducer. The volume of air in the chamber was kept to the minimum possible in order to be able to produce fast ramps on the face of the sensor. Pressure steps could be applied in 11 millisecond (0%-95% rise time), and the pressure could be vented from the chamber in 8 milliseconds (100%-5% fall time). To characterize the rise and fall time we applied a pressure step from 0 kPa to 18kPa, and then waited for the sensor to reach equilibrium. After equilibrium was reached, the load was dropped again to 0 kPa. Sensor gain and offset were examined by performing multiple load unload trials at these two pressure levels and taking multiple sensor readings at the equilibrium values. The spatial response of the sensor was estimated using a 0.5mm diameter probe to apply a 18kPa load to each element. The value of that element and each of its neighbors over many trials was recorded to estimate spatial coupling.

A.3 Results

Typical sensor response time was measured to be 50 milliseconds (0%-95% of value) while sensor fall time (100%-5% of value) was less than 50 milliseconds. Spatial coupling between elements was lower than the noise floor of 2.5% set by averaging 150 sensor frames and can be assumed to be zero.

The most interesting result of the testing is that each sensor element can be assumed to have a Gaussian distribution, with mean equal to the applied load, across loading-unloading cycles provided the applied pressure goes to zero between cycles. This motivates the important observation that the sensor head must not remain in contact

with the tissue to be imaged for the entire examination, but instead should be brought into and out of contact in multiple passes. Figure A.5 illustrates that the distribution is approximately Gaussian in appearance.

After a linear calibration was applied, average accuracy was found to be 10% on a single element basis, while the mean was accurate to 5%. Across multiple trials one standard deviation of both of these numbers is 5% and 1.5% respectively, indicating that 95% of the elements will be $\pm 20\%$ of the mean on any given frame, and that the mean is typically trustworthy to $\pm 8\%$.

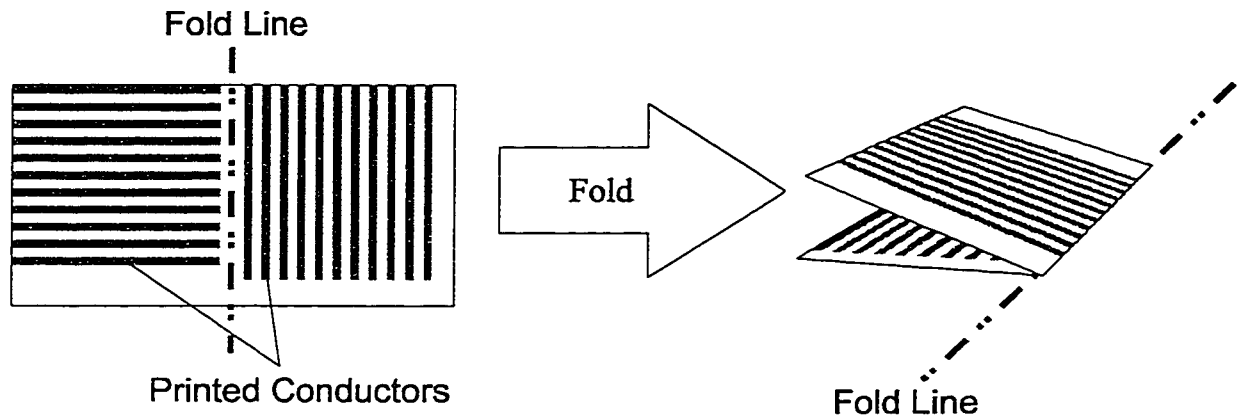


Figure A.1: The elements of the sensor are made by printing conductive ink in rows and columns on two layers of Kapton and then folding the sensor to bring them into contact with each other.

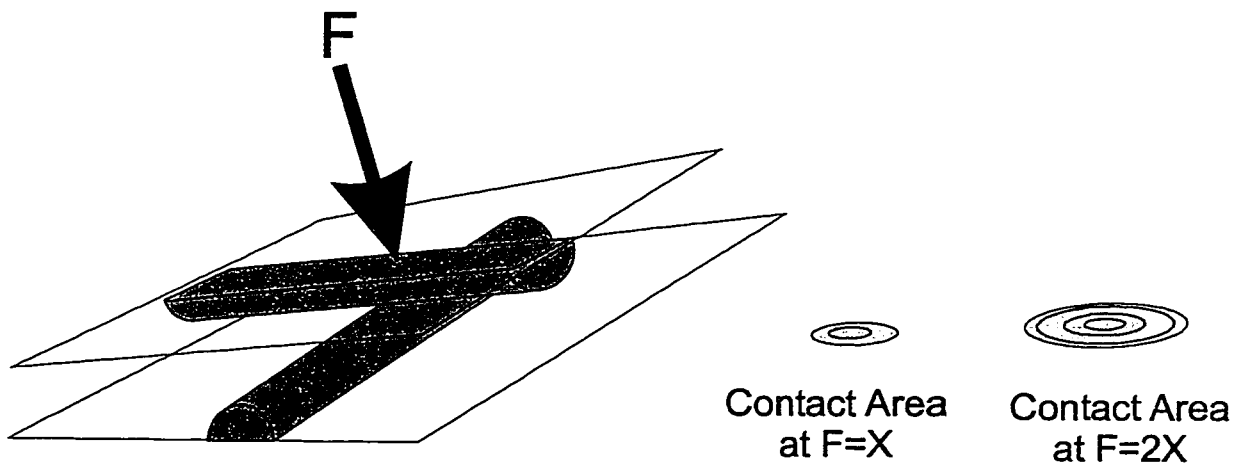


Figure A.2: The transduction mechanism is likely the change in contact area between the crossed conductors in the sensor that results from changes in applied load. When the contact area changes, the electrical resistance of the intersection point decreases.

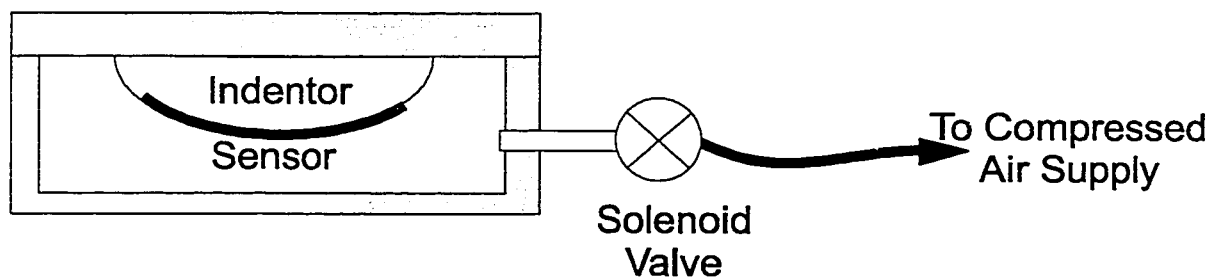


Figure A.3: The air pressure chamber used to characterize the sensor.

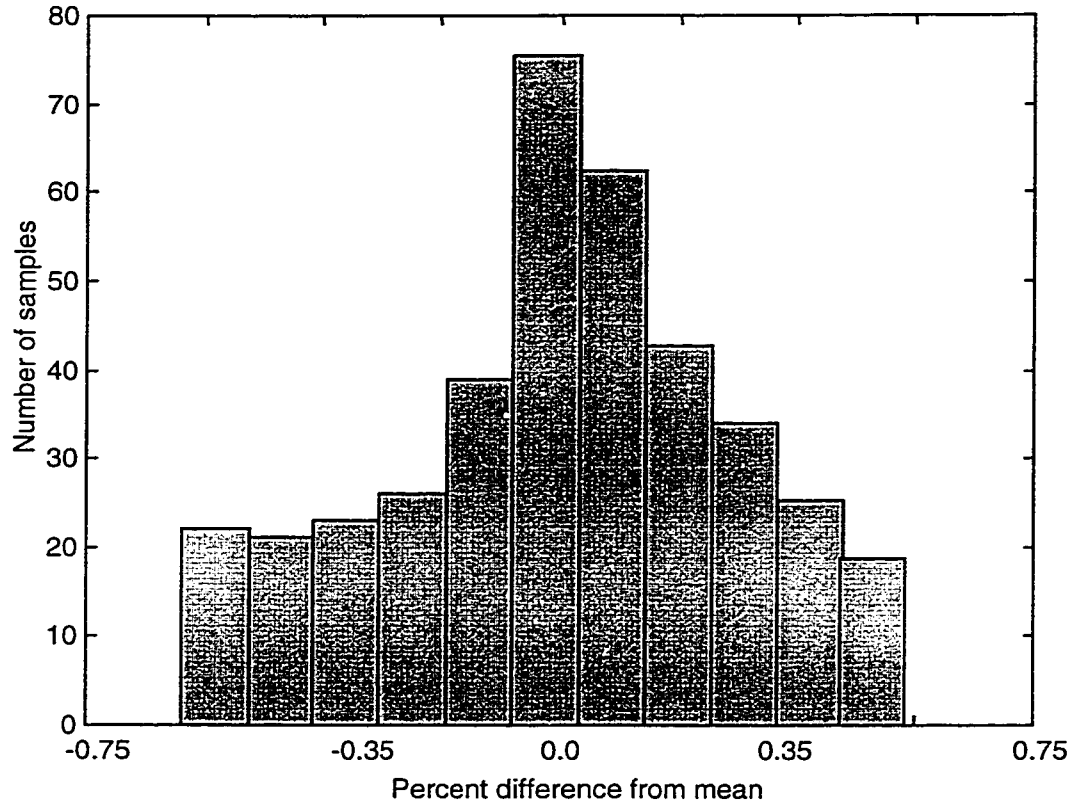


Figure A.4: The pressures measured by a particular element are Gaussian provided there are multiple loading-unloading cycles through zero. Figure is presented for a typical sensor element across 15 loading unloading cycles.

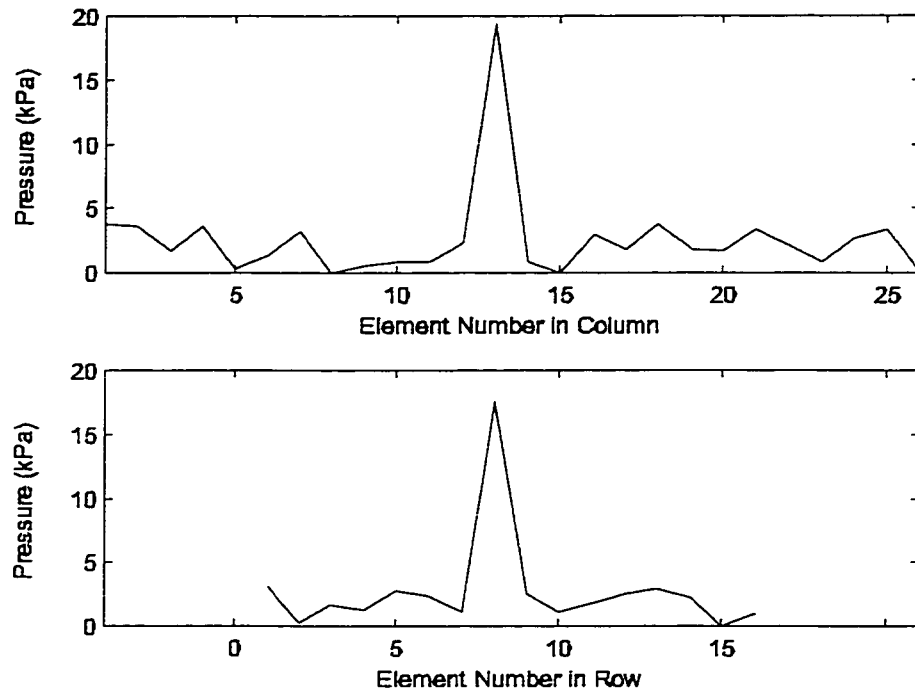


Figure A.5: Typical spatial response for a load applied to one element using a 0.5mm diameter flat-bottomed punch. The figure is averaged across twenty indentations. For this figure, the load was applied to the element in row 8, column 13. Any spatial coupling that is present is below the noise floor of the measurements.

Appendix B

Tactile Mapping Coordinate Frame Transformations.

B.1 Selection of the Best Fit Plane and Reference Line

Figure 2.4 shows a schematic of the different coordinate frames assigned to the patient during imaging. These frames, as well as the user selected reference line are shown in more detail in Figure B.1. The reference line, selected as described in the section on clinical technique, is used to define a reference axis that is shown in Figure B.1 as \mathbf{u}_y . We use this axis to define the direction of the y axis of the patient and require that this image must be parallel to the best fit image plane. This is done to ensure that the individual pressure frames are projected properly and the map produces a representative image. Mathematically, we require that the z axis of the C frame be in the same direction as the normal to the best fit plane.

Thus, we must first determine the best fit plane before proceeding. The user is told to start an examination once the reference line has been determined by pressing the sensor, aligned in a direction substantially the same as it will be used during the

examination, into the tissue directly above the lump to be imaged. The first ten valid frames are used to determine the plane that is the best least square fit to the data. Ten frames are chosen to give sufficient data to give an accurate fit, but acquired quickly enough that the user does not move greatly away from the center of the lump to be imaged during the examination. Since the point locations determined by the magnetic tracker could be co-linear, we actually use the four corners of the sensor. These four corners are uniquely located in the S reference frame and can be transformed to the T frame (the tracker basis frame)

$${}^O\rho(i, j) = T_O^B T_B^S [{}^S\rho(i, j)] \quad (\text{B-1})$$

where ${}^S\rho(i, j)$ is the location of the (i,j)th element of the sensor with respect to the S frame, T_B^S is the homogeneous (4x4) transformation matrix between the S (sensor frame) and B (magnetic tracker in the handle) frames, and T_O^B is the transform from the B frame to the O (reference) frame. Once the locations for the four corners are determined for each of the n frames they are vectorized

$$\mathbf{V}_x = [{}^O\rho_x(i, j)_1, \dots, {}^O\rho_x(i, j)_n] \quad (\text{B-2})$$

$$\mathbf{V}_y = [{}^O\rho_y(i, j)_1, \dots, {}^O\rho_y(i, j)_n] \quad (\text{B-3})$$

$$\mathbf{V}_z = [{}^O\rho_z(i, j)_1, \dots, {}^O\rho_z(i, j)_n] \quad (\text{B-4})$$

and a best fit plane can be found using orthogonal regression (Eberly 1998). This can be accomplished by forming the matrix (provided the data is centered on zero, which can be accomplished with a simple subtraction)

$$\mathbf{M} = \begin{bmatrix} \mathbf{V}_x \mathbf{V}_x^T & \mathbf{V}_x \mathbf{V}_y^T & \mathbf{V}_x \mathbf{V}_z^T \\ \mathbf{V}_y \mathbf{V}_x^T & \mathbf{V}_y \mathbf{V}_y^T & \mathbf{V}_y \mathbf{V}_z^T \\ \mathbf{V}_z \mathbf{V}_x^T & \mathbf{V}_z \mathbf{V}_y^T & \mathbf{V}_z \mathbf{V}_z^T \end{bmatrix}. \quad (\text{B-5})$$

Finding the eigenvalues of this matrix yield the principal directions of the data. Since our data is approximately planar (has much larger extent in the x and y than in the z), the smallest eigenvalue corresponds to the z direction and its corresponding eigenvector, \mathbf{X}_z is the normal to the plane. Now we want the y-axis of the plane to be aligned with the y-axis of the sensor during the motion, \mathbf{v}_y . We define the basis vectors for the plane

$$\mathbf{e}_z^P = \frac{\mathbf{X}_z}{|\mathbf{X}_z|} \quad (\text{B-6})$$

$$\mathbf{e}_x^P = \frac{\mathbf{v}_y \times \mathbf{e}_z}{|\mathbf{v}_y \times \mathbf{e}_z|} \quad (\text{B-7})$$

and

$$\mathbf{e}_y^P = \frac{\mathbf{e}_x \times \mathbf{e}_z}{|\mathbf{e}_x \times \mathbf{e}_z|}. \quad (\text{B-8})$$

The homogeneous transform from the best fit plane to the O frame is,

$$T_O^P = \begin{bmatrix} \mathbf{e}_x^P & \mathbf{e}_y^P & \mathbf{e}_z^P & 0 \\ 0 & 0 & 0 & 1 \end{bmatrix}. \quad (\text{B-9})$$

To find the transform T_O^C from the user selected reference frame to the base frame, we define \mathbf{u}_y shown in Figure B.1 as the direction of the y-axis of the patient's chest. With \mathbf{e}_z^P as defined in equation B-6, we select the other basis vectors as

$$\mathbf{e}_z^C = \mathbf{e}_z^P \quad (\text{B.10})$$

$$\mathbf{e}_x^C = \frac{\mathbf{u}_y \times \mathbf{e}_z}{|\mathbf{u}_y \times \mathbf{e}_z|} \quad (\text{B.11})$$

$$\mathbf{e}_y^C = \frac{\mathbf{e}_x \times \mathbf{e}_z}{|\mathbf{e}_x \times \mathbf{e}_z|} \quad (\text{B.12})$$

The homogeneous transformation

$$T_O^C = \begin{bmatrix} \mathbf{e}_x^C & \mathbf{e}_y^C & \mathbf{e}_z^C & 0 \\ 0 & 0 & 0 & 1 \end{bmatrix} \quad (\text{B.13})$$

maps points in the chest frame to points in the base frame. The points on the sensor surface referenced to frame C are

$${}^C \rho(i, j) = T_C^P T_P^S [{}^S \rho(i, j)]. \quad (\text{B.14})$$

We need only find T_P^S and T_C^P in terms of previously calculated transformations. Looking at Figure B.1

$$T_O^C T_C^P T_P^S = T_O^B T_B^S. \quad (\text{B.15})$$

Solving (28) for $T_C^P T_P^S$ and substituting into (29)

$${}^C \rho(i, j) = (T_O^C)^{-1} T_O^B T_B^S [{}^S \rho(i, j)] \quad (\text{B.16})$$

which is an expression that gives the locations of the individual sensor elements in the examiner selected reference frame. This means that T_C^S of equation 2 is

$$T_C^S = (T_O^C)^{-1} T_O^B T_B^S \quad (\text{B.17})$$

which is the solution we require relating individual element locations within a particular frame to their appropriate locations in the best fit plane.

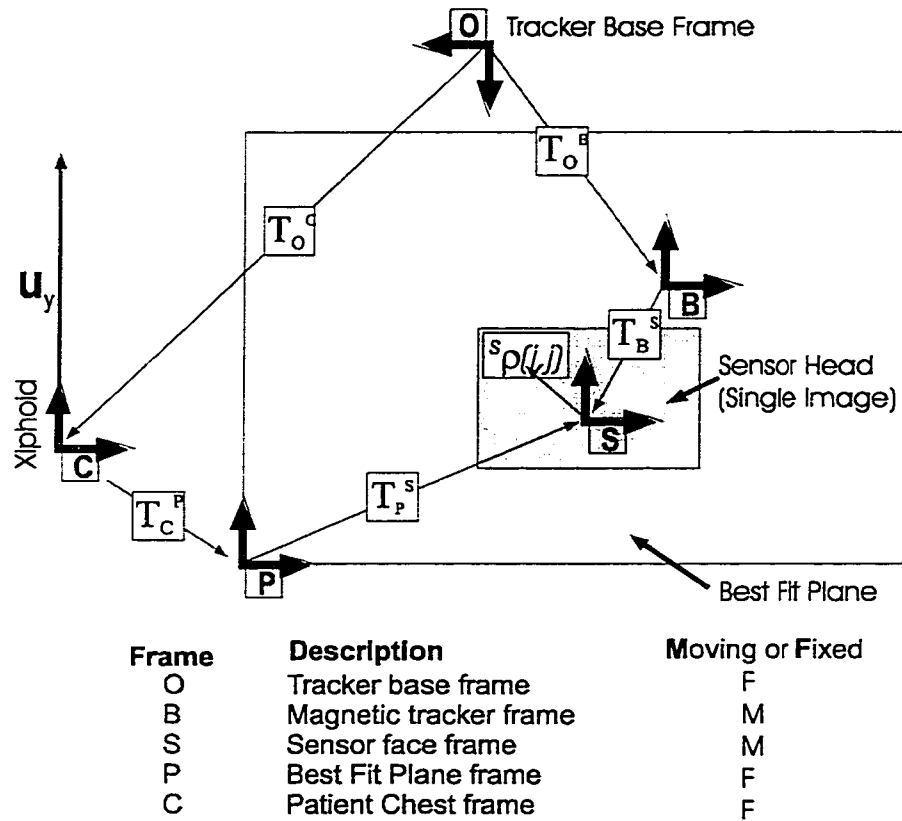


Figure B.1: A schematic of the coordinate transformations required to collocate the individual pressure images within a single tactile map.

Appendix C

Fit Constants for the Forward Model

This appendix contains the fit constants determined by fitting the empirical model

$$P_2(x, d, E_2 / E_1, h / d) = g(d, E_2 / E_1, h / d) \cdot e^{-\left(\frac{x^2}{2\sigma(d, E_2 / E_1, h / d)^2}\right)} \quad (\text{A-1})$$

(which is Equation 4-2) to the pressure distributions determined using the finite element models discussed in Chapter 4.

	<i>d</i> =0.5	<i>d</i> =1.0	<i>d</i> =1.5	<i>d</i> =2.0	<i>d</i> =2.5
<i>h</i> =0.6	0.8048	0.7372	0.6695	0.6018	0.5342
<i>h</i> =0.8	0.7009	0.6057	0.5449	0.5242	0.5101
<i>h</i> =1.0	0.6343	0.5545	0.5184	0.4987	0.4778
<i>h</i> =1.2	0.5908	0.5218	0.4914	0.4783	0.4666
<i>h</i> =1.5	0.5515	0.4927	0.4689	0.4547	0.4427
<i>h</i> =1.8	0.5241	0.4757	0.4642	0.4509	0.4423

Table C.1: Fit constant *a* for $E_2/E_1=2$.

	<i>d</i> =0.5	<i>d</i> =1.0	<i>d</i> =1.5	<i>d</i> =2.0	<i>d</i> =2.5
<i>h</i> =0.6	1.1221	0.9998	0.8738	0.7497	0.6256
<i>h</i> =0.8	0.8542	0.7822	0.7103	0.6133	0.5663
<i>h</i> =1.0	0.7232	0.6683	0.6135	0.5445	0.5037
<i>h</i> =1.2	0.6352	0.5752	0.5332	0.5002	0.4751
<i>h</i> =1.5	0.5872	0.5169	0.4855	0.4692	0.4488
<i>h</i> =1.8	0.5477	0.4956	0.4755	0.4613	0.4417

Table C.2: Fit constant *a* for $E_2/E_1=5$.

	$d=0.5$	$d=1.0$	$d=1.5$	$d=2.0$	$d=2.5$
$h=0.6$	1.3016	1.1412	0.9807	0.8202	0.6598
$h=0.8$	0.9273	0.8069	0.7163	0.6356	0.585
$h=1.0$	0.8145	0.6701	0.6171	0.5642	0.5112
$h=1.2$	0.7016	0.5901	0.5432	0.5164	0.4795
$h=1.5$	0.6012	0.5285	0.498	0.4721	0.4549
$h=1.8$	0.5566	0.4958	0.4806	0.4623	0.4431

Table C.3: Fit constant a for $E_2/E_1=8$.

	$d=0.5$	$d=1.0$	$d=1.5$	$d=2.0$	$d=2.5$
$h=0.6$	1.3871	1.257	1.1269	0.9969	0.8668
$h=0.8$	0.9585	0.8536	0.7165	0.6523	0.5916
$h=1.0$	0.7912	0.6826	0.6174	0.5772	0.5138
$h=1.2$	0.7024	0.5972	0.5434	0.5183	0.4809
$h=1.5$	0.6067	0.5321	0.4982	0.4791	0.4594
$h=1.8$	0.56	0.4978	0.4852	0.4657	0.4439

Table C.4: Fit constant a for $E_2/E_1=10$.

	$d=0.5$	$d=1.0$	$d=1.5$	$d=2.0$	$d=2.5$
$h=0.6$	2.0731	1.8133	1.5536	1.3263	1.034
$h=0.8$	1.1685	0.9977	0.825	0.7323	0.622
$h=1.0$	0.8842	0.7437	0.6296	0.5772	0.5278
$h=1.2$	0.7395	0.6305	0.5532	0.5183	0.4859
$h=1.5$	0.6319	0.548	0.4993	0.4801	0.4616
$h=1.8$	0.5756	0.5068	0.4888	0.4727	0.4519

Table C.5: Fit constant a for $E_2/E_1=100$.

	$d=0.5$	$d=1.0$	$d=1.5$	$d=2.0$	$d=2.5$
$h=0.6$	2.0731	1.8133	1.5536	1.3263	1.034
$h=0.8$	1.1685	0.9977	0.825	0.7323	0.622
$h=1.0$	0.8842	0.7437	0.6296	0.5772	0.5278
$h=1.2$	0.7395	0.6305	0.5532	0.5183	0.4859
$h=1.5$	0.6319	0.548	0.4993	0.4801	0.4616
$h=1.8$	0.5756	0.5068	0.4888	0.4727	0.4519

Table C.6: Fit constant σ for $E_2/E_1=2$.

	$d=0.5$	$d=1.0$	$d=1.5$	$d=2.0$	$d=2.5$
$h=0.6$	2.0731	1.8133	1.5536	1.3263	1.034
$h=0.8$	1.1685	0.9977	0.825	0.7323	0.622
$h=1.0$	0.8842	0.7437	0.6296	0.5772	0.5278
$h=1.2$	0.7395	0.6305	0.5532	0.5183	0.4859
$h=1.5$	0.6319	0.548	0.4993	0.4801	0.4616
$h=1.8$	0.5756	0.5068	0.4888	0.4727	0.4519

Table C.7: Fit constant σ for $E_2/E_1=5$.

	$d=0.5$	$d=1.0$	$d=1.5$	$d=2.0$	$d=2.5$
$h=0.6$	2.0731	1.8133	1.5536	1.3263	1.034
$h=0.8$	1.1685	0.9977	0.825	0.7323	0.622
$h=1.0$	0.8842	0.7437	0.6296	0.5772	0.5278
$h=1.2$	0.7395	0.6305	0.5532	0.5183	0.4859
$h=1.5$	0.6319	0.548	0.4993	0.4801	0.4616
$h=1.8$	0.5756	0.5068	0.4888	0.4727	0.4519

Table C.8: Fit constant σ for $E_2/E_1=8$.

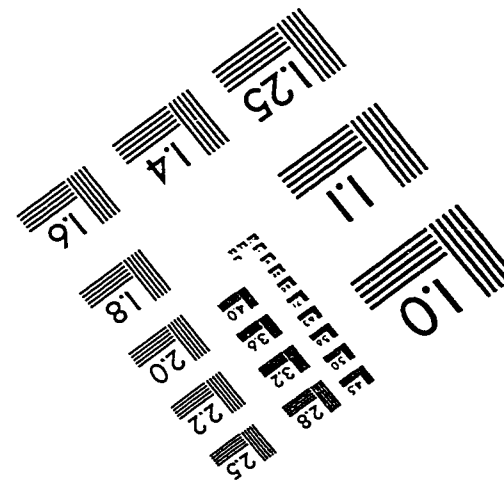
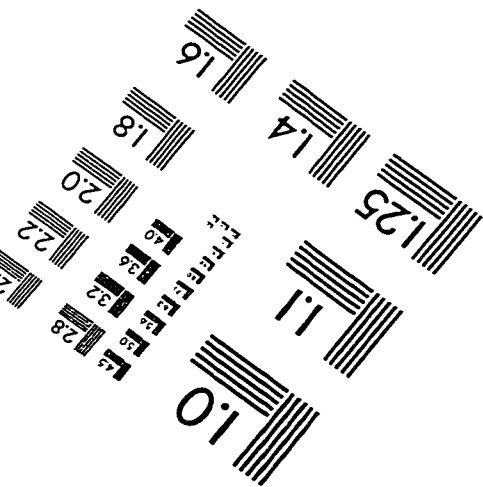
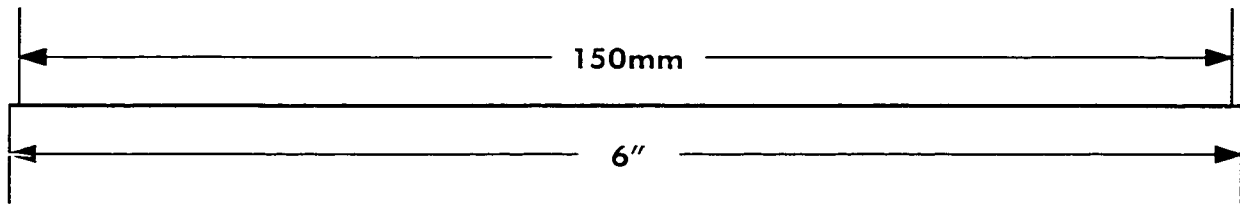
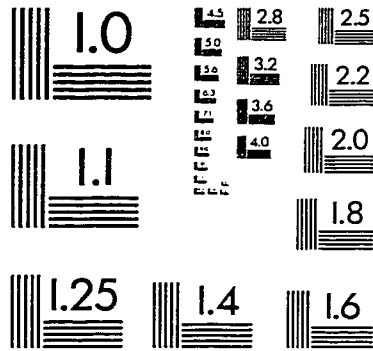
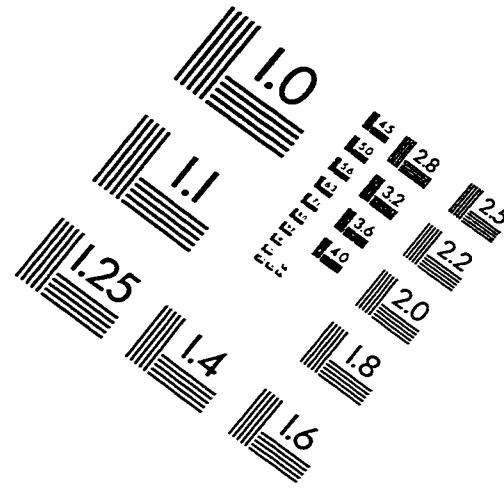
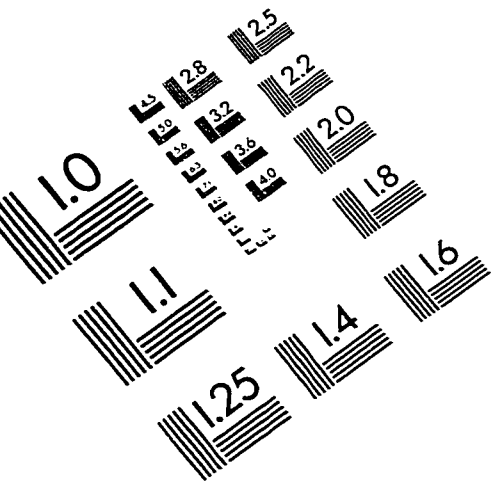
	$d=0.5$	$d=1.0$	$d=1.5$	$d=2.0$	$d=2.5$
$h=0.6$	0.2086	0.2484	0.2963	0.3415	0.4011
$h=0.8$	0.2522	0.3481	0.4558	0.5164	0.5815
$h=1.0$	0.3284	0.4638	0.5882	0.6863	0.8111
$h=1.2$	0.4751	0.5889	0.7622	0.9045	1.0838
$h=1.5$	0.582	0.7526	1.031	1.2806	1.6038
$h=1.8$	0.6866	0.9734	1.279	1.6698	2.2192

Table C.9: Fit constant σ for $E_2/E_1=10$.

	$d=0.5$	$d=1.0$	$d=1.5$	$d=2.0$	$d=2.5$
$h=0.6$	0.1774	0.1767	0.2859	0.3377	0.4005
$h=0.8$	0.2239	0.3284	0.4438	0.4949	0.5884
$h=1.0$	0.3295	0.4407	0.5774	0.6646	0.8044
$h=1.2$	0.4157	0.5533	0.7518	0.8874	1.0617
$h=1.5$	0.5424	0.7233	1.0462	1.2331	1.5871
$h=1.8$	0.6669	0.937	1.1511	1.5921	2.1725

Table C.10: Fit constant σ for $E_2/E_1=100$.

IMAGE EVALUATION TEST TARGET (QA-3)



APPLIED IMAGE, Inc
1653 East Main Street
Rochester, NY 14609 USA
Phone: 716/482-0300
Fax: 716/288-5989

© 1993, Applied Image, Inc., All Rights Reserved